Open a New Window of Plasma Diagnostics in the Solar Physics with Spectropolarimetric Observation

Thesis submitted in accordance with the requirements of
the Kyoto University for the degree of Doctor in Philosophy
by
Tetsu Anan

January 2014

Abstract

Magnetic fields govern the plasma dynamics in the outer layers of the solar atmosphere. The magnetic energy built up by convection in and below the photosphere is transferred from the photosphere into the heliosphere. During the transfer of energy into the outer layers of the solar atmosphere, i.e., chromosphere and corona, the magnetic energy is partially converted into plasma kinetic and thermal energy, causing various active phenomena and heating in the solar atmosphere. Electric field diffuses the magnetic energy through resistivity and accelerates charged particles. Furthermore, electric field acting on neutral atoms that move across the magnetic field enables us to study the dynamical coupling between neutrals and ions in the plasma.

To open a new window of plasma diagnostics by using polarization mechanisms of spectral line and measure the magnetic field, electric field, and anisotropies in atomic excitation in solar atmosphere, we developed a new universal spectropolarimeter on the Domeless Solar Telescope at Hida Observatory to realize precise spectropolarimetric observations in a wide range of wavelength in visible and near infrared. The polarimeter consists of a 60 cm aperture vacuum telescope, a high dispersion vacuum spectrograph, polarization modulator and analyser composed of a continuously rotating waveplate whose retardation is constant in 400 - 1100 nm and Wallaston prisms located closely behind the focus of the telescope, and a fast and high sensitive CCD camera or a infrared camera. The polarimeter achieves photometric accuracy of 10^{-3} in 30 - 60 s at spatial sampling of 0.4 arcsec. Instrumental polarization of the telescope is calibrated by using a remotely controllable turret accommodating linear polarizers attached at the entrance window of the telescope to induce well known polarized light into the telescope. Thus a Mueller matrix model of the telescope is established to compensate the instrumental polarization in observed data within the required accuracy.

In order to measure the magnetic and electric fields of chromospheric jets, the full Stokes spectra of the Paschen series of neutral hydrogen in a surge and in some active region jets that took place at the solar limb were observed on May 5, 2012, using the newly developed spectropolarimeter of the Domeless Solar Telescope. First, we inverted the Stokes spectra taking into account only the effect of magnetic fields on the energy structure and polarization of the hydrogen levels. Having found no definitive evidence of the effects of electric fields in the observed Stokes profiles, we then estimated an upper

bound for these fields by calculating the polarization degree under the magnetic field configuration derived in the first step, with the additional presence of a perpendicular (Lorentz type) electric field of varying strength. The inferred direction of the magnetic field on the plane of the sky (POS) approximately aligns to the active region jets and the surge, with magnetic field strengths in the range $10\,\mathrm{G} < B < 640\,\mathrm{G}$ for the surge. Using magnetic field strengths of 70, 200, and 600 G, we obtained upper limits for possible electric fields of 0.04, 0.3, and $0.8\,\mathrm{V\,cm^{-1}}$, respectively. This upper bound is conservative, since in our modeling we neglected the possible contribution of collisional depolarization. Because the velocity of neutral atoms of hydrogen moving across the magnetic field derived from these upper limits of the Lorentz electric field is far below the bulk velocity of the plasma perpendicular to the magnetic field as measured by the Doppler shift, we conclude that the neutral atoms must be highly frozen to the magnetic field in the surge.

Contents

List of Figures

Acknowledgement

I would like to express my sincere gratitude to my supervisor Prof. Kiyoshi Ichimoto, for his continuous encouragement, guidance and inviting me to the spectropolarimetry having the great potential to develop physics. He suggested me to develop a spectropolarimeter in 2009, and have suggested many interesting studies for my research topic. I have a dream that one day, I will give him a great telescope as a present. I would like to also express my deepest gratitude to my parents, brother and sisters for their sincere understandings and generous supports. I am glad if this thesis will be their pleasures.

I would like to thank Dr. Roberto Casini in High Altitude Observatory for kindly supporting me by his deep theoretical insight into polarization of the spectral line. He also provided me a rare opportunity to visit the National Solar Observatory at Sacrament Peak, observe with outstanding instruments, and look at new-generation spectropolarimeter under development. I am grateful to Dr. Reizaburou Kitai, my vice supervisor, who taught me attitude toward research, and he corrected my hazardous attitude. I am also grateful to Prof. Mitsugu Makita, Mr. Satoru Ueno, Mr. Goichi Kimura, Mr. Yoshikazu Nakatani, Mr. Akihito Oi, and Ms. Jyunko Kiyohara for contribution on this thesis. I would like to thank Prof. Kazunari Shibata, Dr. Hiroaki Isobe, Dr. Andrew Hillier, Mr. Shinsuke Takasao, and Mr. Naoki Nakamura for helpful discussion and supporting me by their theoretical insight. ALL of the members of Kwasan and Hida Observatories and the Department of Astronomy are also acknowledged to various supports to my research activities. They give me many helpful comments and suggestion, do office procedure, cook delicious food, clean up my research environment, help to visit Hida Observatory, and they drink and sing with me. Finally, I would like to thank my girlfriend and Blues (cat) for generous supports.

This work was supported by a Grant-in-Aid for Scientific Research (No. 22244013, P.I. K. Ichimoto) from the Ministry of Education, Culture, Sports, Science and Technology of Japan, and by the Grant-in-Aid for the Global COE Program "The Next Generation of Physics, Spun from University and Emergence" from the Ministry of Education, Culture, Sports, Science and Technology (MEXT) of Japan. This grant supported a two-month visit by T.A. at the High Altitude Observatory (HAO) of the National Center for Atmospheric Research (Boulder, CO), where the interpretational work presented in this paper was initiated.

Chapter 1

Breakthrough in Solar Physics by Plasma Diagnostics with Polarimetric Observation

New plasma diagnostics with polarimetric observation open new window of solar physics. Hale [19] discovered a strong magnetic field in a sunspot by observing Zeeman effect in circular polarization in solar spectrum. The discovery makes human aware of the presence of the magnetic field in the universe. The fundamental roles of magnetic fields can be summarized as follows [20]:

- The magnetic field stores and releases energy that produces transient dynamic phenomena.
- The magnetic field transports energy and disturbances from a site where energy is injected to other locations.
- The Lorentz force works as the magnetic pressure and the magnetic tension force that drives bulk motion of plasma.
- The magnetic field guides the plasma motions, while it traps charged particles and inhibit the thermal conduction across it.

In the case of the Sun, it is revealed that the magnetic field is the key physical ingredient behind the solar activity and various solar phenomena.

The magnetic field in solar photosphere, from which continuum light is emitted, is derived from polarimetric observation by using the Zeeman effect (section 2.2.1). Figure 1.1 shows the radial magnetic field averaged over the longitude for each solar rotation during 35 years [1]. The obvious cyclic pattern of the magnetic field in the diagram corresponds to the activity cycle of the sun, and provides the most stringent observational constraints on the solar dynamo model. Figure 1.2 shows map of line-of-sight component of photospheric magnetic field obtained from observations of circular polarization and soft X-ray solar image at the same day. As the soft X-ray image

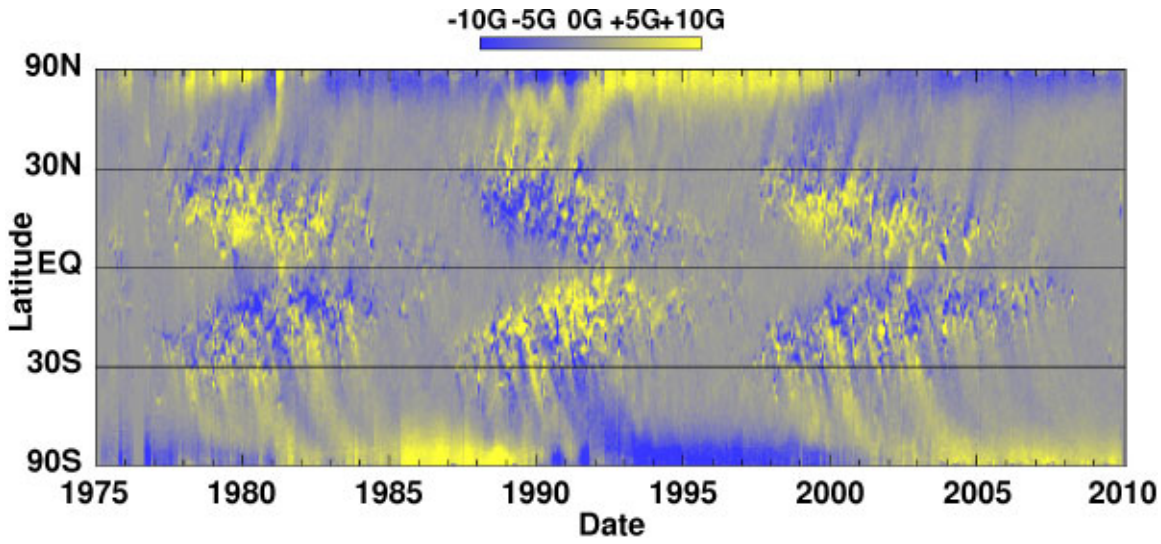

Figure 1.1: A diagram constructed from the longitudinal averaged radial magnetic field obtained from instruments on Kitt Peak National Observatory and the Michelson Doppler Imager (MDI) onboard Solar and Heliospheric Observatory spacecraft (SoHO) [1].

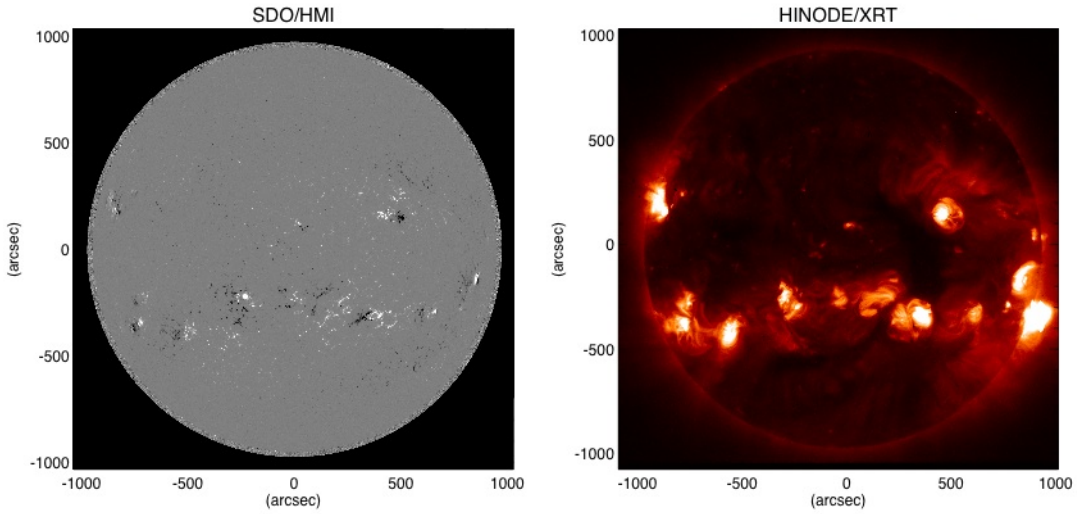

Figure 1.2: *Left:* Line-of-sight component of photospheric magnetic field obtained from observations of circular polarization by Helioseismic and Magnetic Imager (HMI) onboard Solar Dynamics Observatory (SDO) in August 20, 2013. *Right:* Soft X-ray solar image observed by X-Ray Telescope (XRT) onboard HINODE satellite in the same day.

shows distribution of million-degree hot coronal plasma, we can easily recognize that the hot coronal plasma strongly relates with the magnetic field and all regions of strong magnetic field are connected via hot coronal loops with another region of opposite polarity.

The solar dynamo and the coronal heating are both fundamental problems in solar physics and may be briefly summarized as follows: The magnetic energy built up by convection in and below the photosphere is transferred from the photosphere into the heliosphere. During the transfer of energy into the outer layers of the solar atmosphere, i.e., chromosphere and corona, the magnetic energy is partially converted into plasma kinetic and thermal energy, causing various active phenomena and heating in the solar atmosphere. Thus the measurement of the magnetic field is of crucial importance to identify the mechanisms responsible for the both issues and the dynamical phenomena in the solar atmosphere.

We believe that small magnetic structures continue to exist to smaller scale below the presently achievable spatial resolution. Line-ratio technique (section 2.2.1) enables us to measure intrinsic unresolved magnetic field strength from polarimetric observation in two spectral lines, and infers that more than 90 % of the magnetic flux visible in magnetograms has its origin in flux bundles with magnetic filed strength of 1 kG [21]. The size of the flux bundles on the quiet Sun is in the range 10-100 km [22].

High-resolution and high-sensitivity space spectropolarimetric observation discovered polar field structure and transient horizontal magnetic field. From the ground, it is difficult to observe the polar region, because the foreshortening and a strong intensity gradient combined with variable seeing. HINODE gives us a clear map of the polar magnetic field [23], and revealed the existence of many patchy magnetic concentrations rather than a weak extended field (figure 1.3). The intrinsic magnetic field strength in polar region provides observational constraints on the flux-transport dynamo model [24], and the polar field reversal are observed recently [25]. HINODE also revealed the existence of ubiquitous horizontally inclined magnetic fields inside granular cells [26], and the characteristic of the magnetic field for active region and for quiet region are remarkably similar [27]. It suggested that they are generated by common local dynamo process.

Chromosphere, i.e., the boundary layer between the solar corona and the photosphere, is the key layer to understand how magnetic energy is partially converted into plasma kinetic energy during the transfer of energy from photosphere into the outer layers. Various types of dynamics and heating occur in the chromosphere, and they are supposed to be driven by both the hydrodynamic pressure and the magnetic forces (figure 1.4 and 1.5), because the dominant force changes from hydrodynamic pressure to magnetic forces in there. For example, chromospheric jet is triggered by magnetic reconnection, and accelerated by shock [28] (figure 1.4). Prominence is cool, dense object,

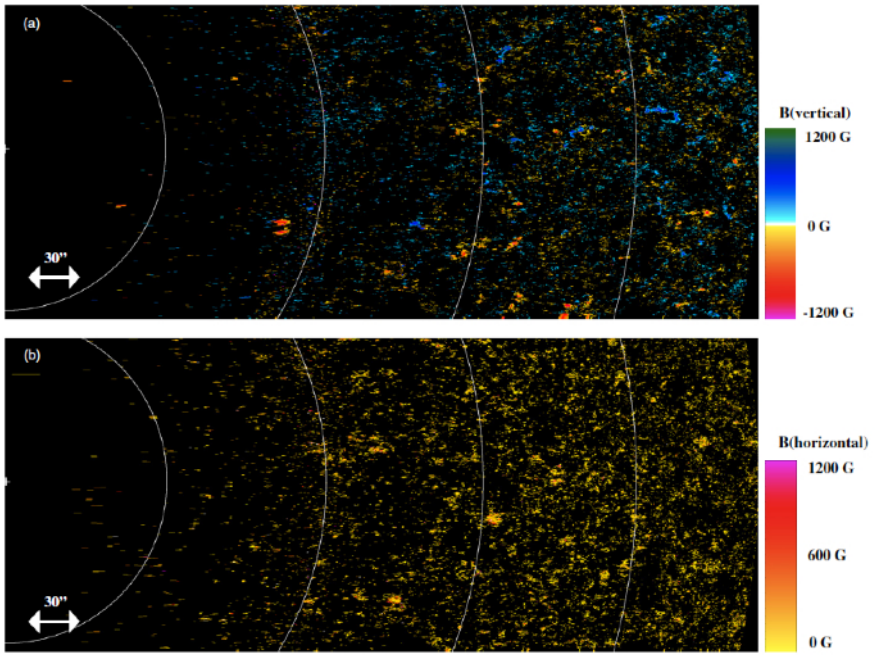

Figure 1.3: Top and bottom plots are vertical and horizontal magnetic field map in solar north pole, respectively [2].

and is supported in and thermally isolated from the surrounding hot, tenuous coronal plasma by Lorentz force. The complex structure in the quiescent prominence outlined by white box in the figure 1.5 is shown to be found by the magnetic Rayleigh-Taylor instability in numerical simulations [29]. Thus, the measurement of the magnetic field in chromosphere is also important for solar physics.

In contrast to the photosphere, it is difficult to diagnose magnetic fields in the solar chromosphere. There are two reasons why it is difficult to diagnose the magnetic fields in the chromosphere. First, the polarization signal produced by the Zeeman effect scales with the ratio of the Zeeman splitting and the Doppler width, and the ratio turns out to be very small for chromospheric lines. Second, the interpretation of the polarization in chromospheric lines is complicated, because polarization mechanism in the chromosphere is not only the Zeeman effect but also, for example, coherent scattering (section 2.2.3) modified with the Hanle effect (section 2.2.5).

Recent progress in the modeling of scattering polarization [30, 12, 31] and in the development of increasingly sensitive spectropolarimetric instrumentation [32, 33, 34] enables us to measure the chromospheric magnetic field by interpreting the observed polarization in terms of the Zeeman and Hanle effects. Recently, the magnetic fields of some types of chromospheric phenomena have been measured, for instance, in filaments [30], prominences [35, 36, 37], spicules [38, 39], and in regions of emerging magnetic flux [40]. Such direct measurements of magnetic field in chromospheric structures are expected to open the new era of research for the physics of chromospheric dynamics.

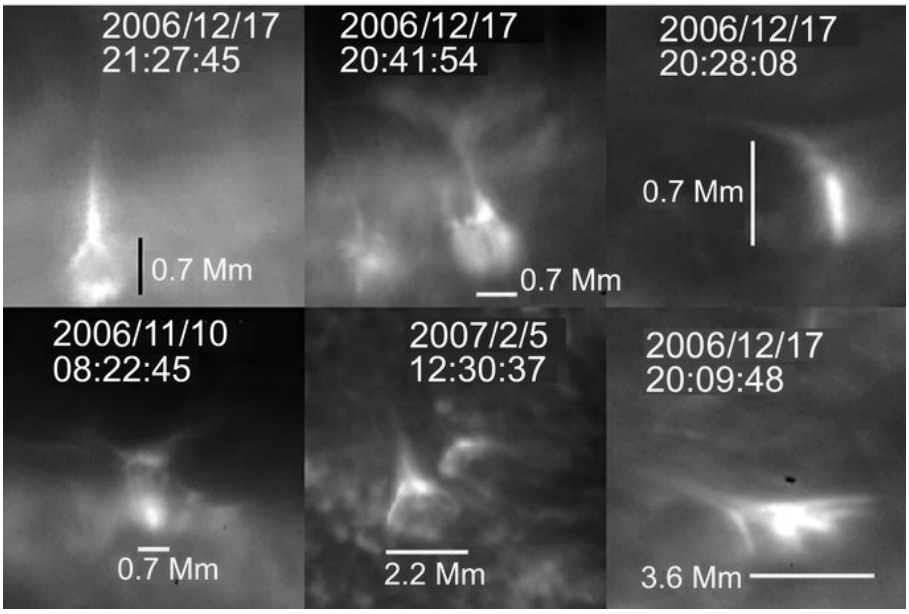

Figure 1.4: Snapshot images of chromospheric jets observed with the CaII broadband filter of the Solar Optical Telecope (SOT) onboard HINODE satellite [3].

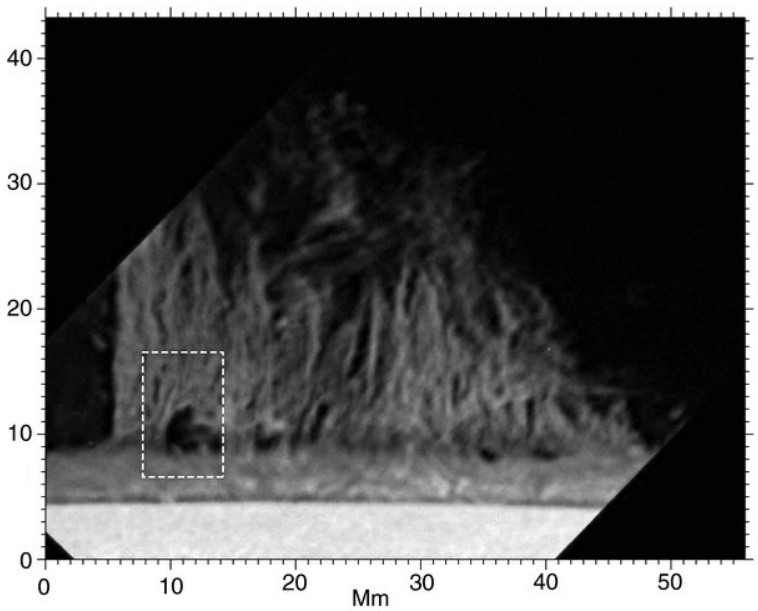

Figure 1.5: Snapshot images of quiescent prominence in Hα observed by the SOT [4]. The white dashed box outlines the complex structure.

In corona, magnetic forces is much stronger than hydrodynamic pressure, and it controls static and dynamic behaviors of the plasma. Linear polarization measurements of the Hanle effect succeeded in mapping the direction of coronal magnetic fields (figure 1.6) [41]. However, obtaining the magnetic field strength is difficult, because weak-field ($\sim$ 10 G) and high-temperature ($\sim$ 10^6 K) coronal plasma produce small circular polarization signal with the Zeeman effect, and Henle effect in coronal emission lines is insensitive to the field strength (Hanle saturation). Furthermore, since the linear polarization produced by resonant scattering is typically 2 orders of magnitude larger than that of the circular polarization in the coronal spectral line, we need high accuracy in calibration of instrumental crosstalk from the linear polarization to the circular polarization to detect circularly polarized Zeeman splitting signature. Lin et al. [42, 6] have succeeded in measuring the weak circular polarization profiles resulting from the longitudinal Zeeman effect, and obtained a two-dimensional map of line-of-sight magnetic flux density in corona by using an reflecting coronagraph and optical fiber-bundle imaging spectropolarimeter (Fugure 1.7).

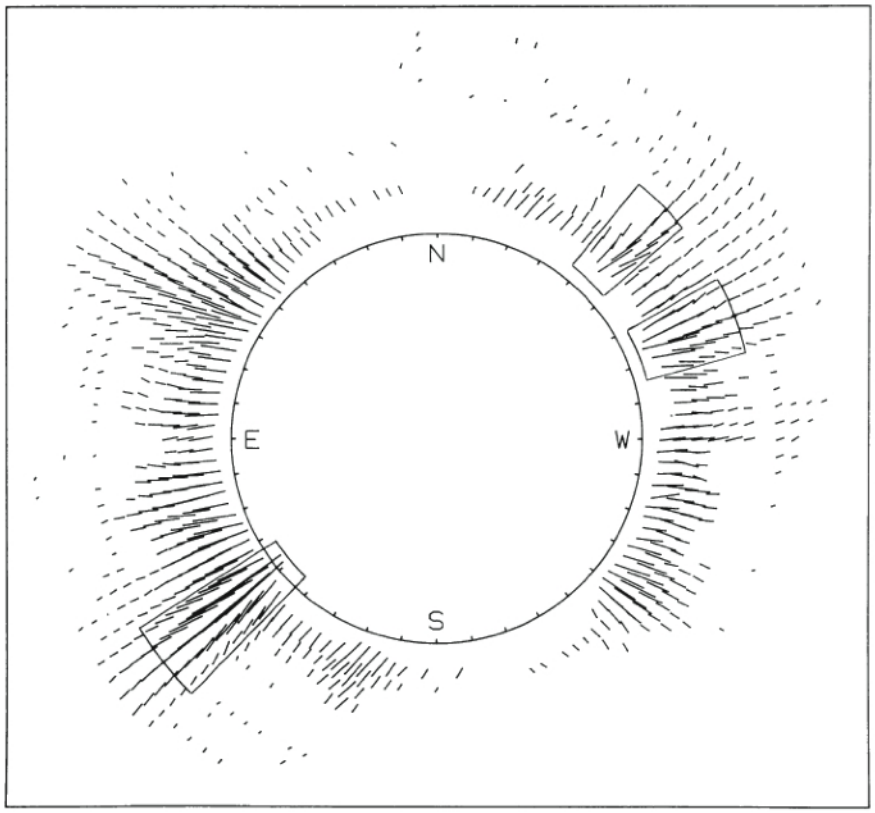

Figure 1.6: Map of linear polarization degree (the line length) and the orientation in 10747 Å[5].

Stalk effect (Section 2.2.2) would enable us to diagnose an electric field induced, for example, when neutral atoms move across a magnetic field [43]. Moran & Foukal [44] and Foukal & Behr [45] estimated the electric field in post flare loops and prominences

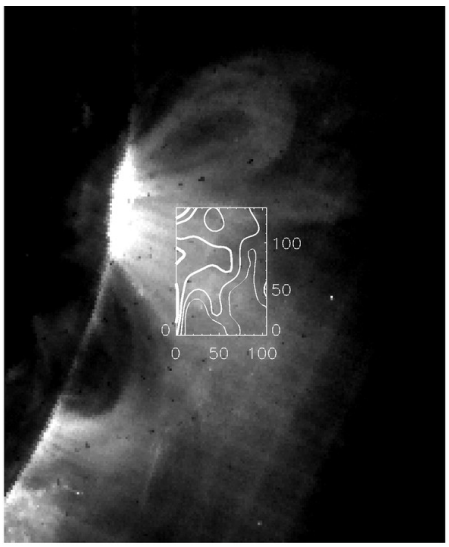

Figure 1.7: Contour map of line-of-sight coronal magnetic flux density obtained from spectropolarimeteric observation in Fe XIII overplotted on the EIT Fe XV image. The thick contour corresponds to 4 G, with additional contours corresponding to 2, 0, -2 G [6].

by studying the line width variation of the linear polarization profile between two orthogonal states of polarization. However the study of electric fields in solar plasmas has been given little attention. This is partially due to the fact that appreciable quasi-static electric fields on macroscopic spatial scales are unlikely in the solar atmosphere, since the relaxation time for the electric charge is very short in the highly conductive solar atmosphere. Electric fields generated in magnetic reconnection events occur at spatial scales far smaller than the spatial resolution of current spectropolarimetric instrumentation. On the other hand, the spatial scale of Lorentz electric fields associated with plasma motions across the magnetic field can be large enough to be resolved with existing solar telescopes, and the associated Stark effect can be detected in a weakly ionized plasma that is able to reach sufficient bulk velocities across the magnetic field. In the followings, we discuss the importance of electric field to study solar physics.

Electric field in inertial reference frame of plasma $\vec{E}'$ is described in inertial reference frame of observer as

$$\vec{E}' = \vec{E} + \frac{1}{c}\vec{v} \times \vec{B}, \tag{1.1}$$

where $\vec{E}$ is electric field, $\vec{B}$ is magnetic field, c is speed of light, $\vec{v}$ is plasma velocity in inertial reference frame of observer. Electric field is generated by charged particle, and also generated on particles that move across the magnetic field. Electric field accelerates charged particle and heats plasma through its resistivity. Electric field also diffuse magnetic field, since substituting $\vec{E}$ into the Maxwell-Faladay equations with

helps of $\vec{E}' = \eta\vec{J}$ and Ampére's circuital law leads to

$$\frac{\partial \vec{B}}{\partial t} = \vec{\nabla} \times (\vec{v} \times \vec{B}) - c\vec{\nabla} \times \vec{E}' \tag{1.2}$$

$$= \vec{\nabla} \times (\vec{v} \times \vec{B}) + \frac{\eta c^2}{4\pi}\nabla^2\vec{B}, \tag{1.3}$$

where η is resistively.

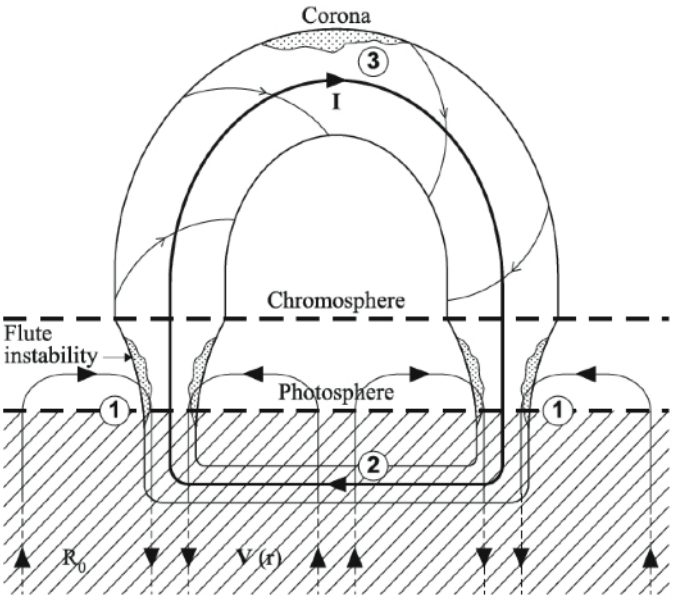

Figure 1.8: Cartoon model of electric dynamic-current-field acceleration [7].

Non-thermal gyro-synchrotron emission at radio wavelengths and bremsstrahlung hard X-rays are observed from solar flares. How and where the energetic electrons are accelerated is one of the most important problems in solar physics. Wide variety of acceleration mechanisms are considered, such as electric dynamic-current-field acceleration [7], stochastic acceleration [46], shock acceleration [47], betatron acceleration [48], and so on. Electric dynamic-current-field acceleration may be occur along flare loop or on current sheet in reconnection region. Figure 1.8 shows cartoon model of electric dynamic-current-field acceleration along flare loop. Neutral hydrogen atoms in convective plasma flows carries the ion, while electrons are more strongly frozen in the magnetic field. The charge separation generates the electric field and drive current in coronal loop from one foot point to the other and closes in the photosphere. Zaitsev et al. [7] estimated the electric field of $\sim 1.2 \times 10^{-3}\,\mathrm{V\,cm^{-1}}$.

In addition, since electric field acts on neutral atoms that move across the magnetic field, the field enable us to study the dynamical coupling between neutrals and ions in the plasma. Since ion is generally frozen in the magnetic field in solar plasma, the eq. (1.2) is reduced as

$$\frac{\partial \vec{B}}{\partial t} = \vec{\nabla} \times (\vec{v}_\mathrm{i} \times \vec{B}), \tag{1.4}$$

where $\vec{v}_{\rm i}$ is ion velocity. In other hand, if the neutral is not frozen in the magnetic field, the eq. (1.2) is reduced as

$$\frac{\partial \vec{B}}{\partial t} = \vec{\nabla} \times (\vec{v}_{\rm n} \times \vec{B}) - c\vec{\nabla} \times \vec{E}', \tag{1.5}$$

where $\vec{v}_{\rm n}$ is neutral velocity. Substitution of eq. (1.4) into eq. (1.5) leads to

$$\vec{E}' = \frac{1}{c}(\vec{v}_{\rm n} - \vec{v}_{\rm i}) \times \vec{B}. \tag{1.6}$$

The difference of velocities between ion and neutral have an effect on the damping of Alfvén and fast magnetohedrodynamic waves in prominence (fig. 1.5) and corona (e.g. fig. 1.2) [49, 50, 51, 52], energy flux of Alfvén wave [53], cut-off frequency of magnetohedrodynamic wave [54], and magnetic reconnection (fig. 1.4) [55, 56, 57, 58].

Impact polarization (Section 2.2.4) would enable us to diagnose anisotropy of velocity distribution of particles that happens in heat conduction or accelerated high-energy particles which penetrate into the chromosphere. Linear polarization of the Hα line emission of solar flares have been reported [59].It is interpreted as impact polarization. Direction and magnitude of the linear polarization depends on the energy of precipitating high-energy particles. Observing the impact polarization enable us to measure the energy and the velocity distribution of accelerated high-energy particles, and the informations are important to study particle acceleration mechanism.

The light is linearly polarized along beam when the energy of the particles lower than a threshold ($\sim$ 200 eV for electrons and $\sim$ 200 keV for protons), and perpendicular to the beam when the energy of the particles larger than the threshold. Thus the direction of the impact polarization depends on the species of particles (electrons or protons). One of implication from hard X-ray and gamma-ray observation is electrons and protons are accelerated on different magnetic field, or they propagate differently along the flux tubes. Figure 1.9 shows hard X-ray and gamma-ray contour observed by Reuven Ramaty High Energy Solar Spectroscopic Imager (RHESSI) over on a Transition Region And Coronal Explorer (TRACE) 195Å coronal image in a large flare [60]. The gamma-ray point source in the neutron capture line at 2.223 MeV are displaced by as much as 20" from hard X-ray point source from electron in some cases. Simultaneous observation between the impact polarization and RHESSI would help to solve the problem how the electrons and the protons accelerate.

In the following, I describe polarization processes of spectral line (Chap. 2), development of a spectropolarimeter of Domeless Solar Telescope at Hida Observatory (Chap. 3), measurement of magnetic and electric fields of chromospheric jets by using the developed spectropolarimeter (Chap. 4), and finally I summarize the thesis (Chap. 5). In the developing the spectropolarimeter, I installed achromatic waveplate, a fast and high sensitive CCD camera, an infrared camera, and a trigger system, I developed software of a remotely controllable turret accommodating linear polarizer,

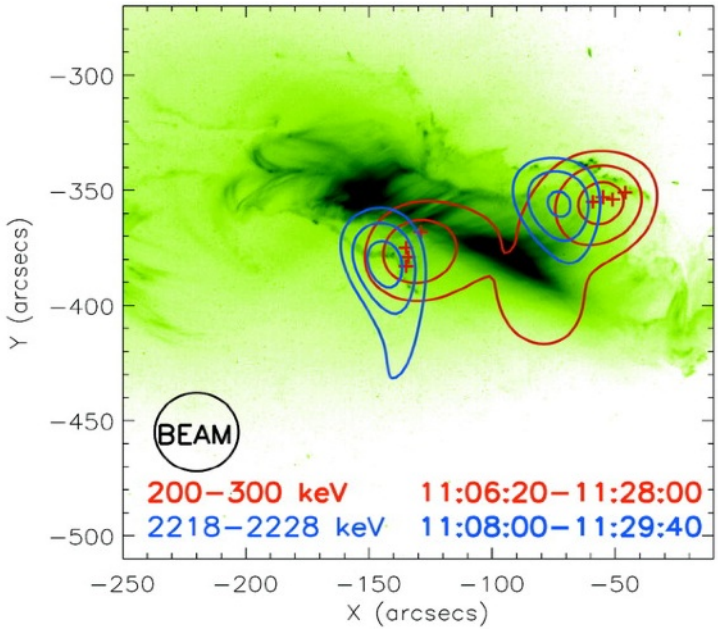

Figure 1.9: Hard X-ray and gamma-ray contours on a TRACE coronal image of the 28 October 2003.

and I calibrated instrumental polarization of the telescope in 400 - 1100 nm. In the measurement of magnetic and electric fields, I observed chromospheric jets with helps of K. Ichimoto, S. Ueno, and A. Oi, I derived magnetic field of chromospheric jets by using a code developed by R. Casini, which calculates polarization profile, and I determined upper limit of electric field by comparison of observed polarization degree with polarization degree as function of the electric field strength calculated by R. Casini.

Chapter 2

Polarization of Spectral Line

Light, electromagnetic wave, is oscillations of $\boldsymbol{E}$ and $\boldsymbol{B}$ in phase lying in a plane perpendicular to the direction of propagation. As $\boldsymbol{E}$ and $\boldsymbol{B}$ are always perpendicular to each other, a description of the wave can be given either specifying its $\boldsymbol{E}$ or alternative. In a given plane perpendicular to the direction of propagation, the tip of the specifying field traces out an elliptic, circle, or a single line. Polarization is the wave oscillating with a directivity.

The quantum of the light is photon of which the magnitude of spin angular momentum is $\sqrt{2}$ and its component, s, along propagation direction is ± 1, where the factor of Planck constant divided by 2π is ignored. The photon with positive s and negative s is circular polarized in right-handed and left-handed, respectively, from the point view toward the source. Linear and elliptic polarization is represented by coherent superposition of right-handed and left-handed circular polarization.

Each photon is completely polarized. However, we observe partial polarized light, namely, incoherent superposition of mutually uncorrelated photons with different polarization state, because the different photons in a stellar atmosphere arise from independent atomic process. Thus, observed polarization in ensemble of photons reflects anisotropy of fields at the light source or medium where atomic radiation process work, unless we distinguish each photon in the light.

2.1 Tools of representation

2.1.1 Jones vector

In a given plane perpendicular to the propagation direction of the light, the electric field oscillates

$$\begin{aligned} E_x(t) &= \mathrm{Re}(\, E_1\, e^{-i(\omega t+\phi_1)}\,) \\ E_y(t) &= \mathrm{Re}(\, E_2\, e^{-i(\omega t+\phi_2)}\,), \end{aligned} \tag{2.1}$$

where E_1, E_2, ϕ_1, and ϕ_2 are four positive constants specifying the amplitudes and phases of the wave in the plane whose orthogonal axes are x and y, and where ω, and t have the usual meaning of angular frequency and time, respectively. The Jones vector

$\boldsymbol{J}$ is simply defined as

$$\boldsymbol{J} = \begin{pmatrix} E_1\, e^{-i\phi_1} \\ E_2\, e^{-i\phi_2} \end{pmatrix}. \tag{2.2}$$

The effect of a medium on the light can be described by a 2×2 complex matrix $\boldsymbol{\omega}$ operating on $\boldsymbol{J}$:

$$\boldsymbol{J}' = \boldsymbol{\omega}\boldsymbol{J}. \tag{2.3}$$

As the Jones vector represents a coherent wave, it is able to describe interference as its summation. By contrast, it can not describe a partially polarized light.

2.1.2 Stokes vector

The 2×2 coherency matrix $\boldsymbol{D}$ is directly obtained from the Jones vector by

$$\begin{aligned} \boldsymbol{D} &= \boldsymbol{J}\boldsymbol{J}^{\dagger} && (2.4) \\ &= \begin{pmatrix} E_1^2 & E_1E_2e^{-i(\phi_1-\phi_2)} \\ E_1E_2e^{-i(\phi_2-\phi_1)} & E_2^2 \end{pmatrix}, && (2.5) \end{aligned}$$

where $\boldsymbol{J}^{\dagger}$ is transposition and complex conjugation of $\boldsymbol{J}$. The averaging of $\boldsymbol{D}$ over a statistical ensemble of photons (hereafter we represent it as D) represents the incoherent superposition of the photon states, since phase factors $e^{-i\omega t}$ disappear by $\boldsymbol{J}\boldsymbol{J}^{\dagger}$. Thus coherency matrix is able to describe partially polarized light.

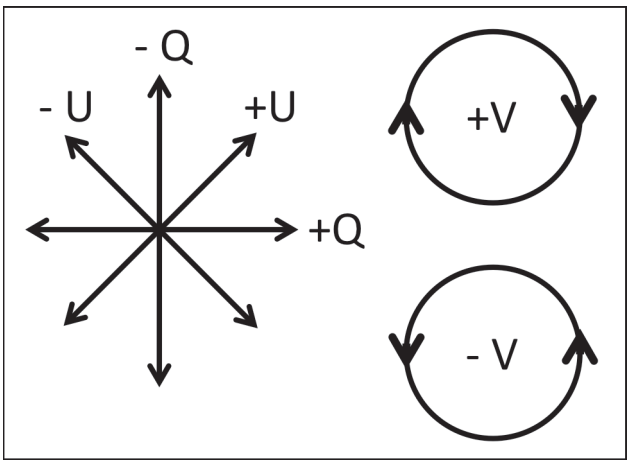

Figure 2.1: The definition of the Stokes vector.

The coherency matrix can be written as

$$\boldsymbol{D} = \frac{1}{2}\begin{pmatrix} I+Q & U+iV \\ U-iV & I-Q \end{pmatrix}, \tag{2.6}$$

$$\begin{aligned} I &= \left\langle E_1^2 \right\rangle + \left\langle E_2^2 \right\rangle && (2.7) \\ Q &= \left\langle E_1^2 \right\rangle - \left\langle E_2^2 \right\rangle && (2.8) \end{aligned}$$

$$U = \left\langle E_1 E_2 \{ e^{-i(\phi_2 - \phi_1)} + e^{-i(\phi_1 - \phi_2)} \} \right\rangle \tag{2.9}$$

$$V = \left\langle i E_1 E_2 \{ e^{-i(\phi_2 - \phi_1)} - e^{-i(\phi_1 - \phi_2)} \} \right\rangle \tag{2.10}$$

which can be cast into a more synthetic form. I correspond to intensity of the light, Q, U are subtraction of the intensity between orthogonal linear polarizations, and V is subtraction of the intensity between right and left circular polarizations (figure 2.1). The Stokes vector $\boldsymbol{S}$ is simply defined as

$$\boldsymbol{S} = \begin{pmatrix} I \\ Q \\ U \\ V \end{pmatrix}. \tag{2.11}$$

In this paper, an axis which rotate 45° from positive Q in counterclockwise looking at the source is defined as positive U, and the right circular polarization, when an electric vector rotates clockwise looking at the source is defined as positive V.

2.1.3 Mueller matrix

Mueller matrix is 4×4 matrix formalized for calculating the effect of a medium on the Stokes vector, unless the effect of a medium is non-linear (e.g. laser experiment). The propagation of the polarization through an optical system is described by the product of the Mueller matrices of individual optical elements in proper order. Rotation matrix of the coordinate may be included if necessary. Each Mueller matrix of the optical elements and rotation matrices of coordinates are described as bellows.

Rotation of coordinate is written as

$$\mathbf{R}(\theta) = \begin{pmatrix} 1 & 0 & 0 & 0 \\ 0 & \cos 2\theta & \sin 2\theta & 0 \\ 0 & -\sin 2\theta & \cos 2\theta & 0 \\ 0 & 0 & 0 & 1 \end{pmatrix}, \tag{2.12}$$

where a plus sign of the rotation angle θ indicates a counterclockwise rotation looking at the light coming to. The Mueller matrix of linear polarizer is described as

$$\mathbf{P} = \frac{1}{1+p} \begin{pmatrix} 1 & p & 0 & 0 \\ p & 1 & 0 & 0 \\ 0 & 0 & \sqrt{1-p^2} & 0 \\ 0 & 0 & 0 & \sqrt{1-p^2} \end{pmatrix}, \tag{2.13}$$

where p is the difference of reflectivity between linear polarizations which are parallel and perpendicular to the reference axis that defines the positive Q. The Mueller matrix of linear retarder referring to the fast axis is represented as

$$\mathbf{D} = \begin{pmatrix} 1 & 0 & 0 & 0 \\ 0 & 1 & 0 & 0 \\ 0 & 0 & \cos\delta & \sin\delta \\ 0 & 0 & -\sin\delta & \cos\delta \end{pmatrix}, \tag{2.14}$$

where δ is the retardation.

2.1.4 Density matrix

The Schrödenger equation

$$i\hbar\frac{\partial}{\partial t}\left|\psi\right\rangle = \hat{H}\left|\psi\right\rangle, \tag{2.15}$$

leads time variation of the wavefunction $|\psi\rangle$, where $\hat{H}$ is the Hamiltonian operator. The wavefunction $|\psi\rangle$ are expanded in terms of the eigenstates of the sistem $|n\rangle$ as

$$\left|\psi\right\rangle = \sum_n c_n \left|n\right\rangle, \tag{2.16}$$

where c_n is complex coefficient. For example, single photon has wavefunction of the form of

$$\left|\psi\right\rangle = c_R \left|R\right\rangle + c_L \left|L\right\rangle, \tag{2.17}$$

where $|R\rangle$ ($|L\rangle$) is the eigenstate in the right (left) circularly polarized photon. However the formalism of wavefunction cannot describe the superposition of the states in a statistical ensemble in which phase of separate events are uncorrelated. It can describe Jones vector, but cannot do Stokes vector.

Density matrix operator $\hat{\rho}$ for a statistical ensemble is defined as

$$\hat{\rho} \equiv \sum_i p_i \left|\psi_i\right\rangle \left\langle\psi_i\right|, \tag{2.18}$$

where p_i is the probability of finding the system in the pure state $|\psi_i\rangle$. Time variation of the density matrix operator is given with help of eq. (2.15) as

$$\frac{\partial\hat{\rho}}{\partial t} = \frac{1}{i\hbar}[\hat{H},\hat{\rho}], \tag{2.19}$$

where the square brackets on the right hand side denote a commutator. The elements $\rho_{nn'}$ of the density matrix operator $\hat{\rho}$ are given by

$$\rho_{nn'} = \left\langle n\right|\hat{\rho}\left|n'\right\rangle. \tag{2.20}$$

The diagonal elements of the density matrix operator ρ_{nn} gives the probability of $|n\rangle$, while the off-diagonal elements of the density matrix operator ρ_{nm} means quantum interference between $|n\rangle$ and $|m\rangle$. The density operator is Hermitian ($\rho_{mn} = \rho^*_{nm}$), where $*$ indicate complex conjugate. The expectation value of the operator $\hat{X}$ is

$$\left\langle\hat{X}\right\rangle = \sum_i p_i \left\langle\psi_i\right|\hat{X}\left|\psi_i\right\rangle = \mathrm{Tr}\left(\hat{\rho}\hat{X}\right) = \mathrm{Tr}\left(\hat{X}\hat{\rho}\right), \tag{2.21}$$

where Tr denote trace of the matrix.

Spherical tensors of the density matrix is obtained from standard matrix as

$$\rho^K_Q(\alpha J,\alpha' J') = \sum_{MM'}(-1)^{J-M}\sqrt{2K+1}\begin{pmatrix} J & J' & K \\ M & -M' & -Q\end{pmatrix}\rho(\alpha LJ,\alpha' L' J'), \tag{2.22}$$

where $K = 0, 1, \cdots$ is the rank of tensor, where $Q = -K, -K+1, \cdots, K-1, K$, where

$$\begin{pmatrix} J & J' & K \\ M & -M' & -Q \end{pmatrix}$$

is the 3-j symbol, and where Q L, J, and M is orbital, total, and magnetic angular quantum number, respectively. Equation (2.22) can be easily inverted as

$$\rho(\alpha LJ, \alpha' L' J') = \sum_{KQ} (-1)^{J-M} \sqrt{2K+1} \begin{pmatrix} J & J' & K \\ M & -M' & -Q \end{pmatrix} \rho_Q^K(\alpha J, \alpha' J'). \quad (2.23)$$

The advantage of the spherical tensors is in its simplicity when the system has a sort of symmetry, i.w., when there exists some symmetry, many components of the matrix vanish. The element with K of 0, odd number, and even number are quantity of the population, atomic orientation, and atomic alignment, respectively. The atomic orientation and alignment are expressed in section 2.2.

2.1.5 Rotation matrix

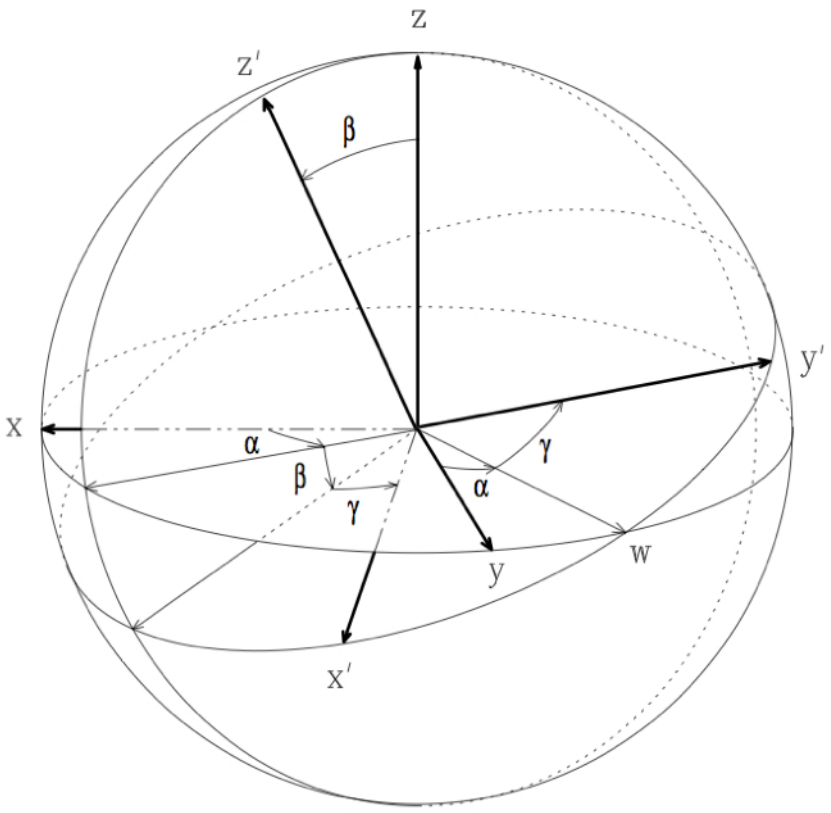

Figure 2.2: Definition of the Euler angles.

When one rotate quantization axis with the Euler angles $\alpha\beta\gamma$ defined in figure 2.2, the density matrix elements in new coordinates system $\rho_{M'N'}$ are formally calculated

from density matrix elements in old coordinates system ρ_{MN} as

$$\rho_{M'N'} = \sum_{MN} D^{J*}_{MM'}(\alpha\beta\gamma) D^{J}_{NN'}(\alpha\beta\gamma) \rho_{MN}, \tag{2.24}$$

where rotation matrix D^J_{MN} is

$$\begin{aligned} D^J_{MN}(\alpha\beta\gamma) &= e^{-i(\alpha M+\gamma N)} \\ &\times \sum_k (-1)^{k-M+N} \frac{\sqrt{(J+M)!(J-M)!(J+N)!(J-N)!}}{(J+M-k)!k!(J-k-N)!(k-M+N)!} \\ &\times \left(\cos\frac{\beta}{2}\right)^{2J-2k+M-N} \left(\sin\frac{\beta}{2}\right)^{2k-M+N}, \end{aligned} \tag{2.25}$$

where ! denotes factorials. In spherical tensors representation, we obtained the density matrix

$$[\rho^K_Q(\alpha J, \alpha' J')]_{\rm new} = \sum_{Q'} [\rho^K_{Q'}(\alpha J, \alpha' J')]_{\rm old} D^K_{Q'Q}(\alpha\beta\gamma)^*, \tag{2.26}$$

where rotation matrix in spherical tensors representation is

$$D^K_{QQ'}(\alpha\beta\gamma)^* = \sum_{MM'NN'} (2K+1) \begin{pmatrix} J & J' & K \\ M & M' & Q \end{pmatrix} \begin{pmatrix} J & J' & K \\ N & N' & Q' \end{pmatrix} D^J_{MN}(\alpha\beta\gamma) D^{J'}_{M'N'}(\alpha\beta\gamma). \tag{2.27}$$

Scattering phase matrix $T^K_Q(i, \vec{\Omega})$ is expressed in terms of the rotation matrix as

$$T^K_Q(i, \vec{\Omega}) = \sum_P t^K_P(i) D^K_{PQ}(\alpha\beta\gamma), \tag{2.28}$$

where

$$t^K_P(i) = \sum_{\alpha\beta=\pm1} \frac{1}{2} (\hat{\sigma}_i)_{\alpha\beta} \sqrt{3(2K+1)} \begin{pmatrix} 1 & 1 & K \\ \beta & -\alpha & -P \end{pmatrix}, \tag{2.29}$$

and where $\hat{\sigma}_i$ are the Pauli spin matrixes.

2.2 Polarization process in spectral lines

Radiation process in spectral lines is bound-bound transition between the lower and upper energy levels of a discrete system such as an atom, ion or molecule. Since summation of the component of angular momentum along the quantum axis is conserved in the system of the interaction of the photon and the matter, the component of the spin angular momentum of the photon created by the bound-bound transition depends on the component of the total angular momentum, magnetic quantum number M, of the lower and upper energy levels of the matter. The polarization created by bound-bound transition with $\Delta M = 1$ and -1 is left-handed and right-handed circular polarization, respectively. If the ΔM equals zero, the photon is linearly polarized along the quantization axis and does not propagate along the axis.

Several processes can generate polarization in spectral lines in response to the presence of magnetic and electric fields in the radiation emitting plasma. The Zeeman and

Stark effects are produced by the energy separation of the atomic levels into multiple sublevels due to the shift of the potential energy of the radiating atom in the external fields. As the splitted components have different polarization properties, this results in a wavelength dependent polarization across the spectral line. In the absence of velocity or field gradients in the emitting plasma, the broadband (i.e., wavelength integrated) polarization from the Zeeman and Stark effect vanishes. In contrast, in the presence of *atomic polarization* (i.e., population imbalances and quantum interferences among the magnetic sublevels; e.g., Landi Degl'Innocenti & Landolfi [61]), the emitted (scattered) radiation is typically characterized by a non-vanishing broadband polarization. The two dominant characteristics of atomic polarization are atomic *alignment* and *orientation*. Atomic alignment is a state of population imbalances between magnetic sublevels with different absolute values of their magnetic quantum numbers. Atomic orientation is characterized by population imbalances between sublevels with positive and negative magnetic quantum numbers. The effects of atomic alignment and orientation in the scattered radiation are observed in the form of broadband linear and circular polarization, respectively. In the process of radiation scattering, the anisotropy of the incident radiation field produces atomic alignment, and the scattered light is therefore linearly polarized, with a magnitude depending on the scattering geometry. The presence of a magnetic or electric field produces a relaxation of the atomic coherence among the magnetic sublevels resulting in a modification of the polarization (typically, depolarization and rotation) of the scattered radiation, known as the Hanle effect. Strong magnetic or electric fields also cause a conversion of atomic alignment into atomic orientation when the energy splitting of the sublevels induced atomic level crossings (A-O mechanism) [62, 63, 64, 65, 14]. Collisions of the scattering atoms with free electrons and protons tend to reduce the atomic level polarization. For the typical density of the upper solar chromosphere, collisional transitions between the fine-structure levels pertaining to the same Bohr level of the neutral hydrogen may play a significant role in the depolarization process [66, 67, 68].

2.2.1 Zeeman effect and Paschen-Back effect

Zeeman [69] discovered an effect of splitting a spectral line into several components in the presence of a static magnetic field. The static magnetic field makes the angular momentum of electron in an atomic system precess around the magnetic field, and perturbs the energy of the electron. The change of the energy of the electron cause the spectral line splitting into several components. We can distinguish between Zeeman and Paschen-Back regimes depending on the magnitude of splitting of the energy levels by the perturbation of the static magnetic field H_B and on the magnitude of the fine-structure spliting $H_{\rm LS}$. Zeeman regime is $H_B \ll H_{\rm LS}$ in which energies of the sub-levels are linear in the applied field. When the magnetic field becomes sufficiently strong, so

that $H_B \sim H_{\rm LS}$ or $H_B \gg H_{\rm LS}$, some of the energy levels of distinct fine structure are strongly mixed, and energies of the sub-levels are not linear in the applied field. This is the Paschen-Back regimes.

The Hamiltonian for an electron in an external electromagnetic field that is characterized by the vector potential $\vec{A}$, a central electrostatic potential V, and perturbation resulting in the fine structures $H_{\rm LS}$ is

$$H = \frac{1}{2m}(\vec{p} + \frac{e_0}{c}\vec{A})^2 + V + H_{\rm LS}, \tag{2.30}$$

where m, $\vec{p}$, and e_0 is the mass, the momentum, and the absolute value of charge of the electron respectively. The vector potential for the magnetic filed can be expressed as

$$\vec{A} = -\frac{1}{2}(\vec{r} \times \vec{B}), \tag{2.31}$$

which can be verified by $\vec{B} = \nabla \times \vec{A}$ when the spatial derivatives of $\vec{B}$ can be neglected in atomic dimensions. After a standard vector transformation, we obtain

$$\vec{A} \cdot \vec{p} = \frac{1}{2}\vec{B} \cdot (\vec{r} \times \vec{p}) = \frac{1}{2}\vec{B} \cdot \vec{L}, \tag{2.32}$$

where $\vec{L}$ is the orbital angular momentum. The relativistic Dirac theory gives the spin angular momentum S of the electron, and the ratio between the magnetic momentum and the angular momentum for the spin of the electron is twice as large as compared with the orbital angular momentum. Thus, we expand the Hamiltonian eq. (2.30) as

$$H = \frac{1}{2m}\vec{p}^2 + V + H_{\rm LS} + \frac{e_0 h}{4\pi mc}(\vec{L} + 2\vec{S}) \cdot \vec{B} + \frac{e_0^2}{8mc^2}(\vec{B} \times \vec{r}). \tag{2.33}$$

The Hamiltonian of the perturbation due to external magnetic field, H_B, is given by

$$H_B = \frac{e_0 h}{4\pi mc}(\vec{L} + 2\vec{S}) \cdot \vec{B} + \frac{e_0^2}{8mc^2}(\vec{B} \times \vec{r}). \tag{2.34}$$

Second term in the right-hand side of eq. (2.34) is comparable with first term of the equation, if magnetic field strength become 10^{10} G. If we exclude the case of extremely large fields that are found in magnetic white dwarfs or are supposed to exist in neutron stars, we can write the Hamiltonian of the perturbation due to external magnetic field by neglecting the second term in eq. (2.34) as

$$H_B = \frac{e_0 h}{4\pi mc}(\vec{L} + 2\vec{S}) \cdot \vec{B} = \mu_0(\vec{L} + 2\vec{S}) \cdot \vec{B}, \tag{2.35}$$

where μ_0 is called *Bohr magneton* ($\mu_0 = 9.27 \times 10^{-21}\,\mathrm{erg\,G^{-1}}$). Since the magnetic dipole induced by angular momentum of the electron perturbs the energy of the atom, L and S are good quantum numbers.

The matrix elements of the H_B on the basis of the eigenvectors $|\alpha JM\rangle$ of $H_0 (\equiv \frac{1}{2m}\boldsymbol{p}^2 + V + H_{\rm LS})$ is

$$\langle \alpha JM | H_B | \alpha' J' M' \rangle = \mu_0 \langle \alpha JM | (\vec{L} + 2\vec{S}) \cdot \vec{B} | \alpha' J' M' \rangle . \tag{2.36}$$

With helps of the Wigner-Eckart theorem

$$\langle \alpha JM|\, T^k_q \,|\alpha' J' M'\rangle = (-1)^{J'+k+M}\sqrt{2J+1}\begin{pmatrix} J & J' & k \\ -M & M' & q \end{pmatrix}\left\langle \alpha J \parallel \boldsymbol{T}^k \parallel \alpha' J' \right\rangle, \tag{2.37}$$

and a reduced matrix element of the total angular momentum operator

$$\left\langle \alpha J \parallel \vec{J} \parallel \alpha' J' \right\rangle = \delta_{\alpha\alpha'}\delta_{JJ'}\sqrt{J(J+1)}, \tag{2.38}$$

the matrix elements of H_B is given as

$$\begin{aligned}\langle \alpha JM|\, H_B \,|\alpha' J' M'\rangle = \;& \mu_0 B \textstyle\sum_q (-1)^{J'+M+q+1}\sqrt{2J+1}\begin{pmatrix} J & J' & 1 \\ -M & M' & q \end{pmatrix} \\ & \times\Big[\sqrt{J(J+1)}\delta_{\alpha\alpha'}\delta_{JJ'} + \left\langle \alpha J \parallel \vec{S} \parallel \alpha' J' \right\rangle\Big] b_{-q},\end{aligned} \tag{2.39}$$

where b_{-q} for $q = 0, \pm 1$ are spherical components of unit vector in the direction of the magnetic field. When the quantization axis for $\vec{J}$ is along the magnetic field,

$$\begin{aligned}\langle \alpha JM|\, H_B \,|\alpha' J' M'\rangle = \;& \mu_0 B\Big[M\delta_{\alpha\alpha'}\delta_{JJ'} \\ & +(-1)^{J'+M+1}\sqrt{2J+1}\begin{pmatrix} J & J' & 1 \\ -M & M' & 0 \end{pmatrix}\left\langle \alpha J \parallel \vec{S} \parallel \alpha' J' \right\rangle\Big]\delta_{MM'}.\end{aligned} \tag{2.40}$$

The matrix H_B is generally block-diagonal one whose block is characterized by M value, when the quantization axis for $\vec{J}$ is along the magnetic field. In special case when the atomic system is exactly described by the L-S coupling scheme, the matrix elements of the H_B is

$$\begin{aligned}&\langle \beta LSJM|\, H_B \,|\beta' L' S' J' M'\rangle = \mu_0 B\delta_{\beta\beta'}\delta_{LL'}\delta_{SS'}\delta_{MM'}\Big[M\delta_{JJ'} + (-1)^{J+J'+L+S+M} \\ &\times\sqrt{(2J+1)(2J'+1)S(S+1)(2S+1)}\begin{pmatrix} J & J' & 1 \\ -M & M & 0 \end{pmatrix}\begin{Bmatrix} J & J' & 1 \\ S & S & L \end{Bmatrix},\end{aligned} \tag{2.41}$$

on the basis of the eigenvectors $|\beta LSJM\rangle$.

Time averaged H_B is written as

$$H_B = \mu_0(\vec{J} + \left\langle \vec{S} \right\rangle)\cdot\vec{B}, \tag{2.42}$$

because $\vec{S}$ not only precess around $\vec{B}$ but also around $\vec{J}$. As the precession time scale of $\vec{S}$ around $\vec{J}$ is shorter than that of the Larmor precession in the Zeeman regime, $\left\langle \vec{S} \right\rangle$ becomes in parallel to $\vec{J}$. Eq. (2.42) is rewritten

$$H_B = \mu_0 g\,\vec{J}\cdot\vec{B}, \tag{2.43}$$

where the *Landé* factor is given by

$$g = 1 + \frac{\left\langle \vec{J}\cdot\vec{S} \right\rangle}{\vec{J}^2} = 1 + \frac{J(J+1) - L(L+1) + S(S+1)}{2J(J+1)}. \tag{2.44}$$

When the quantization axis is along the magnetic field direction, the time averaged Zeeman Hamiltonian is written as

$$H_B = \mu_0 g\, MB. \tag{2.45}$$

Frequency in a transition between two atomic sublevels which split by the Zeeman effect is given by

$$\begin{aligned} \nu^{JJ'}_{MM'} &= \nu_0 + \frac{\mu_0 B}{h}(g'M' - gM) && (2.46)\\ &= \nu_0 + 1.3996 \times 10^6\, B\,(g'M' - gM), && (2.47) \end{aligned}$$

where ν_0 is the frequency of the unperturbed line in s^{-1}, B is in G, and ν is in s^{-1}. In the visible and infrared, since the shift of the frequency in the transition is much smaller than ν_0, the wavelength of the transition can be written

$$\begin{aligned} \lambda^{JJ'}_{MM'} &= \lambda_0 + \frac{\lambda_0^2 e_0 B}{4\pi m c^2}(g'M' - gM) && (2.48)\\ &= \lambda_0 + 4.6686 \times 10^{-13}\, \lambda_0^2\, B\,(g'M' - gM), && (2.49) \end{aligned}$$

where wavelength is in Å.

The selection rule for electric-dipole transitions allows transition for $\Delta M = M' - M = 0, \pm 1$ and $\Delta J = J' - J = 0, \pm 1$, but forbids a transition with $J = 0 \to 0$. $\Delta M = 0$ gives lineally polarized light in the quantization axis, and $\Delta m = \pm 1$ gives circularly polarized light in the plane perpendicular to the axis.

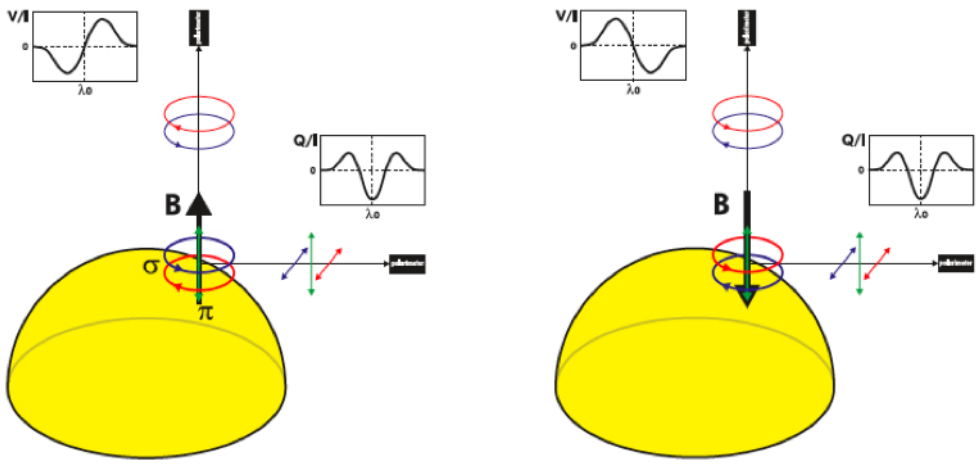

Figure 2.3: Classical representation for the typical Stokes profiles in emission line produced by the Zeeman effect [8].

Emergent line polarization produced by normal Zeeman effect is showed in figure 2.3. When the quantization axis is taken in the direction of the external magnetic field, the polarization created by bound-bound transition with $\Delta M = 1$ and -1 is

left-handed and right-handed circular polarization, respectively (σ component, red and blue circle in the fig. 2.3). If the ΔM is equal to zero, the photon is linearly polarized along the quantization axis and does not propagate along the axis (π component, green arrow in the fig. 2.3). Since the wavelength of the each component is not same due to the Zeeman splitting, this results in a wavelength dependent polarization across the spectral line.

The profile pattern in Stokes-V appears antisymmetric, because the sign of the wavelength shifts depend on the sign of the M in a given magnetic field direction. When the magnetic field direction is flipped, the sign of the Stokes-V pattern changes. The wavelength shifts of the σ components are typically larger than that of the π components, and the pattern in linear polarization is symmetric. When the magnetic field direction is flipped, the pattern in Stokes Q does not change. It means that there is a 180° ambiguity in the full vector measurement of magnetic field with the Zeeman effect.

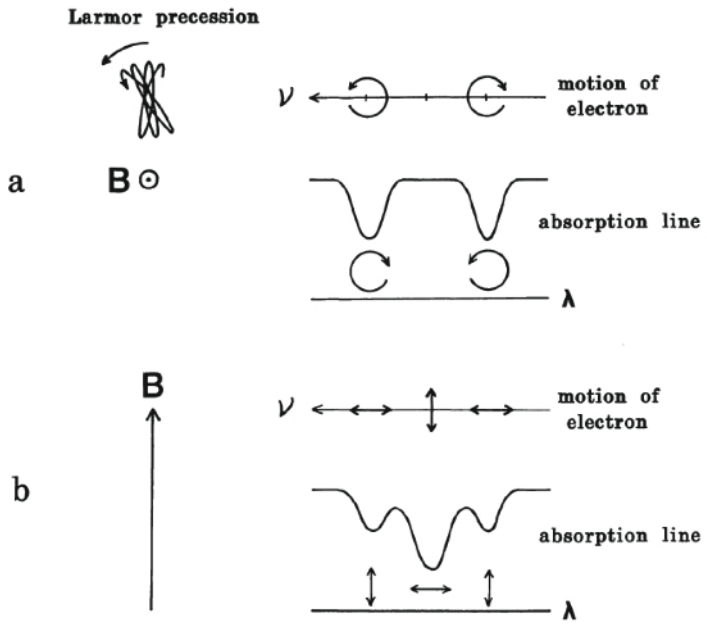

Figure 2.4: Classical representation for the typical Stokes profiles in absorption line produced by the Zeeman effect [9].

In optically thick plasma, the sign of the Stokes profiles in absorption line is opposite to that in the emission line (figure 2.4), because of selective absorption in the Stokes profiles. It is called inverse Zeeman effect. In addition, the optical effect (birefringence) causes rotation of the linear polarization and conversion between linear and circular polarization (magneto-optical effect).

If $I_0(\Delta\lambda)$ is intensity profile solved by non-magnetic transfer equation, intensity

profile for $M = \pm 1$ become

$$I_{\pm}(\Delta\lambda) = I_0(\Delta\lambda \mp \Delta\lambda_H), \tag{2.50}$$

where

$$\Delta\lambda_H = zg\lambda^2 B.$$

When magnetic field directs to the observer, we obtain

$$I = \frac{1}{2}(I_+ + I_-) \sim I_0 + \frac{1}{2}(\Delta\lambda_H)^2 \frac{\partial^2 I_0}{\partial\lambda^2} + \ldots \tag{2.51}$$

$$V = \frac{1}{2}(I_+ - I_-) \sim -\Delta\lambda_H \Big[\frac{\partial I_0}{\partial\lambda} + \frac{1}{6}(\Delta\lambda_H)^2 \frac{\partial^3 I_0}{\partial\lambda^3} + \ldots\Big] \tag{2.52}$$

For weak magnetic field ($\Delta\lambda_H \ll$ spectral line width),

$$I \sim I_0 \tag{2.53}$$

$$V \sim -\Delta\lambda_H \frac{\partial I_0}{\partial\lambda}. \tag{2.54}$$

Stokes V signal is in proportion to the magnetic field strength, and Stokes V has an anti-symmetric profile like the gradient of the Stokes I profile. When magnetic field perpendicular to the observer, we obtain

$$I = \frac{1}{2}(I_0 + \frac{1}{2}I_+ + \frac{1}{2}I_-) \sim I_0 + \frac{1}{4}(\Delta\lambda_H)^2 \frac{\partial^2 I_0}{\partial\lambda^2} + \ldots \tag{2.55}$$

$$Q = \frac{1}{2}(I_0 - \frac{1}{2}I_+ - \frac{1}{2}I_-) \sim -\frac{1}{4}(\Delta\lambda_H)^2 \frac{\partial^2 I_0}{\partial\lambda^2} + \ldots, \tag{2.56}$$

For weak magnetic field, Q gives us

$$Q \sim B^2 \frac{\partial^2 I_0}{\partial\lambda^2}. \tag{2.57}$$

Stokes Q signal scales with B^2, and Stokes Q has symmetric profile like the second derivative of the Stokes I profile.

Observation of the polarization simultaneously in two spectral lines give us information of spatially unresolved magnetic fields. If magnetized plasma is strongly fragmented in a fraction α of the resolution element and the other plasma in the resolution element are not magnetized, Stokes I and V can be given as

$$I = \alpha I_m + (1-\alpha) I_{nm} \tag{2.58}$$

$$V = -\alpha\Delta\lambda_H \Big[\frac{\partial I_{m,0}}{\partial\lambda} + \frac{1}{6}(\Delta\lambda_H)^2 \frac{\partial^3 I_{m,0}}{\partial\lambda^3} + \ldots\Big], \tag{2.59}$$

where index m is for the magnetic and nm is for the non-magnetic components, respectively. The polarization degree of the Stokes V gives us the magnetic flux αB. The line ratio in Stokes V magnitude is written as

$$\frac{V_2}{V_1} \sim \frac{g_2}{g_1}(1 + B^2 \frac{z^2 g^2 \lambda^4}{6} \frac{\partial^3 I_{m,0}}{\partial\lambda^3} / \frac{\partial I_{m,0}}{\partial\lambda} + \ldots). \tag{2.60}$$

Thus the line ratio gives us the intrinsic field strength, independent of the α.

Net circular polarization ($\equiv \int V \mathrm{d}\lambda$) is generated by coupling of velocity gradient with gradient of magnetic field strength [70], inclination [71], and azimuth [72] along the line of sight. The sign of the net circular polarization (NCP) is expected as

$$\mathrm{sign(NCP)} = -\mathrm{sign}\Big(V_{\mathrm{blue}} \frac{\mathrm{d}|B|}{\mathrm{d}\tau} \frac{\mathrm{d}v_{\mathrm{LOS}}}{\mathrm{d}\tau}\Big), \tag{2.61}$$

$$\mathrm{sign(NCP)} = -\mathrm{sign}\Big(V_{\mathrm{blue}} \frac{\mathrm{d}|\cos\gamma|}{\mathrm{d}\tau} \frac{\mathrm{d}v_{\mathrm{LOS}}}{\mathrm{d}\tau}\Big), \tag{2.62}$$

where τ is the optical depth and V_{blue} is the Stokes-V signal in the blue lobe [73]. The inclination γ is zero, when the magnetic field directs to the observer. The line of sight velocity v_{LOS} is defined to be negative, when the velocity vector directs to the observer.

2.2.2 Stark effect

Stark [74] discovered an effect of splitting of lines of *Balmer* series of hydrogen into several components in the presence of an electric field in 1913. Soon after Stark's discovery, Lo Surdo [75] also observed the splitting.

Here, we introduce how the energy level shift in linear Stark effect (a first order perturbation of the atomic level energy). The linear Stark effect is more sensitive to the electric field strength in the field range expected in solar plasma than higher order Stark effect. The linear Stark effect only occurs in hydrogen-like ions, whereas multi-electron atoms tend to show only quadratic (and higher order) energy effects in the presence of an external electric field.

Hamiltonian of the perturbation, H_E, due to external electric field, $\boldsymbol{E}$, is

$$H_E = -\vec{E} \cdot \vec{d}, \tag{2.63}$$

where $\vec{d}$ is the electric-dipole moment. The matrix elements of H_E are calculated as

$$\langle nLSJM|\, H_E \,|nL'SJ'M'\rangle = -E \,\langle nLSJM|\, \vec{e}_E \cdot \vec{d}\,|nL'SJ'M'\rangle\,. \tag{2.64}$$

With a help of Wigner-Eckart theorem (Eq. 2.37), the matrix elements are reduced as

$$\begin{aligned}\langle nLSJM|\, H_E \,|nL'SJ'M'\rangle = \; & -Ea_0e_0(-1)^{S-M'+1}\Lambda(nL,nL')\sqrt{(2J+1)(2J'+1)} \\ & \times \begin{Bmatrix} L & L' & 1 \\ J' & J & S \end{Bmatrix} \sum_Q \begin{pmatrix} J & J' & 1 \\ -M & M' & -Q \end{pmatrix} (\boldsymbol{e_E})_Q,\end{aligned} \tag{2.65}$$

where $(\boldsymbol{e_E})_Q$, for $Q = 0, \pm 1$ are the spherical components of the unit vector of the electric field, a_0 is the *Bohr* radius, e_0 is elementary charge, and

$$\Lambda(nL,nL') \equiv \sqrt{(2L+1)(2L'+1)}\,\langle nL|\, r \,|nL'\rangle \begin{pmatrix} L & L' & 1 \\ 0 & 0 & 0 \end{pmatrix}$$

$$\langle n\,L|\, r \,|n\,L-1\rangle = \frac{2}{3} n\sqrt{n^2-L^2} = \langle n\,L-1|\, r \,|n\,L\rangle\,.$$

When we take the quantization axis in the direction of $\vec{E}$, it is rewritten as

$$\begin{aligned}\langle nLSJM|\, H_E\, |nL'SJ'M'\rangle = \; & -Ea_0e_0(-1)^{S-M'+1}\Lambda(nL,nL')\sqrt{(2J+1)(2J'+1)} \\ & \times \left\{ \begin{array}{ccc} L & L' & 1 \\ J' & J & S \end{array} \right\} \left(\begin{array}{ccc} J & J' & 1 \\ -M & M' & 0 \end{array} \right).\end{aligned} \tag{2.66}$$

Figure 2.5 shows energy level shifts against electric field strength for $n = 2$ and $n = 3$ of neutral hydrogen calculated by equation (2.66). In a weak field strength range where the intrinsic fine structure and Stark splittings are comparable, the energy level shifts is not proportional to the field strength, while the energy level shifts is proportional to the field strength in strong field strength regime.

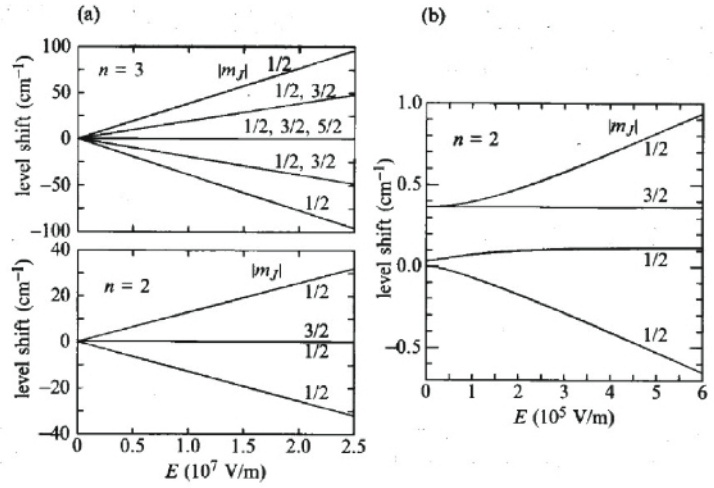

Figure 2.5: Energy level shifts against electric field strength for $n = 2$ and $n = 3$ of neutral hydrogen (a) in a wide field strength range and (b) in a weak field strength range where the intrinsic fine structure and Stark splittings are comparable [10].

In the strong field regime where the level shift is larger than the intrinsic fine structure splittings, level shifts are proportional to the field strength. The wavelength shifts of neutral hydrogen spectral lines are described by the principle quantum numbers (n', n) and parabolic quantum numbers (n'_1, n'_2, m', n_1, n_2, m), where the primes refer to the lower level. The parabolic quantum numbers, n_1 and n_2, are defined as integral numbers which have following relations:

$$n_2, n_1 \geq 0,$$

$$n_2, n_1 \leq n-1,$$

$$|m| = n - 1 - n_1 - n_2.$$

The shift of wavelength of each component from the zero-field position of the line is

$$\Delta\lambda = 6.42 \times 10^{-5}\lambda^2 E\{n(n_2 - n_1) - n'(n'_2 - n'_1)\},$$

where E is in electrostatic units [76]. The splitting of the energy levels, and thus the shift of wavelength, are roughly proportional to the square of the principal quantum number, the square of the wavelength, and the electric field strength [44, 45].

The selection rule permits transition for $\Delta m = 0$, which gives components lineally polarized parallel to the field, and $\Delta m = \pm 1$, which gives components lineally polarized perpendicular to the field.

In the presence of an electric field, level crossing can happen between $\Delta L = 1$ levels that are separated in energy by a difference comparable to the Lamb shift, rather than by the L-S coupling fine structure energy separation, because different L-levels are degenerated in hydrogen-like atom.

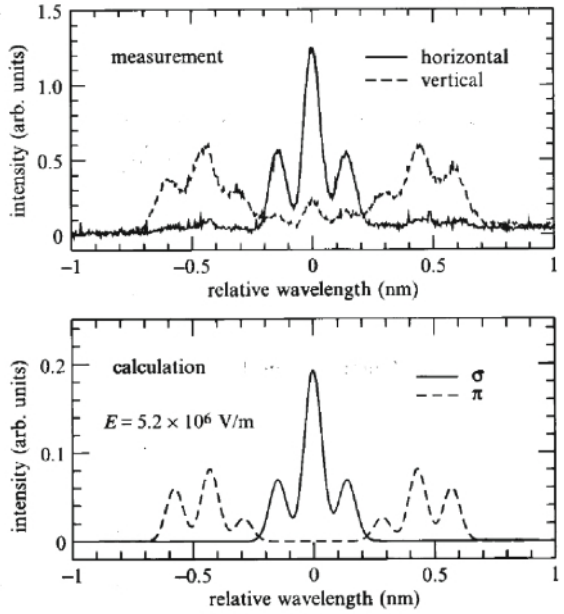

Figure 2.6: Stark effect of the Balmer α line of neutral hydrogen measured on Large Helical Device and a calculation results [10].

π ($\Delta M = 0$) and σ ($\Delta M = \pm 1$) components are linearly polarized along and perpendicular to the electric field, respectively. Unlike the Zeeman effect, the π component lie in the wings of spectral line, while σ component is near the line core (figure 2.6). In addition, we cannot observe circular polarization, because the Stark effect does not split $M = 1$ and $M = -1$. Thus, we cannot measure the line-of-sight component of electric field strength by using the Stark effect.

2.2.3 Resonance scattering

In the bound-bound absorption process, the electric field of the incident radiation induces an oscillating dipole moment in the scattering atoms on the plane perpendicular to the propagation direction of the incident radiation. Dipole radiation emitted from the

oscillating dipole moment does not have component along the propagation direction of the incident radiation. These processes are resonance scattering. If there are anisotropy of incident radiation field around the line of sight, the resonance scattering is linearly polarized.

In the quantum approach, the resonance scattering is one of the atomic polarization. Excitation by the incident radiation field with anisotropy distribution creates population imbalances among the magnetic sub-levels, because incident photon only excite magnetic sub-levels which have magnetic quantum number 1 plus or 1 minus magnetic quantum number of the lower level. In addition, rotation of the quantization axis produces the quantum interferences among them.

Let's consider $J = 0$ - 1 transition, where J is total angular momentum. Magnetic quantum number of lower level, M_l, is 0, and magnetic quantum numbers of upper level, M_u, are -1, 0, and 1. When unpolarized light incident on the atom along a quantization axis, only upper levels with $M_u = -1$ and 1 are excited, because unpolarized light can be understood to involve incoherent right-hand and left-hand circular polarizations. The excited atom is characterized as atomic alignment, and emitted radiation are observed in the form of broadband linear polarization.

The state of the atoms, density matrix, is obtained by solving statistical equilibrium equations, and emission coefficients are derived from the density matrix. The details of the equations is described in section 2.3. In the ideal case of the resonance scattering (the assumption of the two-levels atom, unpolarized lower level, no magnetic field, and no collision), emission coefficients in the four Stokes parameters ($i = 1, 2, 3, 4$) can be written in eq. (10.16) in Landi Degl'Innocenti & Landolfi [61],

$$\epsilon_i(\nu, \vec{\Omega}) = \frac{h\nu}{4\pi} N_l \, B(\alpha_l J_l \rightarrow \alpha_u J_u) \, \phi(\nu_0 - \nu) \sum_{KQ} W_K(J_l, J_u) \, (-1)^Q \, T^K_Q(i, \vec{\Omega}) \, J^K_{-Q}(\nu_0), \tag{2.67}$$

where N_l is the number density of the atoms in lower state, $B(\alpha_l J_l \rightarrow \alpha_u J_u)$ is the Einstein coefficient for radiative excitation, $\phi(\nu_0 - \nu)$ is the line profile function, $T^K_Q(i, \vec{\Omega})$ is spherical tensors for rotation (section 2.1.5), $J^K_Q(\nu_0)$ is spherical tensors for radiation field, and $W_K(J_l, J_u)$ is defined to be

$$W_K(J_l, J_u) \equiv \frac{\left\{ \begin{array}{ccc} 1 & 1 & K \\ J_u & J_u & J_l \end{array} \right\}^2}{\left\{ \begin{array}{ccc} 1 & 1 & 0 \\ J_u & J_u & J_l \end{array} \right\}^2}. \tag{2.68}$$

For an unpolarized incident beam, the polarization degree of the scattered radiation in optically thin case is given by

$$p_Q \equiv \frac{\epsilon_Q(\nu, \vec{\Omega})}{\epsilon_I(\nu, \vec{\Omega})} = \frac{3 \, W_2 \sin^2 \Theta}{4 - W_2 + 3 \, W_2 \cos^2 \Theta} \tag{2.69}$$

$$p_U \equiv \frac{\epsilon_U(\nu, \vec{\Omega})}{\epsilon_I(\nu, \vec{\Omega})} = 0, \tag{2.70}$$

where Θ is angle between incident light and scattered light. If $W_2 = 0$, $p_Q = 0$ and if $W_2 = 1$, $p_Q = 1$. Thus the factor W_2 can be regarded as an efficiency factor for the generation of the linear polarization from unpolarized light in resonance scattering process.

Spherical tensors for radiation field $J^K_Q(\nu_0)$ is generally defined as

$$J^0_0 = \int \mathrm{d}\nu \oint \phi(\nu_0 - \nu) \frac{\mathrm{d}\vec{\Omega}}{4\pi} I_{\nu\vec{\Omega}}, \tag{2.71}$$

$$J^1_0 = \int \mathrm{d}\nu \oint \phi(\nu_0 - \nu) \frac{\mathrm{d}\vec{\Omega}}{4\pi} \sqrt{\frac{3}{2}} \mu V_{\nu\vec{\Omega}}, \tag{2.72}$$

$$J^1_1 = -\int \mathrm{d}\nu \oint \phi(\nu_0 - \nu) \frac{\mathrm{d}\vec{\Omega}}{4\pi} e^{i\chi} \sqrt{\frac{3}{2}} \sqrt{1-\mu^2} V_{\nu\vec{\Omega}}, \tag{2.73}$$

$$J^2_0 = \int \mathrm{d}\nu \oint \phi(\nu_0 - \nu) \frac{\mathrm{d}\vec{\Omega}}{4\pi} \frac{1}{2\sqrt{2}} \Big[(3\mu^2 - 1) I_{\nu\vec{\Omega}} + 3(\mu^2 - 1) Q_{\nu\vec{\Omega}} \Big], \tag{2.74}$$

$$J^2_1 = \int \mathrm{d}\nu \oint \phi(\nu_0 - \nu) \frac{\mathrm{d}\vec{\Omega}}{4\pi} \frac{\sqrt{3}}{2} e^{i\chi} \sqrt{1-\mu^2} \Big[-\mu (I_{\nu\vec{\Omega}} + Q_{\nu\vec{\Omega}}) - i U_{\nu\vec{\Omega}} \Big], \tag{2.75}$$

$$J^2_2 = \int \mathrm{d}\nu \oint \phi(\nu_0 - \nu) \frac{\mathrm{d}\vec{\Omega}}{4\pi} \frac{\sqrt{3}}{2} e^{2i\chi} \sqrt{1-\mu^2} \Big[\frac{1}{2}(1-\mu^2) I_{\nu\vec{\Omega}} - \frac{1}{2}(1+\mu^2) Q_{\nu\vec{\Omega}} - i\mu U_{\nu\vec{\Omega}} \Big], \tag{2.76}$$

$$J^K_{-Q} = (-1)^Q [J^K_Q]^*, \tag{2.77}$$

where χ and θ are azimuthal and inclination angles of the orientation of each ray of direction $\vec{\Omega}$ with respect to axes which you give, respectively, where μ is defined as $\cos\theta$, and where * denotes complex conjugation. J^0_0 corresponds to the radiation mean intensity, whereas the others represent the anisotropy of the radiation field.

Let us consider simple atmospheric model 'un-magnetized Milne-Eddington atmosphere'. In the plane-parallel atmosphere, J^0_0 and J^2_0 are the nonvanishing components of the radiation tensor. The J^2_0 represents the difference of intensity between vertical rays and horizontal rays. Figure 2.7 shows the variation with optical depth τ of the anisotropy factor $A \equiv J^2_0/J^0_0$ for various values of b/a in the un-magnetized Milne-Eddington atmosphere, in which the source function is a function of $a + b\tau$. If the source function is constant ($b/a = 0$), the anisotropy A is zero in deeper layer, because the plasma is isotropically illuminated by radiation with constant intensity. In contrast, near the stellar surface incoming vertical rays become weak, and horizontal rays is stronger than vertical outgoing rays ($A < 0$). If b/a becomes large, the limb darkening makes the anisotropy A becomes positive.

Another simple atmospheric model is showed in figure 2.8 [12]. The illuminating radiation is unpolarized and contained within a cone of half aperture θ_M with the vertex centered at the scattering atom. We obtain by neglecting the center to limb variation

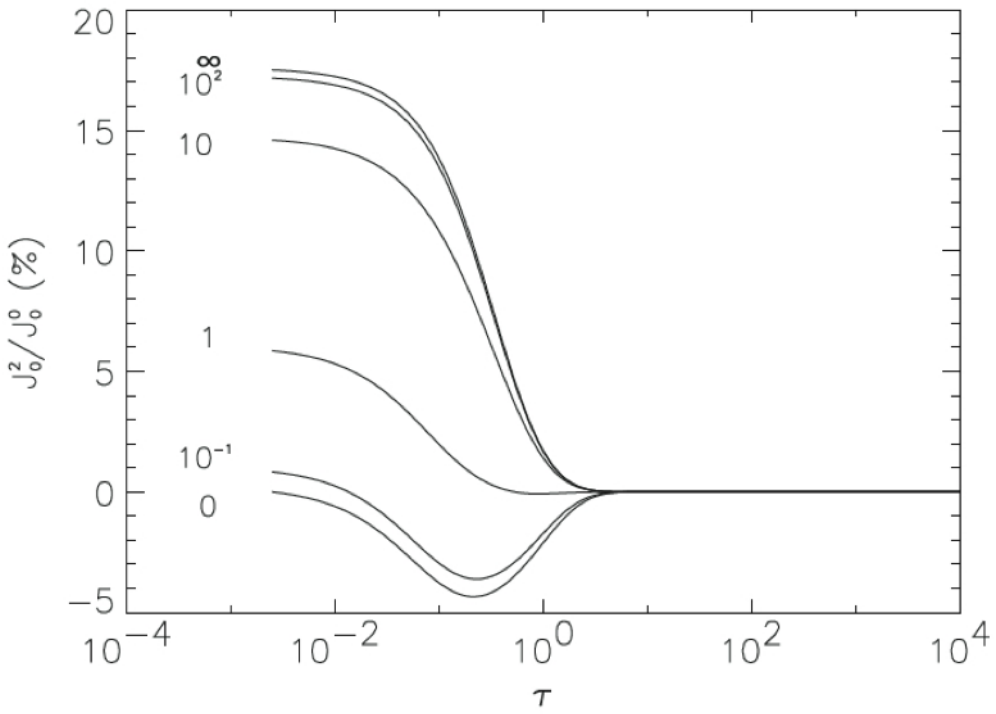

Figure 2.7: Variation of the anisotropy factor J^2_0/J^0_0 with optical depth τ in unmagnetized Milne-Eddington atmosphere for various values of b/a [11].

of the sun

$$J^0_0 = \frac{1}{2}(1-\cos\theta_M)\, I, \tag{2.78}$$

$$J^2_0 = \frac{1}{4\sqrt{2}}(1-\cos\theta_M)(1+\cos\theta_M)\cos\theta_M\, I, \tag{2.79}$$

$$\tag{2.80}$$

$$A = \frac{1}{2\sqrt{2}}(1+\cos\theta_M)\cos\theta_M, \tag{2.81}$$

$$\tag{2.82}$$

and the others are vanished. The θ_M determines the dilution and anisotropy of the incident radiation field.

Real solar atmosphere is more structured and dynamic than the simple atmospheric models. Figure 2.9 shows distribution of the anisotropy factor A in realistic model of a network region made by radiative magnetohydrodynamic simulation [77]. Even sign of the factor has complex distribution in the realistic model.

The generation of linear polarization by resonance scattering changes due to the change of energy configuration of the atom in the transition to the Paschen-Back regime [61, 78], when the spin-orbit interaction becomes negligible with respect to the magnetic interaction. Figure 2.10 shows degree of net linear polarization of the transition ${}^2S_{\frac{1}{2}}$ - ${}^2P_{\frac{1}{2},\frac{3}{2}}$ for the case of 90° scattering estimated by a code in López Ariste and

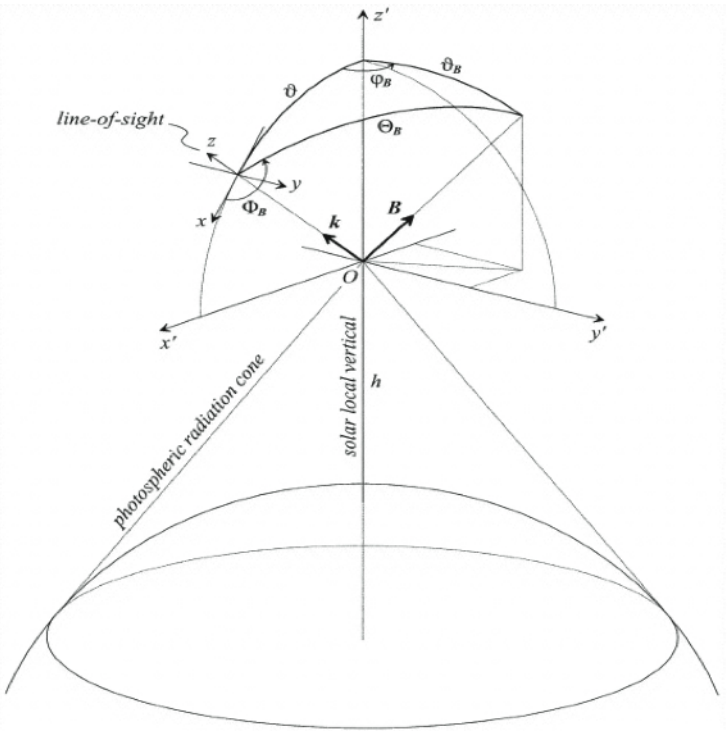

Figure 2.8: Geometric model for radiation scattering in the presence of a magnetic field. The cone of (photospheric) radiation irradiates the scattering atoms at the point O of height h above the solar surface.

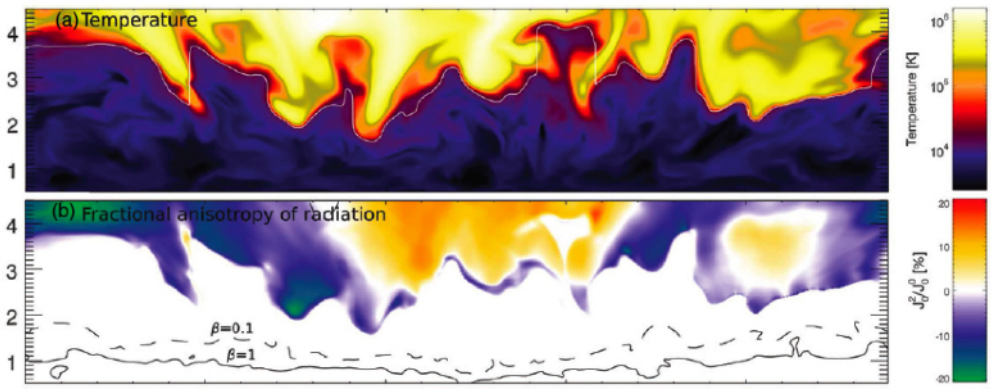

Figure 2.9: (a) Temperature and (b) anisotropy factor of the Lyα radiation field across the vertical 2D slice of 3D radiation magnetohydrodynamic simulations. The white lines in each plot indicates the height where the line-center optical depth is unity along a line of sight with $\mu = 0.3$.

Casini [12], and energy level shifts against magnetic field strength for ${}^2P_{\frac{1}{2}}$ and ${}^2P_{\frac{3}{2}}$. The magnetic field is along the normal to the solar surface. The incident radiation is not polarized, possesses cylindrical symmetry around the normal to the solar surface and perpendicular to the line of sight. Polarization degree derived from total angular momentum number by using eq. (2.69) is roughly consistent with the estimated one by using the code [12] for $B < 10^3$ G. Although Hanle effect (section 2.2.5) does not produce any modification of the polarization because of the field geometry (section **??**), the estimated polarization degree changes, as the orbital and spin angular momentum get better quantum number than the total angular momentum in incomplete Paschen-Back regime.

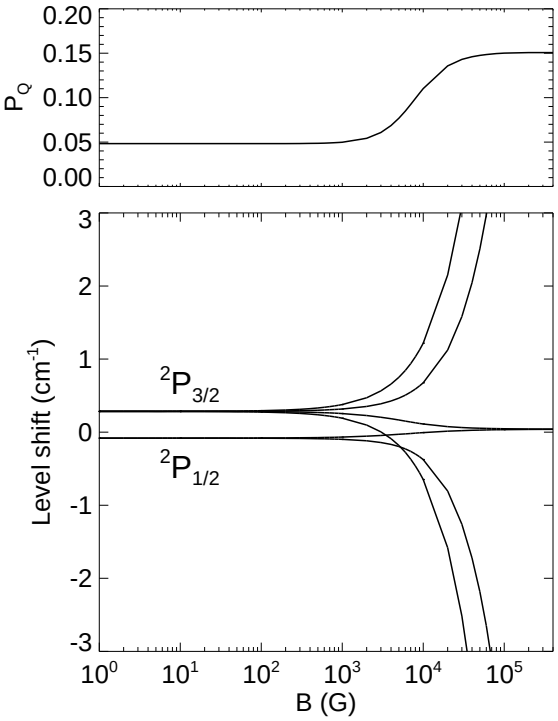

Figure 2.10: Top panel show net linear polarization degree for Stokes Q of the transition ${}^2S_{\frac{1}{2}}$ - ${}^2P_{\frac{1}{2},\frac{3}{2}}$ for the case of 90° scattering calculated by a code in López Ariste and Casini [12]. Bottom panel shows energy level shifts of ${}^2P_{\frac{1}{2}}$ and ${}^2P_{\frac{3}{2}}$. Both abscissas indicate strength of magnetic field around which the incident radiation field possesses cylindrical symmetry. Stokes Q is defined to be positive on the plane perpendicular to the magnetic field.

2.2.4 Impact polarization

Skinner [79] discovered linear polarization emitted from atoms collisionally excited by beams of electrons. The excited atom is characterized as atomic alignment of the angular momenta along the particle propagation direction. The state of the atoms,

density matrix, is obtained by solving statistical equilibrium equations, and emission coefficients are derived from the density matrix.

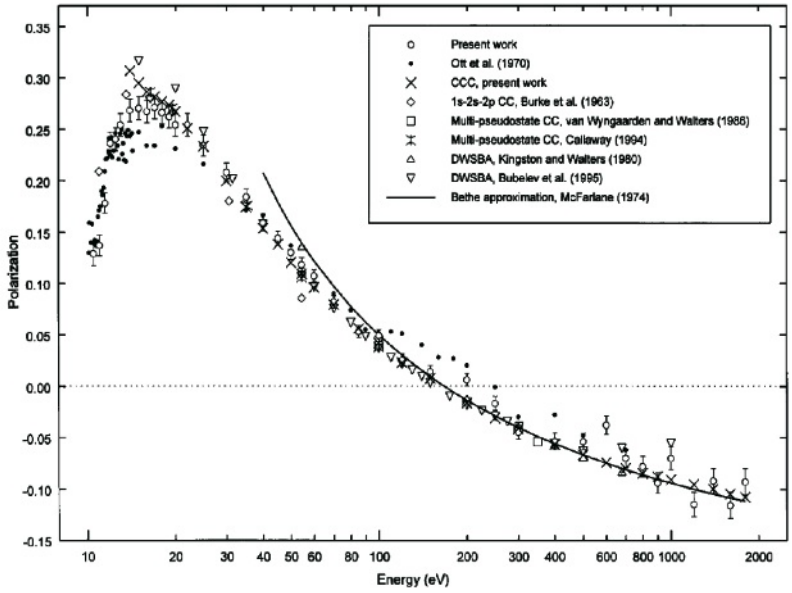

Figure 2.11: Experimental and theoretical values for the polarization of Lyman-α radiation from hydrogen excited by electron impact [13].

Here we describe qualitative characteristics of the impact polarization. The angular distribution of the Stokes I and Q of spectral line produced by the impact polarization by high-energy charged particle of velocity, v, are given by

$$I(v,\beta) \sim I_T \{1 - P(v)\cos^2\beta\} \tag{2.83}$$

$$Q(v,\beta) \sim I_T P(v)\sin^2\beta, \tag{2.84}$$

where β is angle between the direction of v and the line of sight, $P(v)$ is polarization degree in the case of $\beta = 90°$, and I_T is the mean intensity [80]. When the direction of the travel of high-energy charged particle is perpendicular to the line of sight, we observe maximum polarization degree, $P(v)$. Figure 2.11 shows observed and calculated values of $P(v)$ for the Hα line collisionally excited by electron beam [81]. It is noticeable that the sign of the polarization degree change for increasing the energy of the electron beam. The energy of the particle beam at which the sign of the polarization changes is $\sim$ 200 eV for electrons and is $\sim$ 200 keV for protons. In the solar plasma, since the energetic particles have a velocity distribution, we should consider the distribution function of the velocity.

2.2.5 Hanle effect

Hanle [82] interpreted a previously observed phenomena which show an effect of a weak magnetic field on the scattered radiation. Oscillating dipole moment excited by

incident radiation or by colliding particles precess around magnetic field. Since the oscillating moment is radiatively damped, the orbit of the precession depends on the ratio between the precession frequency (the Larmor angular frequency) $\omega_L = eB/2mc$ and the damping frequency (Einstein's spontaneous transition coefficient) γ. Observed polarization reflects the weighted average of the damping precession.

The ratio between ω_L and γ can be described

$$\Omega = \frac{2g\omega_L}{\gamma} \tag{2.85}$$

where g is the Landé factor of the excited level. The effective range of Ω in which the Hanle effect is sensitive to the magnetic field strength is approximately $0.2 < \Omega < 5$. The observed linear polarization rotates and depolarize. For a small magnetic field strength, the polarization behave like the resonance scattering (section 2.2.3). For a strong magnetic field, the Hanle depolarization and rotation saturate. Because line broadening due to the damping γ is generally less than the Doppler broadening in solar plasma, the Hanle effect occurs in a parameter range in which the Zeeman effect is practically ineffective.

When the magnetic field is parallel to the direction of incident radiation, the damping precession oscillates in the plane perpendicular to the incident radiation, the Hanle effect does not modify the resonance scattering polarization. Thus the Hanle effect does not work in numerical experiment of figure 2.10.

Tangled magnetic field isotropically distributed in the spatial resolution element is invisible in the Zeeman effect, because polarization is canceled out by contribution of field which points opposite or perpendicular directions. In contrast, the Hanle depolarization could be observable in the tangled field.

To understand quantitatively, we need to solve the equations of statistical equilibrium (section 2.3). Here, we introduce simple example of the precession by using two level atoms with $J_l = 0$, $J_u = 1$. Time variation of the density matrix is derived as solution of equation of motion

$$i\hbar \frac{\partial}{\partial t}\hat{\rho} = [\hat{H}, \hat{\rho}], \tag{2.86}$$

where Hamiltonian H consists of the perturbation due to the magnetic field. When quantization axis is parallel to the magnetic field, the Hamiltonian H in Zeeman regime is written as

$$\langle M| \hat{H} |M'\rangle = -\hbar\omega_L M \delta_{MM'}, \tag{2.87}$$

and

$$\hat{H} = -\hbar\omega_L \begin{pmatrix} 1 & 0 & 0 \\ 0 & 0 & 0 \\ 0 & 0 & -1 \end{pmatrix}. \tag{2.88}$$

Substituting eq. (2.88) into eq. (2.86) leads to

$$\hat{\rho}(t) = \begin{pmatrix} \rho_{1\,1}(0) & \rho_{1\,0}(0)e^{i\omega_L t} & \rho_{1\,-1}(0)e^{2i\omega_L t} \\ \rho_{0\,1}(0)e^{-i\omega_L t} & \rho_{0\,0}(0) & \rho_{0\,-1}(0)e^{i\omega_L t} \\ \rho_{-1\,1}(0)e^{-2i\omega_L t} & \rho_{-1\,0}(0)e^{-i\omega_L t} & \rho_{-1\,-1}(0) \end{pmatrix}. \tag{2.89}$$

Only off-diagonal element oscillate in time due to the magnetic field. Here we assume the initial value of each elements is determined by incident radiation.

When quantization axis is along the incident radiation, unpolarized lights with angular momentum of ± 1 excite the energy state with $M_u = \pm 1$, and the density matrix can be written as

$$\hat{\rho} = \frac{1}{2}\begin{pmatrix} 1 & 0 & 0 \\ 0 & 0 & 0 \\ 0 & 0 & 1 \end{pmatrix}. \tag{2.90}$$

There is population imbalance among the sublevels, but no coherence (no off-diagonal component of the density matrix) for the moment. Then, we rotate the quantization axis from the direction of the incident radiation to the magnetic field by using the rotation matrix (sec. 2.1.5). When the angle between the magnetic field and the incident radiation is θ, the density matrix of eq. (2.90) become

$$\hat{\rho}' = \frac{1}{4}\begin{pmatrix} 1+\cos^2\theta & -\sqrt{2}\cos\theta\sin\theta & 1-\cos^2\theta \\ -\sqrt{2}\cos\theta\sin\theta & 2\sin^2\theta & \sqrt{2}\cos\theta\sin\theta \\ 1-\cos^2\theta & \sqrt{2}\cos\theta\sin\theta & 1+\cos^2\theta \end{pmatrix}. \tag{2.91}$$

The angle θ which makes population of sublevels balance ($\rho'_{11} = \rho'_{00} = \rho'_{-1-1}$) is called van Vleck angle $\theta_{\rm vv}$. For example, if the magnetic field is perpendicular to the incident radiation, the time evolution of the density matrix is

$$\hat{\rho}'(t) = \frac{1}{4}\begin{pmatrix} 1 & 0 & e^{2i\omega_L t} \\ 0 & 2 & 0 \\ e^{-2i\omega_L t} & 0 & 1 \end{pmatrix}. \tag{2.92}$$

The oscillation of the coherence corresponds to the precession of the oscillator. If the magnetic field is along the incident radiation field, off-diagonal elements are not produced and the density matrix does not change in time.

From statistical equilibrium equations (section 2.3), we obtain the emissivity for a two-level atom with unpolarized lower level by neglecting stimulated emission, with helps eqs. (2.68) and (2.85) as

$$\epsilon_i(\vec{\Omega}) = k_L^A \oint \frac{{\rm d}\Omega'}{4\pi} \sum_{j=0}^{3} \sum_{KQ} W_K(J_l, J_u)(-1)^Q T_Q^K(i,\vec{\Omega}) T_{-Q}^K(j,\vec{\Omega}')\; e^{-i\alpha}\cos\alpha\; I_j(\nu_0,\vec{\Omega}'), \tag{2.93}$$

where

$$k_L^A = \frac{h\nu}{4\pi} N_l B(\alpha_l J_l \rightarrow \alpha_u J_u),$$

and where

$$\cos\alpha = \sqrt{\frac{1}{1+\pi^2\Omega^2 Q^2}},$$

where N_l is the number density of the atom in the lower level, $B(\alpha_l J_l \rightarrow \alpha_u J_u)$ is the Einstein coefficient for radiative excitation, and i and j are index of Stokes I, Q, U, and V. Stokes vectors $I_j(\nu_0, \vec{\Omega}')$ of incident ray are rotated and depolarized by the Hanle effect ($e^{-i\alpha}\cos\alpha$), and generate resonance scattering with the efficiency of $W_K(J_l, J_u)$. The spherical tensors for the rotation $T^K_{-Q}(j, \vec{\Omega}')$ and $T^K_Q(i, \vec{\Omega})$ rotate the quantization axis from the incident radiation axis to the magnetic field, and from the magnetic field to the line of sight, respectively.

In the saturated regime of the Hanle effect ($\Omega \gg 5$), if the incident radiation are unpolarized, the emissivities for Stokes Q and U are simply expressed by

$$\begin{array}{l} \epsilon_Q \sim w(3\cos^2\vartheta_B - 1)\sin^2\Theta_B \cos 2\Phi_B \\ \epsilon_U \sim w(3\cos^2\vartheta_B - 1)\sin^2\Theta_B \sin 2\Phi_B \end{array} , \tag{2.94}$$

where

$$w = \frac{9\sqrt{2}}{8}\frac{A\, W_2 \sin^2\Theta}{4 - W_2 + 3\, W_2 \cos^2\Theta},$$

and where ϑ_B, Θ_B and Φ_B are defined in figure 2.8 [83]. The factor $3\cos^2\vartheta_B - 1$ comes from the rotation of quantization axis from the incident radiation field into the magnetic field, and represents population unbalance among sub-levels, i.e. atomic alignment. We can confirm it in eq. (2.91) as $4(\rho_{11} - \rho_{00}) = 3\cos^2\theta - 1$. In Hanle saturation regime, the magnetic field completely decohere among the sub-levels where the quantization axis is along the magnetic field. When ϑ_B is equal to $\theta_{\rm vv}$, atomic polarization disappear.

Factors $\sin^2\Theta_B \cos 2\Phi_B$ and $\sin^2\Theta_B \sin 2\Phi_B$ come from the rotation of quantization axis from the magnetic field into the line of sight. A sign change of Stokes Q and U due to a 90° change of Φ_B can thus be compensated by a sign change of the factor $(3\cos^2\vartheta_B - 1)\sin^2\Theta_B$. This is the reason why there are 90° ambiguity in the full vector measurement of magnetic field with the Hanle effect.

Figure 2.12 shows the polarization degree for a two-level atom ($J_l = 0$, $J_u = 1$) in Hanle saturation regime. Polarization degree depends on the orientation of the magnetic field in expression of eq. (2.94). Figure 2.13, 2.14, and 2.15 show polarization degree as function of Ω, where the orientations of the magnetic field are given. For $1 < \Omega < 5$, the polarization rotate and is depolarized according to the magnetic field strength. When θ_B is equal to θ_{vv}, the polarization degree gets zero.

2.2.6 Alignment-to-orientation conversion

Lehmann [62] discovered circular polarization emitted from atoms excited by no-circular polarized light in magnetic field. In non external field case, pathways of excitation-decay processes are independent between distinct J and L levels. As external magnetic or electric fields become strong, the sublevels of distinct J or L levels get close. Then, when the distance in energy is less than the lifetime-broadened width of the states,

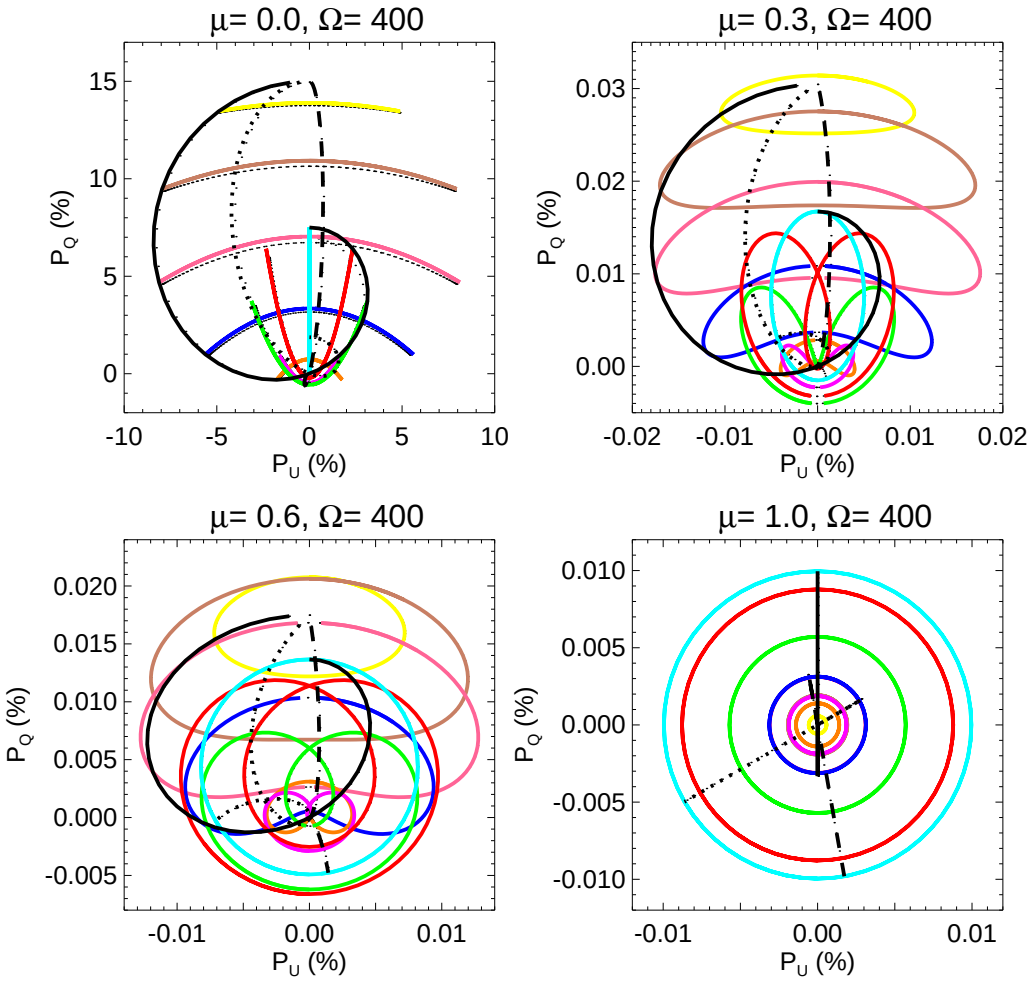

Figure 2.12: Polarization degree calculated by using eq. (2.94) in Hanle saturation regime ($\Omega = 400$) in four case of $\mu = \cos\vartheta = 0.0$, 0.3, 0.6, 1.0, where ϑ is angle between the normal of the solar surface and the line of sight. Black lines are results as function of θ_B. The azimuth angle of the magnetic field (ϕ_B) of solid, dotted, and dashed line are 90°, 30°, and −5°, respectively. Colored lines are results for different ϕ_B: Pair of color and ϕ_B are (yellow, 10°), (brown, 20°), (pink, 30°), (blue, 40°), (orange, 50°), (purple, 60°), (green, 70°), (red, 80°), and (light blue, 90°).

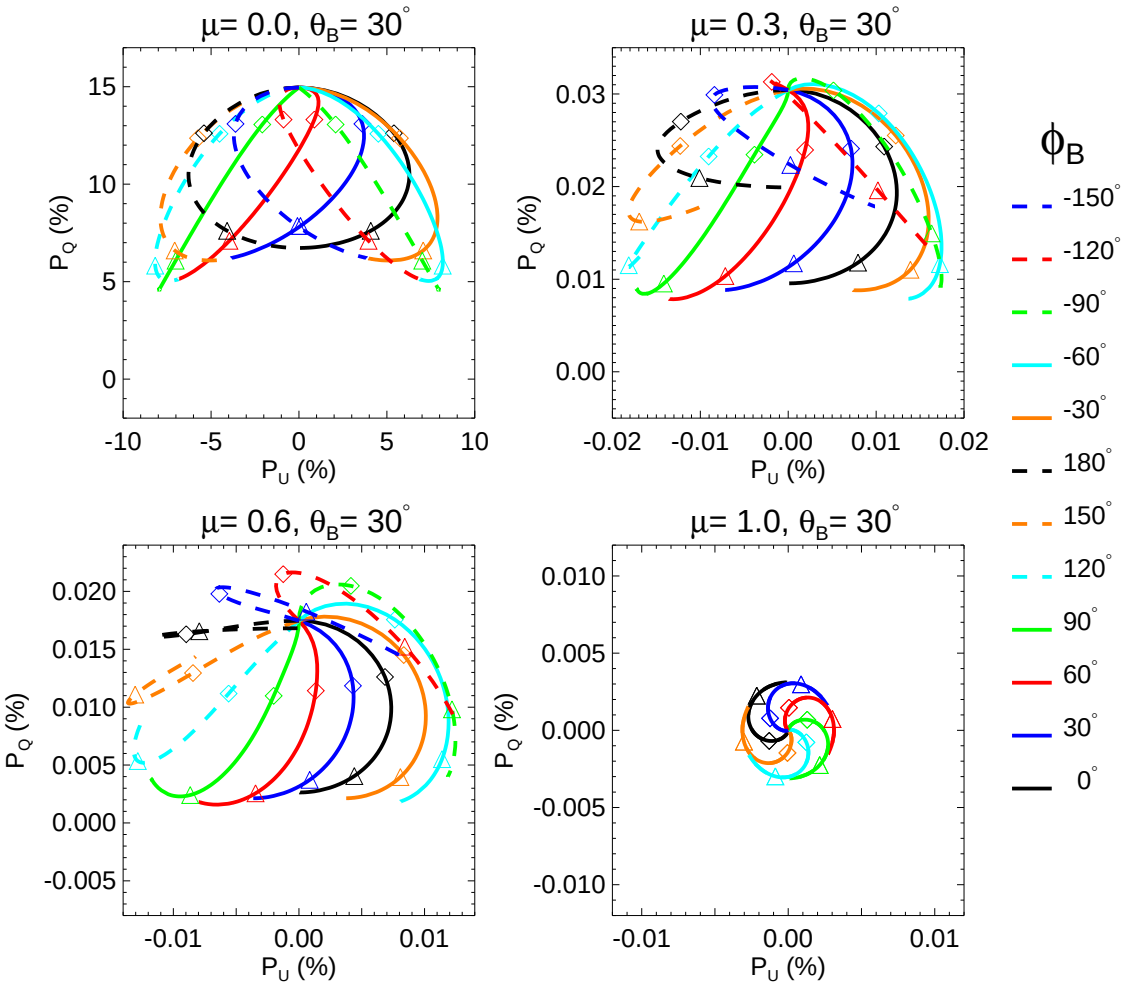

Figure 2.13: Polarization degree for a two-level atom ($J_l = 0$, $J_u = 1$) calculated by using a code in López Ariste and Casini [12] as function of Ω in the case of $\theta_B = 30°$. Symbols of diamond and triangle show results with $\Omega = 1$ and 5, respectively.

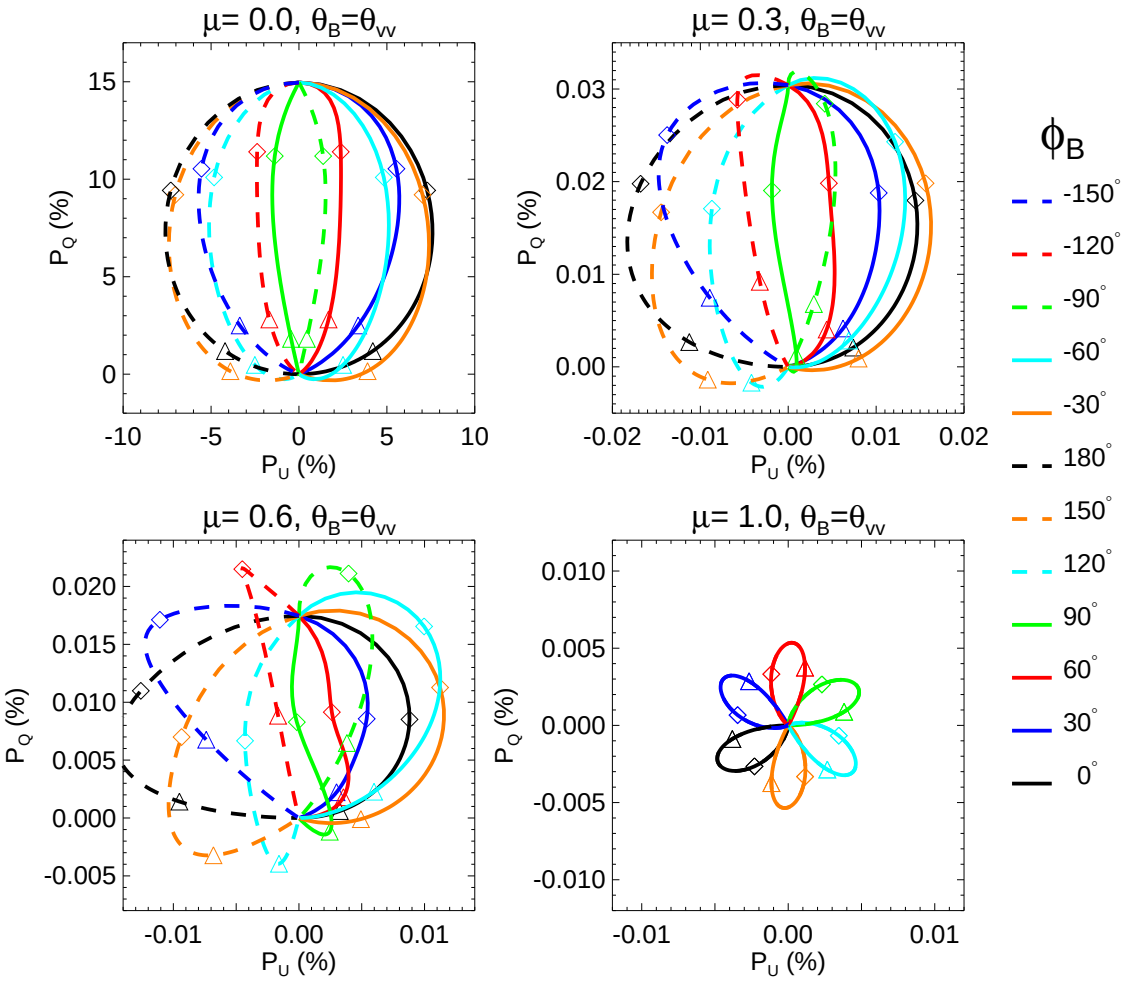

Figure 2.14: Polarization degree in the case of $\theta_B = \theta_{\mathrm{VV}}$. The others are the same as in figure 2.13.

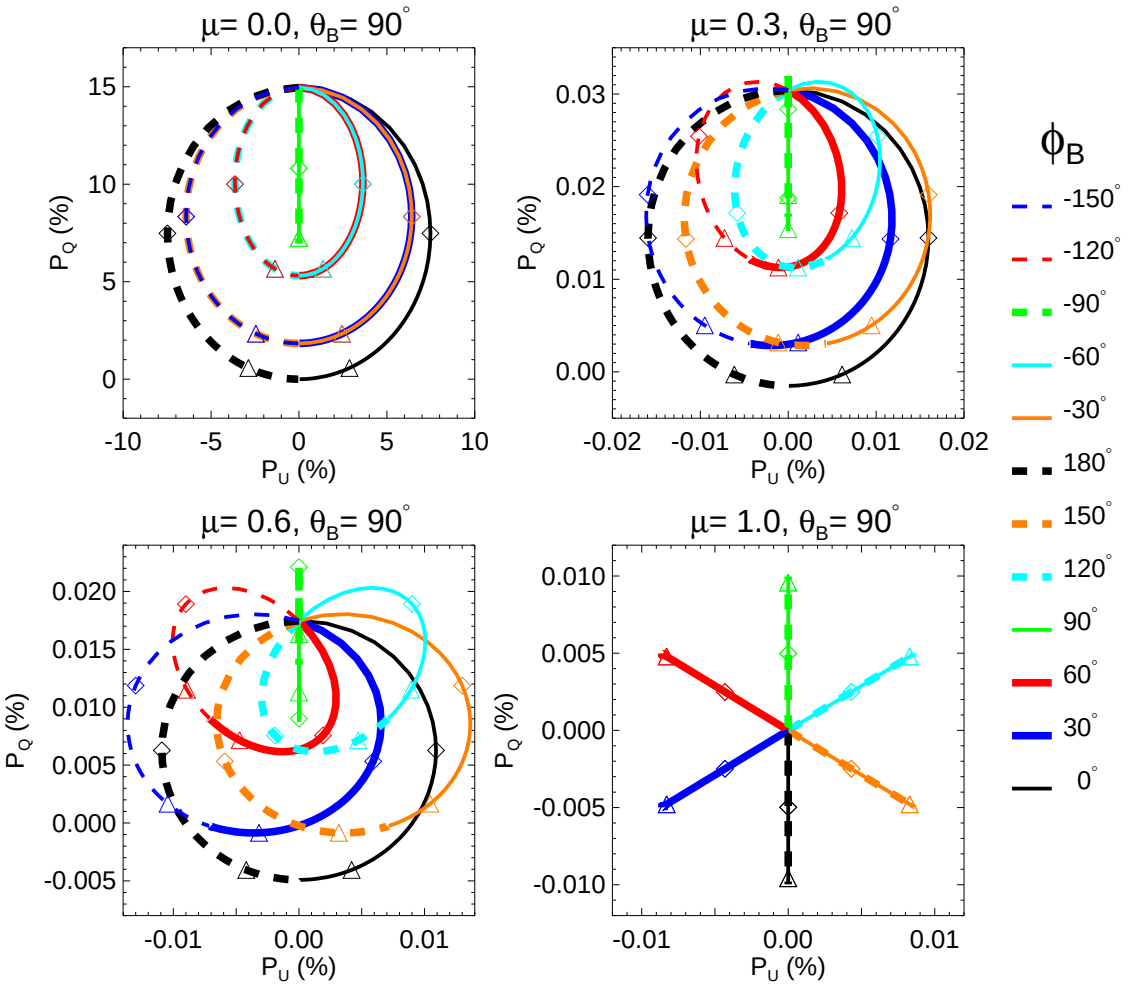

Figure 2.15: Polarization degree in the case of $\theta_B = 90°$. The others are the same as in figure 2.13.

interference between the states can occur. The interference of different excitation-decay pathways results the conversion between alignment and orientation. Alignment-to-orientation conversion occur in the solar plasma, because anisotropy of the excitation process generally causes atomic alignment in the sun.

To understand quantitatively, we should solve the equations of statistical equilibrium. In section 2.3, we introduce the equations of statistical equilibrium. Here, we focus only on the contribution of the magnetic field to the Alignment-to-orientation conversion in the statistical equilibrium equations. Time variation of the density matrix by magnetic-field effect in the spherical tensor representation is written as

$$\begin{aligned}
\frac{\mathrm{d}}{\mathrm{d}t}\,{}^{nS}\rho^K_Q(LJ,L'J') &= -i\,{}^{nS}\rho^{K'}_{Q'}(L''J'',L'''J''')\Bigg[\delta_{JJ''}\delta_{J'J'''}\delta_{KK'}\delta_{QQ'}\omega_{JJ'} \\
&\quad +\delta_{QQ'}\frac{e_0B}{2m}(-1)^{J+J'-Q}\sqrt{(2K+1)(2K'+1)}\begin{pmatrix} K & K' & 1 \\ -Q & Q & 0\end{pmatrix} \\
&\quad \times\Big[\delta_{J'J'''}\Gamma_{LS}(J,J'')\begin{Bmatrix} K & K' & 1 \\ J'' & J & J'\end{Bmatrix} \\
&\quad +\delta_{JJ''}(-1)^{K+K'}\Gamma_{LS}(J''',J')\begin{Bmatrix} K & K' & 1 \\ J''' & J' & J\end{Bmatrix}\Big]\Bigg], \qquad (2.95)
\end{aligned}$$

where

$$\begin{aligned}
\Gamma_{LS}(J,J') &= \delta_{JJ'}\sqrt{(2J+1)J(J+1)} \\
&\quad -(-1)^{L+S+J}\sqrt{(2J+1)(2J'+1)(2S+1)(S+1)S}\begin{Bmatrix} J & J' & 1 \\ S & S & L\end{Bmatrix}.
\end{aligned}$$

The K of 0, 1, and 2 indicate the degree of the atomic population, orientation, and alignment, respectively. In the case of $J = J'$, there are no conversion between K and K', because the right side of the eq. (2.95) reduces to the term $ig\omega_L Q$. In weak field regime, in which the time variation of the quantum interference between distinct J levels (${}^{nS}\rho^K_Q(LJ,L'J'),\ J \neq J'$) is almost determined by a factor of $\delta_{KK'}\omega_{JJ'}$, there are no conversion between K and K'. When the energy splitting between J and J' levels induced atomic level crossing in strong field regime, the magnetic-field effect is significant for the time variation of the quantum interference, and it is possible to occur conversion between K and K', i.e, conversion between atomic alignment and atomic orientation.

2.3 Calculation of polarization in spectral lines

Polarization of the spectral line is described by density matrix. In this section, we refer to Landi Degl'Innocenti and Landolfi [61], Goto [10], and Casini [14].

2.3.1 Energy of level

Wavelengths of possible line components are calculated from level energies of the initial and final terms of the transition. The level energies of the resolved magnetic sub-levels are solved from the eigenvalue problem of the Hamiltonian. In section 2.2.1 and 2.2.2, we gave elements of the Hamiltonian

$$\begin{aligned}\langle nLSJM|\, H\, |nL'SJ'M'\rangle &= \delta_{LL'}\delta_{JJ'}\delta_{MM'}\hbar\omega_{LJ}^{nS} \\ &\quad +\delta_{LL'}\delta_{MM'}\mu_0 B\Bigg[\delta_{JJ'}M \\ &\quad +(-1)^{L+S+J+J'+M}\sqrt{(2J+1)(2J'+1)(2S+1)S(S+1)} \\ &\quad \times\begin{pmatrix} J & J' & 1 \\ -M & M & 0\end{pmatrix}\begin{Bmatrix} J & J' & 1 \\ S & S & L\end{Bmatrix}\Bigg] \\ &\quad +a_0 e_0 E(-1)^{S-M'}\Lambda(nL,nL')\sqrt{(2J+1)(2J'+1)}\begin{Bmatrix} L & L' & 1 \\ J' & J & S\end{Bmatrix} \\ &\quad \times\sum_Q\begin{pmatrix} J & J' & 1 \\ M & M' & -Q\end{pmatrix}(e_E)_Q, \end{aligned} \tag{2.96}$$

where $\hbar\omega_{LJ}^{nS}$ are intrinsic energies of J levels, and where $(e_E)_Q$, for $Q = 0, \pm 1$, are the spherical components of the unit vector of the electric field. We employ the $|nLSJM\rangle$ scheme as the base wave-functions. The diagonalization of H is given as

$$H\begin{pmatrix} C_1^1 & C_1^2 & \dots & C_1^m \\ C_2^1 & C_2^2 & \dots & C_2^m \\ \vdots & \vdots & \ddots & \vdots \\ C_m^1 & C_m^2 & \dots & C_m^m\end{pmatrix} = \begin{pmatrix} C_1^1 & C_1^2 & \dots & C_1^m \\ C_2^1 & C_2^2 & \dots & C_2^m \\ \vdots & \vdots & \ddots & \vdots \\ C_m^1 & C_m^2 & \dots & C_m^m\end{pmatrix}\begin{pmatrix} E_{\psi_1} & 0 & \dots & 0 \\ 0 & E_{\psi_2} & \dots & 0 \\ \vdots & \vdots & \ddots & \vdots \\ 0 & 0 & \dots & E_{\psi_m}\end{pmatrix}. \tag{2.97}$$

Eigenvalues E_{ψ_i} are perturbed level energies. States of the perturbed level $|\psi_i\rangle$ are eigenfunctions, and they are expressed as a linear combination of several base functions

$$|\psi_i\rangle = \sum_j C_j^i\,|nLSJM\rangle = \sum_{(LJM)} C_{LJM}^i(nS)\,|nLSJM\rangle \tag{2.98}$$

2.3.2 Statistical equilibrium

The expectation value of observable O is

$$O(t) = \mathrm{Tr}\{\hat{O}\rho\}. \tag{2.99}$$

The time evolution of O can be obtained from eq. (2.99) as

$$\frac{\mathrm{d}}{\mathrm{d}t}O(t) = \mathrm{Tr}\Big\{\frac{\mathrm{d}\hat{O}}{\mathrm{d}t}\rho\Big\} + \mathrm{Tr}\Big\{\hat{O}\frac{\mathrm{d}\rho}{\mathrm{d}t}\Big\}. \tag{2.100}$$

Interaction picture is useful to represent system in which the total Hamiltonian H can be expressed as the sum of unperturbed Hamiltonian H_0 and interaction Hamiltonian

V. The *Interaction picture* is obtained from the *Schrödinger picture* by the following transformation

a) for the state vectors:

$$|\psi(t)\rangle_{\mathrm{I}} = e^{i\frac{2\pi}{h}H_0 t}\,|\psi(t)\rangle\,, \tag{2.101}$$

b) for the operators:

$$\hat{O}_{\mathrm{I}}(t) = e^{i\frac{2\pi}{h}H_0 t}\hat{O}(t)e^{-i\frac{2\pi}{h}H_0 t}, \tag{2.102}$$

c) for the interaction Hamiltonian:

$$V_{\mathrm{I}}(t) = e^{i\frac{2\pi}{h}H_0 t}Ve^{-i\frac{2\pi}{h}H_0 t}, \tag{2.103}$$

where I is symbol for the *interaction picture*. The equation of motion for density operator in the interaction picture is

$$\frac{\mathrm{d}}{\mathrm{d}t}\rho_{\mathrm{I}}(t) = -\frac{2\pi i}{h}[V_{\mathrm{I}}(t), \rho_{\mathrm{I}}(t)], \tag{2.104}$$

and integration of the eq. (2.104) between 0 and t gives

$$\rho_{\mathrm{I}}(t) = \rho_{\mathrm{I}}(0) - \frac{2\pi i}{h}\int_0^t [V_{\mathrm{I}}(t'), \rho_{\mathrm{I}}(t')]\mathrm{d}t'. \tag{2.105}$$

Substitution of eq. (2.104) into eq. (2.100) leads to

$$\frac{\mathrm{d}}{\mathrm{d}t}O(t) = \mathrm{Tr}\Big\{\Big(\frac{\mathrm{d}}{\mathrm{d}t}\hat{O}_{\mathrm{I}}(t)\Big)\rho_{\mathrm{I}}\Big\} - \frac{2\pi i}{h}\mathrm{Tr}\Big\{[\hat{O}_{\mathrm{I}}(t), V_{\mathrm{I}}(t)]\rho_{\mathrm{I}}(t)\Big\}. \tag{2.106}$$

The interaction picture reduces Hamiltonian to interaction Hamiltonian from eq. (2.100). We apply the interaction Hamiltonian to describe the interaction between a material system and the radiation field.

The expectation value of an operator given by $\hat{O} = |m'\rangle\langle m|$ in Schrödinger picture is the density matrix element $\rho_{mm'}(t)$, where $|m'\rangle$ and $|m\rangle$ are two arbitrary eigenvectors of H_0 in the Schrödinger picture. In this case, the left side of the equation (2.106) is the time evolution of density matrix element.

The first term of the right side of the equation (2.106) is written as

$$\begin{aligned}
\mathrm{Tr}\Big\{\Big(\frac{\mathrm{d}}{\mathrm{d}t}\hat{O}_{\mathrm{I}}(t)\Big)\rho_{\mathrm{I}}\Big\} &= \mathrm{Tr}\Big\{\Big(\frac{\mathrm{d}}{\mathrm{d}t}e^{i\frac{2\pi}{h}H_0 t}\,|m'\rangle\langle m|\,e^{-i\frac{2\pi}{h}H_0 t}\Big)\rho_{\mathrm{I}}\Big\} && (2.107)\\
&= \mathrm{Tr}\Big\{\Big(\frac{\mathrm{d}}{\mathrm{d}t}\,|m'\rangle\langle m|\,e^{2\pi i\nu_{m'm}t}\Big)\rho_{\mathrm{I}}\Big\} && (2.108)\\
&= 2\pi i\nu_{m'm}\mathrm{Tr}\Big\{|m'\rangle\langle m|\,e^{2\pi i\nu_{m'm}t}\rho_{\mathrm{I}}\Big\} && (2.109)\\
&= 2\pi i\nu_{m'm}\rho_{mm'}(t). && (2.110)
\end{aligned}$$

If we neglect the second terms, eq. (2.106) gives an analytical solution as

$$\rho_{mm'}(t) = \rho_{mm'}(0)e^{2\pi i\nu_{m'm}t}. \tag{2.111}$$

The above equation means that the value of the off-diagonal elements of the density matrix (i.e. interference of the states) oscillates in the frequency of $2\pi\nu_{m'm}$. When the

time scale of life time of the states (τ_A) is much less than that of the oscillation of the interference (τ_C), the off-diagonal elements of the density matrix is almost constant, and the states are coherent. For $\tau_A \gg \tau_C$, the off-diagonal elements of the density matrix modulates rapidly, and the states are incoherent. For $\tau_A \sim \tau_C$, the off-diagonal elements of the density matrix is sensitive to the energy difference between the states. The relation between τ_A and τ_C is essence of the Hanle effect (section 2.2.5).

The interaction Hamiltonian V in the non-relativistic approximation is deduced by Cohen-Tannoudji et al. [84, 85] which use the standard methods of Quantum Electrodynamics. At optical wavelength, V is approximately written as

$$V \sim \frac{e_0}{mc} \sum_i \vec{p}_i \cdot \vec{A}(\vec{r}_i), \tag{2.112}$$

where $\vec{r}_i$ and $\vec{p}_i$ are the position and momentum operator of the i-th optical electron of the atom, respectively, and where $\vec{A}(\vec{r}_i)$ is the operators corresponding to the vector potential of the radiation field.

The vector potential of the radiation field in terms of destruction $a(\nu, \vec{\Omega}, \lambda)$ and creation $a^\dagger(\nu, \vec{\Omega}, \lambda)$ operators of the harmonic oscillator can be written as

$$\vec{A}(\vec{r}_i) = \sum_{\nu\vec{\Omega}\lambda} c\sqrt{\frac{h}{2\pi\nu\mathcal{V}}}, \Big\{ a(\nu, \vec{\Omega}, \lambda)\vec{e}_\lambda(\vec{\Omega}) e^{i\vec{k}\cdot\vec{r}} + a^\dagger(\nu, \vec{\Omega}, \lambda)\vec{e}_\lambda(\vec{\Omega})^* e^{-i\vec{k}\cdot\vec{r}} \Big\}, \tag{2.113}$$

where

$$\vec{k} = \frac{2\pi\nu}{c}\vec{\Omega}$$

$$\vec{e}_\lambda(\vec{\Omega}) \cdot \vec{\Omega} = 0, \qquad \vec{e}_\lambda(\vec{\Omega}) \cdot \vec{e}_{\lambda'}(\vec{\Omega})^* = \delta_{\lambda\lambda'} \qquad (\lambda, \lambda' = 1, 2)$$

and

$$[a(\nu, \vec{\Omega}, \lambda), a(\nu', \vec{\Omega}', \lambda')] = [a^\dagger(\nu, \vec{\Omega}, \lambda), a^\dagger(\nu', \vec{\Omega}', \lambda')] = 0$$

$$[a(\nu, \vec{\Omega}, \lambda), a^\dagger(\nu', \vec{\Omega}', \lambda')] = \delta_{\nu\nu'}\delta_{\vec{\Omega}\vec{\Omega}'}\delta_{\lambda\lambda'},$$

and where the symbols $*$ and $\dagger$ indicate complex conjugate and Hermite conjugate, respectively. By using eq. (2.103), eq. (2.112) and eq. (2.113), we obtained

$$V_{\rm I}(t) = B(t) + B^\dagger(t), \tag{2.114}$$

where

$$B(t) = \sum_{\nu\vec{\Omega}\lambda} \Big\{ e^{i\frac{2\pi}{h}H_0 t} \frac{e_0}{m} \sqrt{\frac{h}{2\pi\nu\mathcal{V}}} (\sum_i \vec{p}_i \cdot \vec{e}_\lambda(\vec{\Omega}) e^{i\vec{k}\cdot\vec{r}}) e^{-i\frac{2\pi}{h}H_0 t} \Big\} \Big\{ e^{i\frac{2\pi}{h}H_0 t} a(\nu, \vec{\Omega}, \lambda) e^{-i\frac{2\pi}{h}H_0 t} \Big\}.$$

Substituting eq. (2.114) and eq. (2.105) into the second term of the right side of the eq. (2.106) leads to

$$-\frac{2\pi i}{h}{\rm Tr}\Big\{ [\hat{O}_{\rm I}(t), V_{\rm I}(t)]\rho_{\rm I}(t) \Big\} = \; - \; \frac{2\pi i}{h}{\rm Tr}\Big\{ [\hat{O}_{\rm I}(t), B(t)]\rho_{\rm I}(0) \Big\}$$

$$
\begin{aligned}
&- \frac{2\pi i}{h}\mathrm{Tr}\Big\{[\hat{O}_{\mathrm{I}}(t), B^{\dagger}(t)]\rho_{\mathrm{I}}(0)\Big\} \\
&- \frac{4\pi^2}{h^2}\mathrm{Tr}\Big\{\int_0^t \Big[[\hat{O}_{\mathrm{I}}(t), B(t)], B(t')\Big]\rho_{\mathrm{I}}(t')\mathrm{d}t'\Big\} \\
&- \frac{4\pi^2}{h^2}\mathrm{Tr}\Big\{\int_0^t \Big[[\hat{O}_{\mathrm{I}}(t), B(t)], B^{\dagger}(t')\Big]\rho_{\mathrm{I}}(t')\mathrm{d}t'\Big\} \\
&- \frac{4\pi^2}{h^2}\mathrm{Tr}\Big\{\int_0^t \Big[[\hat{O}_{\mathrm{I}}(t), B^{\dagger}(t)], B(t')\Big]\rho_{\mathrm{I}}(t')\mathrm{d}t'\Big\} \\
&- \frac{4\pi^2}{h^2}\mathrm{Tr}\Big\{\int_0^t \Big[[\hat{O}_{\mathrm{I}}(t), B^{\dagger}(t)], B^{\dagger}(t')\Big]\rho_{\mathrm{I}}(t')\mathrm{d}t'\Big\}
\end{aligned}
\tag{2.115}
$$

We are going to use some assumptions. First, the radiation field and the atomic system are supposed to be uncorrelated. In calculation, it means

$$
\rho_{\mathrm{I}}(t) = \rho_{\mathrm{I}}^{(R)}(t) \otimes \rho_{\mathrm{I}}^{(A)}(t) \quad (\text{for } t \geq 0) \tag{2.116}
$$

$$
\mathrm{Tr}\Big\{\hat{O}_{\mathrm{I}}^{(R)}\hat{O}_{\mathrm{I}}^{(A)}\rho_{\mathrm{I}}\Big\} = \mathrm{Tr}^{(R)}\Big\{\hat{O}_{\mathrm{I}}^{(R)}\rho_{\mathrm{I}}^{(R)}\Big\}\mathrm{Tr}^{(A)}\Big\{\hat{O}_{\mathrm{I}}^{(A)}\rho_{\mathrm{I}}^{(A)}\Big\},
$$

where $\mathrm{Tr}^{(R)}$ and $\mathrm{Tr}^{(A)}$ denote tracing over the states of the radiation field and of the atomic system, respectively. Second, the properties of the radiation fields can be expressed by a set of conditions

$$
\mathrm{Tr}^{(\mathrm{R})} \quad \Big\{a(\nu, \vec{\Omega}, \lambda)\rho_{\mathrm{I}}^{(\mathrm{R})}(t)\Big\} = \mathrm{Tr}^{(\mathrm{R})}\Big\{a^{\dagger}(\nu, \vec{\Omega}, \lambda)\rho_{\mathrm{I}}^{(\mathrm{R})}(t)\Big\} = 0 \tag{2.117}
$$

$$
\mathrm{Tr}^{(\mathrm{R})} \quad \Big\{a(\nu, \vec{\Omega}, \lambda)a(\nu', \vec{\Omega}', \lambda')\rho_{\mathrm{I}}^{(\mathrm{R})}(t)\Big\} = 0 \tag{2.118}
$$

$$
\mathrm{Tr}^{(\mathrm{R})} \quad \Big\{a^{\dagger}(\nu, \vec{\Omega}, \lambda)a^{\dagger}(\nu', \vec{\Omega}', \lambda')\rho_{\mathrm{I}}^{(\mathrm{R})}(t)\Big\} = 0 \tag{2.119}
$$

$$
\mathrm{Tr}^{(\mathrm{R})} \quad \Big\{a^{\dagger}(\nu, \vec{\Omega}, \lambda)a(\nu', \vec{\Omega}', \lambda')\rho_{\mathrm{I}}^{(\mathrm{R})}(t)\Big\} = 0 \quad \text{unless } \nu = \nu',\ \vec{\Omega} = \vec{\Omega}'. \tag{2.120}
$$

By using these assumptions, eq. (2.115) reduces to

$$
\begin{aligned}
-\frac{2\pi i}{h}\mathrm{Tr}\Big\{[\hat{O}_{\mathrm{I}}(t), V_{\mathrm{I}}(t)]\rho_{\mathrm{I}}(t)\Big\} &= -\frac{4\pi^2}{h^2}\mathrm{Tr}\Big\{\int_0^t \Big[[\hat{O}_{\mathrm{I}}(t), B(t)], B^{\dagger}(t')\Big]\rho_{\mathrm{I}}(t')\mathrm{d}t'\Big\} \\
&\quad -\frac{4\pi^2}{h^2}\mathrm{Tr}\Big\{\int_0^t \Big[[\hat{O}_{\mathrm{I}}(t), B^{\dagger}(t)], B(t')\Big]\rho_{\mathrm{I}}(t')\mathrm{d}t'\Big\} \\
&= -\sum_{\nu\vec{\Omega}\lambda\lambda'} \frac{8\pi^3\nu}{h\mathcal{V}} \sum_{nm''} [\vec{d}\cdot\vec{e}_{\lambda}(\vec{\Omega})]_{mn}[\vec{d}\cdot\vec{e}_{\lambda'}(\vec{\Omega})^*]_{nm''} \\
&\quad \times \int_0^t \Big[e^{2\pi i(\nu_{m'n}-\nu)(t-t')}\mathrm{Tr}^{(\mathrm{A})}\Big\{|m'\rangle\langle m''|\, e^{2\pi i\nu_{m'm''}t'}\rho_{\mathrm{I}}^{\mathrm{A}}(t')\Big\} \\
&\quad \mathrm{Tr}^{(\mathrm{R})}\Big\{\Big(a^{\dagger}(\nu, \vec{\Omega}, \lambda')a(\nu, \vec{\Omega}, \lambda) + \delta_{\lambda\lambda'}\Big)\rho_{\mathrm{I}}^{\mathrm{R}}(t')\Big\}\Big]\mathrm{d}t' \\
&\quad +\text{other terms} \\
&= -\sum_{\nu\vec{\Omega}\lambda\lambda'} \frac{8\pi^3\nu}{h\mathcal{V}} \sum_{nm''} [\vec{d}\cdot\vec{e}_{\lambda}(\vec{\Omega})]_{mn}[\vec{d}\cdot\vec{e}_{\lambda'}(\vec{\Omega})^*]_{nm''} \\
&\quad \times \int_0^t \Big[e^{2\pi i(\nu_{m'n}-\nu)(t-t')}\rho_{m''m'}(t')\Big(\frac{c^2}{h\nu^3}[I_{\lambda'\lambda}(\nu, \vec{\Omega})]_{t'} + \delta_{\lambda'\lambda}\Big)\Big]\mathrm{d}t' \\
&\quad +\text{other terms.}
\end{aligned}
\tag{2.121}
$$

Moreover we assume that the relaxation times charactering the evolution of the physical quantities of the coupled system is much longer than the typical time scale over the oscillating factor $e^{2\pi i(\nu_{m'n}-\nu)(t-t')}$. Under the assumptions, the second term of the right side of the eq. (2.106) is

$$\begin{aligned}
-\frac{2\pi i}{h}\mathrm{Tr}\Big\{[\hat{O}_{\mathrm{I}}(t),V_{\mathrm{I}}(t)]\rho_{\mathrm{I}}(t)\Big\} &= -\frac{16\pi^4}{h^2c}\sum_{\lambda\lambda'}\sum_{nm''}\rho_{m''m'}\oint\frac{\mathrm{d}\Omega}{4\pi} \\
&\quad\times\int_0^\infty \mathrm{d}\nu[\vec{d}\cdot\vec{e}_\lambda(\vec{\Omega})]_{mn}[\vec{d}\cdot\vec{e}_{\lambda'}(\vec{\Omega})^*]_{nm''} \\
&\quad\times\Big[I_{\lambda'\lambda}(\nu,\vec{\Omega})+\frac{h\nu^3}{c^2}\delta_{\lambda\lambda'}\Big]\Phi(\nu_{m'n}-\nu) \\
&\quad+\text{other terms} \\
&= -\frac{16\pi^4}{h^2c}\sum_{\lambda\lambda'}\sum_{nm''}\rho_{m''m'}\oint\frac{\mathrm{d}\Omega}{4\pi} \\
&\quad\times\int_0^\infty \mathrm{d}\nu[\vec{d}\cdot\vec{e}_\lambda(\vec{\Omega})]_{mn}[\vec{d}\cdot\vec{e}_{\lambda'}(\vec{\Omega})^*]_{nm''}I_{\lambda'\lambda}(\nu_{\bar{m}\bar{n}},\vec{\Omega}) \\
&\quad-\frac{16\pi^4}{hc^3}\sum_{\lambda}\sum_{m''}\rho_{m''m'}\sum_{n}\nu^3_{\bar{m}\bar{n}}\Theta(\nu_{\bar{m}\bar{n}}) \\
&\quad\times\oint\frac{\mathrm{d}\Omega}{4\pi}[\vec{d}\cdot\vec{e}_\lambda(\vec{\Omega})]_{mn}[\vec{d}\cdot\vec{e}_\lambda(\vec{\Omega})^*]_{nm''} \\
&\quad+\text{other terms},
\end{aligned} \tag{2.122}$$

where $\Theta(x)$ is a step function, which is equal 1 for positive value of the argument and to 0 otherwise. The evaluation of 'other terms' can be derived by similar calculation for those developed above.

The time evolution of the density matrix in the spherical tensor representation is written by using eq. (2.106), eq. (2.110), and eq. (2.122) as

$$\begin{aligned}
\frac{\mathrm{d}}{\mathrm{d}t}{}^{nS}\rho^K_Q(LJ,L'J') = &- \sum_{L''J''}\sum_{L'''J'''}\sum_{K'Q'}\Big[iN(nS;LJL'J'KQ;L''J''L'''J'''K'Q') \\
&+ R_A(nS;LJL'J'KQ;L''J''L'''J'''K'Q') \\
&+ R_S(nS;LJL'J'KQ;L''J''L'''J'''K'Q') \\
&+ R_E(nS;LJL'J'KQ;L''J''L'''J'''K'Q')\Big]\,{}^{nS}\rho^{K'}_{Q'}(L''J'',L'''J''') \\
&+ \sum_{n_l}\sum_{L_lJ_l}\sum_{L'_lJ'_l}\sum_{K_lQ_l}T_A(nS;LJL'J'KQ;n_lS;L_lJ_lL'_lJ'_lK_lQ_l)\,{}^{n_lS}\rho^{K_l}_{Q_l}(L_lJ_l,L'_lJ'_l) \\
&+ \sum_{n_u}\sum_{L_uJ_u}\sum_{L'_uJ'_u}\sum_{K_uQ_u}\Big[T_S(nS;LJL'J'KQ;n_uS;L_uJ_uL'_uJ'_uK_uQ_u) \\
&+ T_E(nS;LJL'J'KQ;n_uS;L_uJ_uL'_uJ'_uK_uQ_u)\Big]\,{}^{n_uS}\rho^{K_u}_{Q_u}(L_uJ_u,L'_uJ'_u),
\end{aligned} \tag{2.123}$$

where contribution of atomic Hamiltonian is

$$N(nS;LJL'J'KQ;L''J''L'''J'''K'Q') = \hbar^{-1}\sum_{MM'}\sqrt{(2K+1)(2K'+1)}\begin{pmatrix} J & J' & K \\ M & -M' & -Q\end{pmatrix}$$

$$\times\Bigg[\delta_{L'L'''}\delta_{J'J'''}\sum_{M''}(-1)^{J-M+J''-M''}\begin{pmatrix} J'' & J' & K' \\ M'' & -M' & -Q' \end{pmatrix} \times\langle nLSJM|\,H_A\,|nL''SJ''M''\rangle$$
$$-\delta_{LL''}\delta_{JJ''}\sum_{M'''}\begin{pmatrix} J & J''' & K' \\ M & -M''' & -Q' \end{pmatrix} \times\langle nL'''SJ'''M'''|\,H_A\,|nL'SJ'M'\rangle\Bigg], \tag{2.124}$$

where rate for absorption from lower levels is

$$\begin{aligned} T_A(nS;LJL'J'KQ;n_lS;L_lJ_lL'_lJ'_lK_lQ_l) &= \frac{16\pi^3}{3}\frac{e_0^2a_0^2}{\hbar^2c}\Lambda(n_lL_l,nL)\Lambda(n_lL'_l,nL')(-1)^{J'_l-J_l+K_l-Q_l} \\ &\times\sqrt{(2J+1)(2J_l+1)(2J'+1)(2J'_l+1)} \\ &\times\begin{Bmatrix} J & J_l & 1 \\ L_l & L & S \end{Bmatrix}\begin{Bmatrix} J' & J'_l & 1 \\ L'_l & L' & S \end{Bmatrix} \\ &\times\sum_{K_rQ_r}\sqrt{3(2K+1)(2K_l+1)(2K_r+1)} \\ &\times\begin{Bmatrix} K & K_l & K_r \\ J & J_l & 1 \\ J' & J'_l & 1 \end{Bmatrix}\begin{pmatrix} K & K_l & K_r \\ -Q & Q_l & -Q_r \end{pmatrix}J^{Kr}_{Q_r}(\omega_{nn_l}), \end{aligned} \tag{2.125}$$

where rate for spontaneous emission from upper levels is

$$\begin{aligned} T_S(nS;LJL'J'KQ;n_uS;L_uJ_uL'_uJ'_uK_uQ_u) &= \frac{16\pi^3}{3}\frac{e_0^2a_0^2}{\hbar^2c}\Lambda(n_uL_u,nL)\Lambda(n_uL'_u,nL') \\ &\times(-1)^{J'_u-J_u+K_u-Q_u} \\ &\times\sqrt{(2J+1)(2J_u+1)(2J'+1)(2J'_u+1)} \\ &\times\begin{Bmatrix} J & J_u & 1 \\ L_u & L & S \end{Bmatrix}\begin{Bmatrix} J' & J'_u & 1 \\ L'_u & L' & S \end{Bmatrix} \\ &\times\sum_{K_rQ_r}(-1)^{K_r}\sqrt{3(2K+1)(2K_u+1)(2K_r+1)} \\ &\times\begin{Bmatrix} K & K_u & K_r \\ J & J_u & 1 \\ J' & J'_u & 1 \end{Bmatrix}\begin{pmatrix} K & K_u & K_r \\ -Q & Q_u & -Q_r \end{pmatrix} \\ &\times J^{Kr}_{Q_r}(\omega_{n_un}), \end{aligned} \tag{2.126}$$

where rate for stimulated emission from upper levels is

$$\begin{aligned} T_E(nS;LJL'J'KQ;n_uS;L_uJ_uL'_uJ'_uK_uQ_u) &= \frac{4}{3}\frac{e_0^2a_0^2}{\hbar c^3}\omega^3_{n_un}\Lambda(n_uL_u,nL)\Lambda(n_uL'_u,nL') \\ &\times\delta_{KK_u}\delta_{QQ_u}(-1)^{J'+J'_u+K+1} \\ &\times\sqrt{(2J+1)(2J_u+1)(2J'+1)(2J'_u+1)} \end{aligned}$$

$$\times \left\{ \begin{array}{ccc} J & J_u & 1 \\ L_u & L & S \end{array} \right\} \left\{ \begin{array}{ccc} J' & J'_u & 1 \\ L'_u & L' & S \end{array} \right\}$$
$$\times \left\{ \begin{array}{ccc} J & J' & K \\ J'_u & J_u & 1 \end{array} \right\},$$

(2.127)

where rate for absorption to upper levels is

$$\begin{aligned} R_A(nS; LJL'J'KQ; L''J''L'''J'''K'Q') &= \frac{16\pi^3}{3}\frac{e_0^2 a_0^2}{\hbar^2 c}\sum_{n_u L_u}\sum_{K_r Q_r}(-1)^{L_u - S + J - Q' + 1} \\ &\times\sqrt{3(2K+1)(2K'+1)(2K^r+1)} \\ &\times \left(\begin{array}{ccc} K & K' & K_r \\ Q & -Q' & Q_r \end{array} \right) J^{K_r}_{Q_r}(\omega_{n_u n}) \\ &\times\frac{1}{2}\Bigg[\delta_{LL''}\delta_{JJ''}(-1)^{L'+L'''}\sqrt{(2J'+1)(2J'''+1)} \\ &\times\Lambda(nL', n_u L_u)\Lambda(nL''', n_u L_u) \\ &\times \left\{ \begin{array}{ccc} L' & L''' & K_r \\ J''' & J' & S \end{array} \right\} \left\{ \begin{array}{ccc} L' & L''' & K_r \\ 1 & 1 & L_u \end{array} \right\} \\ &\times \left\{ \begin{array}{ccc} K & K' & K_r \\ J''' & J' & J \end{array} \right\} \\ &+\delta_{L'L'''}\delta_{J'J'''}(-1)^{L+L''+J'-J''+K+K'+K_r} \\ &\times\sqrt{(2J+1)(2J''+1)}\Lambda(nL, n_u L_u)\Lambda(nL'', n_u L_u) \\ &\times \left\{ \begin{array}{ccc} L & L'' & K_r \\ J'' & J & S \end{array} \right\} \left\{ \begin{array}{ccc} L & L'' & K_r \\ 1 & 1 & L_u \end{array} \right\} \\ &\times \left\{ \begin{array}{ccc} K & K' & K_r \\ J'' & J & J' \end{array} \right\}\Bigg], \end{aligned}$$

(2.128)

where rate for spontaneous emission to lower levels is

$$\begin{aligned} R_S(nS; LJL'J'KQ; L''J''L'''J'''K'Q') &= \frac{16\pi^3}{3}\frac{e_0^2 a_0^2}{\hbar^2 c}\sum_{n_l L_l}\sum_{K_r Q_r}(-1)^{L_l - S + J + K_r - Q' + 1} \\ &\times\sqrt{3(2K+1)(2K'+1)(2K^r+1)} \\ &\times \left(\begin{array}{ccc} K & K' & K_r \\ Q & -Q' & Q_r \end{array} \right) J^{K_r}_{Q_r}(\omega_{n n_l}) \\ &\times\frac{1}{2}\Bigg[\delta_{LL''}\delta_{JJ''}(-1)^{L'+L'''}\sqrt{(2J'+1)(2J'''+1)} \\ &\times\Lambda(nL', n_l L_l)\Lambda(nL''', n_l L_l) \\ &\times \left\{ \begin{array}{ccc} L' & L''' & K_r \\ J''' & J' & S \end{array} \right\} \left\{ \begin{array}{ccc} L' & L''' & K_r \\ 1 & 1 & L_l \end{array} \right\} \\ &\times \left\{ \begin{array}{ccc} K & K' & K_r \\ J''' & J' & J \end{array} \right\} \end{aligned}$$

$$
\begin{aligned}
&+\delta_{L'L'''}\delta_{J'J'''}(-1)^{L+L''+J'-J''+K+K'+K_r} \\
&\times\sqrt{(2J+1)(2J''+1)}\Lambda(nL,n_lL_l)\Lambda(nL'',n_lL_l) \\
&\times\left\{\begin{array}{ccc} L & L'' & K_r \\ J'' & J & S \end{array}\right\}\left\{\begin{array}{ccc} L & L'' & K_r \\ 1 & 1 & L_l \end{array}\right\} \\
&\times\left\{\begin{array}{ccc} K & K' & K_r \\ J'' & J & J' \end{array}\right\}\Bigg],
\end{aligned}
\tag{2.129}
$$

and where rate for stimulated emission to lower levels is

$$
\begin{aligned}
R_E(nS;LJL'J'KQ;L''J''L'''J'''K'Q') &= \frac{4}{3}\frac{e_0^2a_0^2}{\hbar c^3}\delta_{LL''}\delta_{L'L'''}\delta_{JJ''}\delta_{J'J'''}\delta_{KK'}\delta_{QQ'} \\
&\quad\times\sum_{n_lL_l}\omega_{nn_l}^3\frac{1}{2}[(2L+1)^{-1}\Lambda^2(nL,n_lL_l) \\
&\quad+(2L'+1)^{-1}\Lambda^2(nL',n_lL_l)].
\end{aligned}
\tag{2.130}
$$

The quantity $\Lambda(nL,n'L')$ is given for $n=n'$ as

$$
\Lambda(nL,nL')=\sqrt{(2L+1)(2L'+1)}\begin{pmatrix} L & L' & 1 \\ 0 & 0 & 0 \end{pmatrix}\langle nL|\,r\,|nL'\rangle\,, \tag{2.131}
$$

where

$$
\langle nL|\,r\,|nL-1\rangle=\frac{3}{2}n\sqrt{n^2-L^2}=\langle nL-1|\,r\,|nL\rangle\,,
$$

and for $n\neq n'$ as

$$
\Lambda(nL,n'L')=(-1)^L\sqrt{\frac{3(2L+1)\hbar c^3}{4e_0^2a_0^2\omega_{nL,n'L'}^3}A(nL,n'L')}, \tag{2.132}
$$

where $A(nL,n'L')$ is the Einstein coefficient for spontaneous de-excitation. The meanings of the rates and the primes are illustrated in figure 2.16.

2.3.3 Radiative transfer equation

Intensity of a radiation beam is

$$
I(\nu,\vec{\Omega})=\frac{h\nu^3}{c^2}\sum_{\lambda=1,2}n(\nu,\vec{\Omega},\lambda), \tag{2.133}
$$

where $n(\nu,\vec{\Omega},\lambda)$ is the number of photons in a unit range about a particular frequency and a particular propagation direction $\vec{\Omega}$, and where λ indicates two complex unit vectors both perpendicular to $\vec{k}$ and perpendicular to each other. In the form of the quantum mechanical operator, it is written as

$$
\hat{I}(\nu,\vec{\Omega})=\frac{h\nu^3}{c^2}\sum_{\lambda=1,2}a^\dagger(\nu,\vec{\Omega},\lambda)a(\nu,\vec{\Omega},\lambda), \tag{2.134}
$$

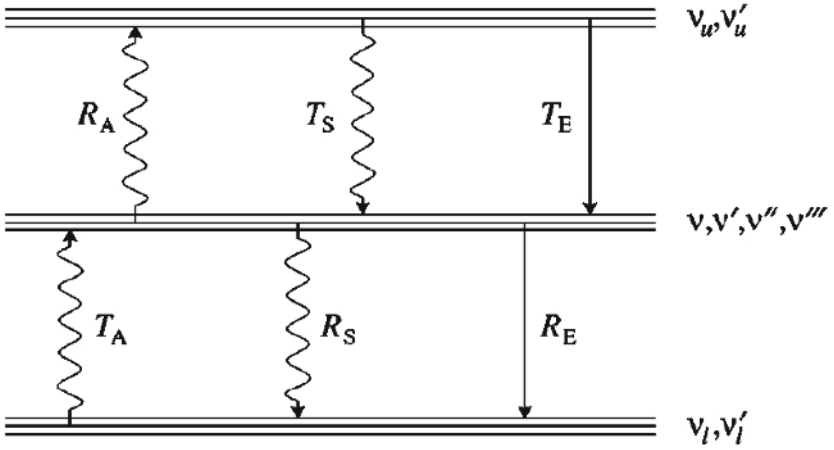

Figure 2.16: The different radiative processes in the multi-term atom. Straight arrows indicate spontaneous emission processes, whereas wiggly lines indicate radiation-induced processes (absorption and stimulated emission) [14].

and

$$\hat{I}_{\alpha\beta}(\nu,\vec{\Omega}) = \frac{h\nu^3}{c^2} a^\dagger(\nu,\vec{\Omega},\alpha)a(\nu,\vec{\Omega},\beta) \tag{2.135}$$

generate the polarization tensor defined as

$$\frac{1}{2}\begin{pmatrix} I+Q & U-iV \\ U+iV & I-Q \end{pmatrix}. \tag{2.136}$$

This operator remains unchanged in the interaction picture.

Substituting eq. (2.136) into eq. (2.106) leads to

$$\begin{aligned} \frac{\mathrm{d}}{\mathrm{d}t} I_{\alpha\beta}(\nu,\vec{\Omega}) &= -\frac{4\pi^2\nu^3}{hc^2}\mathrm{Tr}\Big\{\int_0^t \Big[[a^\dagger(\nu,\vec{\Omega},\alpha)a(\nu,\vec{\Omega},\beta), B(t)], B^\dagger(t')\Big]\rho_{\mathrm{I}}(t')\mathrm{d}t'\Big\} \\ &\quad + c.c.\ \{\alpha \rightleftharpoons \beta\}. \end{aligned} \tag{2.137}$$

With some algebra and the helps of eqs. (2.116) and (2.121), we obtain

$$\begin{aligned} \frac{\mathrm{d}}{\mathrm{d}t} I_{\alpha\beta}(\nu,\vec{\Omega}) &= \Bigg\{\frac{4\pi^3\nu}{h\mathcal{V}}\sum_\gamma\sum_{mm'n}[\vec{d}\cdot\vec{e}_\alpha(\vec{\Omega})]_{mn}[\vec{d}\cdot\vec{e}_\gamma(\vec{\Omega})^*]_{nm'}\rho_{m'm}\Phi(\nu_{mn}-\nu)I_{\gamma\beta}(\nu,\vec{\Omega}) \\ &\quad + \frac{4\pi^3\nu^4}{c^2\mathcal{V}}\sum_{mm'n}[\vec{d}\cdot\vec{e}_\alpha(\vec{\Omega})]_{mn}[\vec{d}\cdot\vec{e}_\beta(\vec{\Omega})^*]_{nm'}\rho_{m'm}\Phi(\nu_{mn}-\nu) \\ &\quad - \frac{4\pi^3\nu}{h\mathcal{V}}\sum_\gamma\sum_{mnn'}[\vec{d}\cdot\vec{e}_\alpha(\vec{\Omega})]_{mn}[\vec{d}\cdot\vec{e}_\gamma(\vec{\Omega})^*]_{n'm}\rho_{nn'}\Phi(\nu_{mn}-\nu)I_{\gamma\beta}(\nu,\vec{\Omega})\Bigg\} \\ &\quad + c.c.\ \{\alpha \rightleftharpoons \beta\}, \end{aligned} \tag{2.138}$$

where $\mathcal{V}$ is volume.Equation (2.138) is interpreted as an evolution equation for the polarization tensor in the phase space of photon occupation numbers. To replace the

phase space by the ordinary three dimension space, we can replace the time derivative in eq. (2.138) with

$$\frac{\mathrm{d}}{\mathrm{d}t} \rightarrow \frac{\partial}{\partial t} + c\frac{\mathrm{d}}{\mathrm{d}s}, \tag{2.139}$$

where s is the spatial coordinate along the direction $\vec{\Omega}$. In addition, for an ensemble of uncorrelated atomic system, we can replace the factor $1/\mathcal{V}$ by the number density N under assumption that the radiation field, which has volume of $\mathcal{V}$, interacts with a single atomic system. Moreover, by using transformation from the polarization tensor into the Stokes parameters, we obtain general radiative transfer equations of Stokes vectorss,

$$\begin{aligned}
\Big(\frac{\partial}{\partial t} + c\frac{\mathrm{d}}{\mathrm{d}s}\Big)\begin{pmatrix} I \\ Q \\ U \\ V \end{pmatrix} = & - \begin{pmatrix} \eta_I^{(a)} & \eta_Q^{(a)} & \eta_U^{(a)} & \eta_V^{(a)} \\ \eta_Q^{(a)} & \eta_I^{(a)} & \rho_V^{(a)} & -\rho_U^{(a)} \\ \eta_U^{(a)} & -\rho_V^{(a)} & \eta_I^{(a)} & \rho_Q^{(a)} \\ \eta_V^{(a)} & \rho_U^{(a)} & -\rho_Q^{(a)} & \eta_I^{(a)} \end{pmatrix}\begin{pmatrix} I \\ Q \\ U \\ V \end{pmatrix} \\
& + \begin{pmatrix} \eta_I^{(s)} & \eta_Q^{(s)} & \eta_U^{(s)} & \eta_V^{(s)} \\ \eta_Q^{(s)} & \eta_I^{(s)} & \rho_V^{(s)} & -\rho_U^{(s)} \\ \eta_U^{(s)} & -\rho_V^{(s)} & \eta_I^{(s)} & \rho_Q^{(s)} \\ \eta_V^{(s)} & \rho_U^{(s)} & -\rho_Q^{(s)} & \eta_I^{(s)} \end{pmatrix}\begin{pmatrix} I \\ Q \\ U \\ V \end{pmatrix} + \begin{pmatrix} \epsilon_I \\ \epsilon_Q \\ \epsilon_U \\ \epsilon_V \end{pmatrix}
\end{aligned} \tag{2.140}$$

where absorption matrix

$$\begin{aligned}
\eta_i^{(a)}(\omega,\vec{k}) = & \frac{4\pi^2}{3}\frac{e_0^2 a_0^2}{\hbar c} N\omega \sum_{L_l J_l M_l}\sum_{L_l' J_l' M_l'}\sum_{L_l'' J_l'' M_l''}\sum_{L_u J_u M_u}\sum_{L_u' J_u' M_u'}\sum_{qq'}(-1)^{J_l''-M_l''+M_u-M_u'+q'+1} \\
& \times \sum_{\mu_l\mu_u} C^{\mu_l}_{L_l J_l M_l}(n_l S) C^{\mu_l}_{L_l'' J_l'' M_l''}(n_l S) C^{\mu_u}_{L_u J_u M_u}(n_u S) C^{\mu_u}_{L_u' J_u' M_u'}(n_u S) \\
& \times \sum_{KQ}\sum_{K_l Q_l}\sqrt{3(2K+1)(2K_l+1)}\begin{pmatrix} J_u & J_l & 1 \\ -M_u & M_l & q \end{pmatrix}\begin{pmatrix} J_u' & J_l' & 1 \\ -M_u' & M_l' & q' \end{pmatrix} \\
& \times \begin{pmatrix} 1 & 1 & K \\ -q & q' & -Q \end{pmatrix}\begin{pmatrix} J_l'' & J_l' & K_l \\ M_l'' & -M_l' & -Q_l \end{pmatrix}\begin{Bmatrix} L_u & L_l & 1 \\ J_l & J_u & S \end{Bmatrix}\begin{Bmatrix} L_u' & L_l' & 1 \\ J_l' & J_u' & S \end{Bmatrix} \\
& \times \sqrt{(2J_u+1)(2J_u'+1)(2J_l+1)(2J_l'+1)}\Lambda(n_u L_u, n_l L_l)\Lambda(n_u L_u', n_l L_l') \\
& \times \mathrm{Re}\{T_Q^K(i,\vec{k})\,{}^{n_l S}\rho_{Q_l}^{K_l}(L_l'' J_l'', L_l' J_l')\Phi(\omega_{n_u\mu_u,n_l\mu_l}-\omega)\}
\end{aligned} \tag{2.141}$$

and scattering matrix

$$\begin{aligned}
\eta_i^{(s)}(\omega,\vec{k}) = & \frac{4\pi^2}{3}\frac{e_0^2 a_0^2}{\hbar c} N\omega \sum_{L_u J_u M_u}\sum_{L_u' J_u' M_u'}\sum_{L_u'' J_u'' M_u''}\sum_{L_l J_l M_l}\sum_{L_l' J_l' M_l'}\sum_{qq'}(-1)^{J_u'-M_u+q'+1} \\
& \times \sum_{\mu_u\mu_l} C^{\mu_u}_{L_u J_u M_u}(n_u S) C^{\mu_u}_{L_u'' J_u'' M_u''}(n_u S) C^{\mu_l}_{L_l J_l M_l}(n_l S) C^{\mu_l}_{L_l' J_l' M_l'}(n_l S) \\
& \times \sum_{KQ}\sum_{K_u Q_u}\sqrt{3(2K+1)(2K_u+1)}\begin{pmatrix} J_u & J_l & 1 \\ -M_u & M_l & q \end{pmatrix}\begin{pmatrix} J_u' & J_l' & 1 \\ -M_u' & M_l' & q' \end{pmatrix}
\end{aligned}$$

$$\times \begin{pmatrix} 1 & 1 & K \\ -q & q' & -Q \end{pmatrix} \begin{pmatrix} J'_u & J''_u & K_u \\ M'_u & -M''_u & -Q_u \end{pmatrix} \begin{Bmatrix} L_u & L_l & 1 \\ J_l & J_u & S \end{Bmatrix} \begin{Bmatrix} L'_u & L'_l & 1 \\ J'_l & J'_u & S \end{Bmatrix}$$
$$\times \sqrt{(2J_u+1)(2J'_u+1)(2J_l+1)(2J'_l+1)}\Lambda(n_uL_u, n_lL_l)\Lambda(n_uL'_u, n_lL'_l)$$
$$\times \mathrm{Re}\{T^K_Q(i,\vec{k})^{\,n_uS}\rho^{K_u}_{Q_u}(L'_uJ'_u, L''_uJ''_u)\Phi(\omega_{n_u\mu_u,n_l\mu_l}-\omega)\} \tag{2.142}$$

$$\rho^{(a)}_i(\nu,\vec{\Omega}) = \eta^{(a)}_i(\nu,\vec{\Omega})\ \{\mathrm{Re}\to\mathrm{Im}\} \tag{2.143}$$

$$\rho^{(s)}_i(\nu,\vec{\Omega}) = \eta^{(s)}_i(\nu,\vec{\Omega})\ \{\mathrm{Re}\to\mathrm{Im}\} \tag{2.144}$$

$$\epsilon_i(\nu,\vec{\Omega}) = \frac{2h\nu^3}{c^2}\eta^{(s)}_i(\nu,\vec{\Omega}), \tag{2.145}$$

where the symbol $\{\mathrm{Re}\to\mathrm{Im}\}$ means substitution of the imaginary part for the real part. The density matrix and the profile function represent atomic polarization and the wavelength dependent polarization across the spectral line (Zeeman effect and Stark effect), respectively.

The Stokes vectors are solved by the radiative transfer equations using the density matrix, while the density matrix elements are solved by the statistical equilibrium equations from the local radiation field. Thus we need iterative schemes to solve the Stokes vector until the self-consistency of the two solutions of the radiative transfer equations and the statistical equilibrium equations is achieved.

Chapter 3

Developments of the Wideband Spectropolarimeter of the Domeless Solar Telescope at Hida Observatory

3.1 INTRODUCTION

Recently, the developments of polarimeter enable us to detect the weak polarization in spectral lines (e.g. Zurich Imaging Stokes Polarimeter II [86] , Tenerife Infrared Polarimeter II [32] , and Facility Infrared Spectro-polarimeter [33]). If the polarization sensitivity of 10^{-4} is achieved, we can detect the Hanle effect, a modification of the coherent scattering polarization by magnetic field. The Hanle effect provides us an opportunity to diagnose small scale turbulent or tangled magnetic fields [87] and weak magnetic fields that cannot be reached with the Zeeman effect. On the other hand, some polarization line profiles produced by coherent scattering, ex. Na I D_1, are not understood with the current quantum mechanical description [88] and atomic polarization of metastable level are still enigmatic [30] .

The Stark effect and anisotropic collisional excitation (impact) of atoms also produce a polarization of spectral lines of the order of 10^{-3}. The Stalk effect would enable us to diagnose an electric field induced, for example, when neutral atoms move across a magnetic field [43] , and the impact polarization would enable us to diagnose anisotropy of velocity distribution of particles by heat conduction or accelerated high-energy particles which penetrate into the chromosphere [59] . However studies incorporating these effects are quite limited so fer.

In order to utilise these polarization mechanisms to open a new window of plasma diagnostics, we developed a system which enable us to make precise spectro-polarimetric observations in a photometric accuracy of 10^{-3}- 10^{-4} for wide wavelength range in visible and near infrared. The requirements on the accuracy and the sensitivity of the

polarization calibration to achieve our aim are established in the same manner as Ichimoto et al. [89] , but with different parameters; i.e., the statistical noise, the allowable scale error, maximum incoming linear polarization, and maximum incoming circular polarization to be 10^{-4}, 0.05, 0.02, and 0.02, respectively. In the following sections, we describe the detail of new developed polarimeter (Section 3.2), calibration of instrumental polarization of the telescope (Section 3.3), and finally discuss and summarize our developments (Section 3.4).

3.2 New polarimeter

The new polarimeter is a successor of formerly developed polarimeter on the Domeless Solar Telescope (DST) at Hida observatory, which was aimed to measure the vector magnetic fields in the photosphere [18] . The system consists of a 60 cm aperture vacuum telescope, a high dispersion vertical vacuum spectrograph, polarization modulator and analyser composed of a rotating waveplate and Wallaston prisms located closely behind the focus of the telescope, and a CCD camera or infrared camera. Details of DST will be described in section 3.3. The vacuum spectrograph is equipped with a grating of $306 \times 408\,\mathrm{mm}^2$ ruled area, of 632 grooves/mm, and Blaze angle is 56° [90] . The length of the spectrograph slit is 20 mm that corresponds to the angular scale of 128 arcsec, or 26.6 Mm on the sun. Entire spectrograph including the entrance slit, rotating waveplate and polarization analyzer is rotatable about the vertical optical axis of the DST.

Observed intensity of spectrum $I_{\pm}^{\mathrm{obs}}$ in orthogonal polarizations separated by the polarization analyzer can be written with the following forms as functions of the rotation angle of the waveplate (θ_i) at the ith exposure start time.

$$I_{\pm}^{\mathrm{obs}}(\theta_i) = \frac{1}{2}(1-r^2)\,\epsilon\,R_{\pm}\Big[\Big\{1 \pm C_1 \cos\{2\,(\theta_i+\beta)\}\Big\}\,I^{\mathrm{in}} \pm \Big\{C_2 \cos\{4\,(\theta_i+\beta)\} + C_3\Big\}\,Q^{\mathrm{in}} \pm C_2 \sin\{4\,(\theta_i+\beta)\}\;U^{\mathrm{in}} \mp C_4 \sin\{2\,(\theta_i+\beta)\}\;V^{\mathrm{in}}\Big]$$

$$\begin{aligned} C_1 &= -2\,r^2\,\frac{T}{2\pi\epsilon}\sin\left(\frac{2\pi\epsilon}{T}\right)\sin\left(\frac{4\pi dn}{\lambda}\right)\sin\delta \\ C_2 &= \frac{T}{4\pi\epsilon}\sin\left(\frac{4\pi\epsilon}{T}\right)\frac{1-\cos\delta}{2} \\ C_3 &= \frac{1+\cos\delta}{2} \\ C_4 &= \frac{T}{2\pi\epsilon}\sin\left(\frac{2\pi\epsilon}{T}\right)\sin\delta \\ \beta &= \pi\frac{\epsilon}{T} + \alpha \end{aligned}$$

where $\pm$ indicate each light of dual orthogonal beam, $(I^{\mathrm{in}}, Q^{\mathrm{in}}, U^{\mathrm{in}}, V^{\mathrm{in}})$ are the Stokes vector of the incident light to the spectrograph, λ is the wavelength, $R_{\pm}$ is transmittance of spectrograph for each beam, ϵ is the exposure time, and α is the angle between the fast axis of the waveplate and the direcion of the polarization axis of the Wallaston

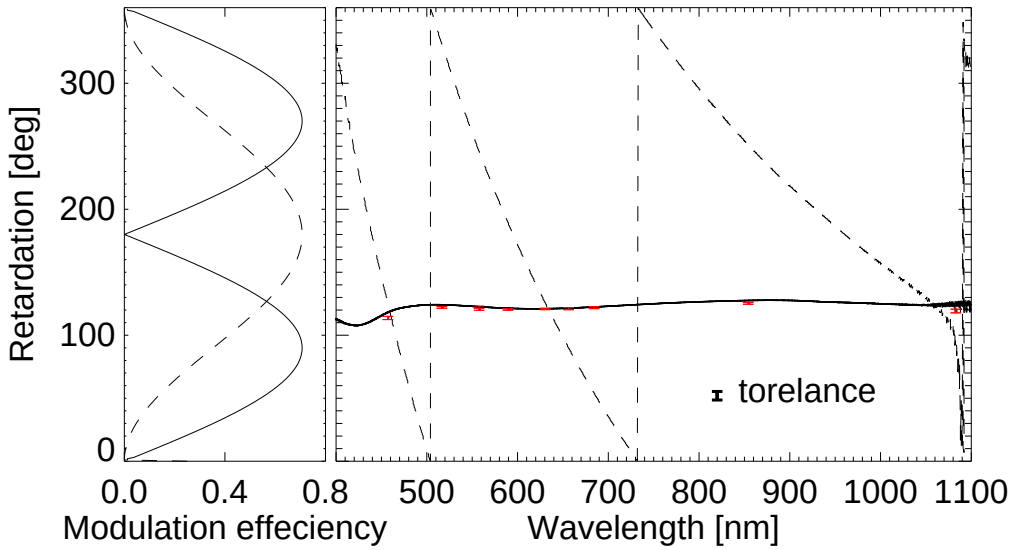

Figure 3.1: Retardation of waveplates used as modulator (right) and modulation efficiency [15] as function of a retardation (left). In the left panel, solid line and dashed lines indicate the modulation efficiency for circular and linear polarizations, respectively. In the right panel, Black solid line and dashed lines are retardation of the APSAW and the quartz waveplate measured by using a photopolarimetric measurement system of Mueller matrix with dual rotating waveplates [16] , respectively. Red symbols are the retardation of APSAW derived from intensity modulation observed when complete linear polarized light incident on our modulator with analyzer.

prism when the first exposure is triggered. T, δ, r, d, and n are the rotation period, the retardation, the surface reflectivity, the thickness, and the refractive index of the waveplate, respectively. On the focal plane of DST, we define an axis of Wollaston prism that is perpendicular to the spectrograph slit as positive Q. $\mathbf{S}^{\rm in} \equiv (I^{\rm in}, Q^{\rm in}, U^{\rm in}, V^{\rm in})$ and $\mathbf{\Delta I}^{\rm obs} \equiv \left(\frac{I_+^{\rm obs}(\theta_1) - I_-^{\rm obs}(\theta_1) R_+/R_-}{2}, \ldots, \frac{I_+^{\rm obs}(\theta_n) - I_-^{\rm obs}(\theta_n) R_+/R_-}{2}\right)$ are connected with a $4 \times n$ 'modulation matrix' $\mathbf{M}$.

$$
\begin{aligned}
\Delta I_i^{\rm obs} &= \sum_{j=1}^{4} M_{ij}\, S_j^{\rm in} \\
&= \frac{1}{2}(1-r^2)\,\epsilon\, R_+ \Big[C_1 \cos\left\{2\left(\theta_i + \beta\right)\right\} I^{\rm in} + \Big\{ C_2 \cos\left\{4\left(\theta_i + \beta\right)\right\} + C_3 \Big\} Q^{\rm in} \\
&\quad + C_2 \sin\left\{4\left(\theta_i + \beta\right)\right\} U^{\rm in} - C_4 \sin\left\{2\left(\theta_i + \beta\right)\right\} V^{\rm in} \Big]
\end{aligned}
$$

The inverse matrix $\mathbf{W}$ of the modulation matrix $\mathbf{M}$ can be obtained with the following form, and we are able to get the input Stokes vector as the product of $\mathbf{W}$ and $\mathbf{\Delta I^{obs}}$,

$$\mathbf{W} = (\mathbf{M}^T \mathbf{M})^{-1} \mathbf{M}^T,$$

where the superscript T denotes the transpose of the matrix. Our tolerance of the retardation, the rotation angle, and the stability of exposure time are determined in the same manner as Ichimoto et al. [89] and are 3.4°, 0.07°, and 100 μs, respectively.

Figure 3.1 shows the modulation efficiencies for Stokes-Q, U, and V as a function of the retardation of the waveplate and the measured retardation of our waveplates as a function of wavelength. In the former system [18] , the wavelength range of high modulation efficiency is limited with a 163 μm thick quartz waveplate and it took 30 s to take 16 images with a slow camera and step-wise motion of the rotating waveplate. In the new system, the polarimeter is equipped with a fast and high sensitive CCD camera (Procilica GE1650, manufactured by Allied Vision Technologies Co.), a infrared camera (XEVA-1.7-640, manufactured by Xenics Co.), Super-Achromatic True Zero-Order Waveplates (APSAW, manufactured by Astropribor Co.), and a continuously rotating waveplate equipped with an origin sensor on it. APSAW have high modulation efficiency in a wavelength range from 400 nm to 1100 nm. Wide wavelength range is covered by using one of the CCD camera and the infrared camera. The origin sensor produces a trigger for the camera to start a sequence of exposures for both orthogonal polarization spectra split by the Wallaston prisms. Maximum frame rate at full resolution is about 30 frames per second. Thus the new system enable us to take spectral images in both orthogonal polarizations simultaneously with a frame rate of $\sim$30 Hz for wide range of wavelength while the waveplate rotates continuously in a rate of 1 Hz.

It takes $\sim$30 s and $\sim$60 s to achieve photon random noise to 10^{-3} in visible and near infrared in typical setup with the spatial sampling of 0.4 arcsec and spectral sampling of 4 pm in visible (589 nm) and of 0.6 arcsec and spectral sampling of 3 pm in infrared

(1083 nm), respectively, while it takes more than ∼150 s by the former system in visible to achieve the same noise level. The accuracy of the rotation angle and the retardation of waveplate are verified within our tolerance. The accuracy of the exposure time of camera is 1 μs within our tolerance. In typical observation, we take 16 - 20 exposures in one rotation of the waveplate, and demodulation is made by extracting the $\cos 2\theta$, $\sin 4\theta$ and $\cos 4\theta$ components from the observed intensity modulation for Stokes-V, Q, and U, respectively. Although interference fringes produced by internal reflection of the waveplate modulate the intensity in similar way with the Stokes-V, the fringes do not effect on the measurement of Stokes vector, since its modulation is 90° apart in phase from the Stokes-V signal. Two orthogonaly polarized spectra are aligned and combined to eliminate the intensity variations caused by seeing and guiding error during the integration.

3.3 Instrumental Polarization of DST

The DST is a 60 cm aperture Newton-Gregorian type telescope on alt-azimuth mount [91], [90]. Figure 3.2 shows the ray path along the DST and its optical components. The solar ray goes through an entrance window and an entrance pupil with an aperture of 600 mm before it reaches a primary mirror that has 633 mm of diameter. The primary mirror with a focal length of 3.150 m ($F5.1$) produces a 3 cm solar image on the elevation axis of the tube, which is 21.5 m high from the ground level. The conversing light reflected by the Newton mirror passes through a central hole of the Coude mirror and reaches to the Gregory secondary mirror with a diameter of 452 mm. Then after reflected by the Coude mirror and transmitting the exit-window, the Gregory secondary mirror forms a 300 mm solar image at the observing table of the spectrograph. The space between the entrance-window and the exit-window is kept vacuum down to 2 mmHg to avoid air turbulence.

The entrance and exit windows are 40 mm in thickness and made of BK7 and UBK7, respectively. They are also coated with MgF_2 to increase the UV transmission. All mirrors are aluminized and made of Zerodur. In addition to being aluminized, the Newton, secondary, and Coude mirror are also overcoated with Zeiss-H08 coating to increase the reflectivity.

It is important to calibrate the instrumental polarization of the DST to realize accurate polarization measurement, because the two flat oblique mirrors (Newton mirror and Coude mirror) of the DST produce a non-negligible instrumental polariztion. The telescope Muellar matrix model we consider is almost the same as that of Makita et al. [92], Kiyohara et al. [18], and Hanaoka [17]. Their model can represent the instrumental polarization with an accuracy of 0.009 at 630 nm [17]. Since the details of the coating of mirrors are unknown, we set thier properties as unknown parameters of the model for wide range of wavelength and obtained them by fitting the model with

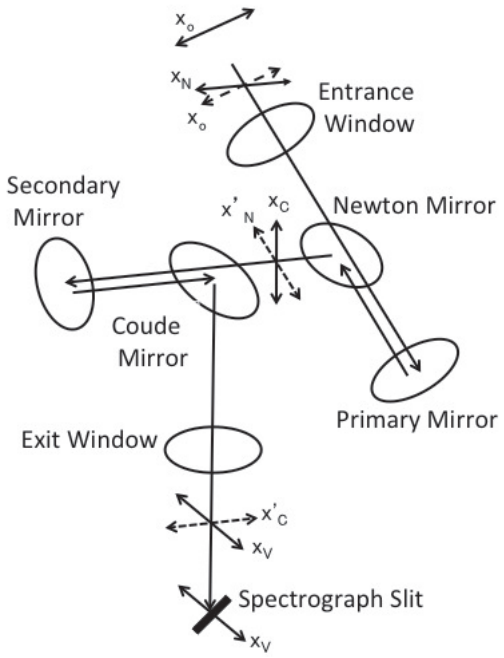

Figure 3.2: The ray path along the DST. The arrows x_N (x'_N) and x_C (x'_C) are included in the incident and reflection plane of the Newton and Coude mirrors, respectively. The arrow x_o indicates the reference coordinate of the Stokes vector of the light entering into the DST. The arrow x_V is the direction of analyzer in perpendicular to the slit of the vertical spectrograph.

observation data obtained by introducing known polarized light into the telescope.

3.3.1 DST polarization model

The propagation of the polarization through the DST is described by the product of the Mueller matrices of individual optical elements in proper order including rotation matrix of the coordinate. Mechanical stress on the two windows could make them act as a weak linear retarder [93] and each 4 mirrors is described as the product of a linear retarder and a linear polarizer

$$\mathbf{M} = \frac{1}{1+p} \begin{pmatrix} 1 & p & 0 & 0 \\ p & 1 & 0 & 0 \\ 0 & 0 & -\sqrt{1-p^2}\cos\tau & -\sqrt{1-p^2}\sin\tau \\ 0 & 0 & \sqrt{1-p^2}\sin\tau & -\sqrt{1-p^2}\cos\tau \end{pmatrix},$$

where p and τ are the difference of reflectivity and phase between the polarizations which are parallel and perpendicular to the plane of incidence, respectively. The axis of positive Q is defined as included in the plane defined by incident and reflected rays at each surface.

In our polarimetric system, direction of positive Q of the incident light is defined as the east-west direction (x_o) on the celestial sphere (figure 3.2).The Mueller matrix

of DST, $\mathbf{T_{DST}}$, is written as

$$\mathbf{T_{DST}} = \mathbf{S}\ \mathbf{R}(-\theta_{ex})\mathbf{D_{ex}}\mathbf{R}(\theta_{ex})\ \mathbf{R}(-\theta_C)\mathbf{M_C}\mathbf{R}(\theta_C)\ \mathbf{R}(-\theta_G)\mathbf{M_G}\mathbf{R}(\theta_G)$$

$$\mathbf{R}(-\theta_N)\mathbf{M_N}\mathbf{R}(\theta_N)\ \mathbf{R}(-\theta_P)\mathbf{M_P}\mathbf{R}(\theta_P)\ \mathbf{R}(-\theta_{en})\mathbf{D_{en}}\mathbf{R}(\theta_{en}),$$

where $\mathbf{D_{ex}}$ and $\mathbf{D_{en}}$ are the Mueller matrices of exit and entrance window, respectively. $\mathbf{M_C}$, $\mathbf{M_G}$, $\mathbf{M_N}$, and $\mathbf{M_P}$ are the Mueller matrices of Coude, Gregorian secondary, Newton, and Primary mirror, respectively. $\mathbf{R}$ is the rotation matrix and θ_{en}, θ_P, θ_N, θ_G, θ_C, and θ_{ex} are the angle between positive Q of the incident light and the axis of the entrance window, the primary mirror, the Newton mirror, the Gregorian secondary mirror, the Coude mirror, and the exit window, respectively. In addtion to the DST model described in Makita et al. [92] , we consider an effect of unpolarized stray light in the telescope which is written as a fictitious Mueller matrix

$$\mathbf{S} = \begin{pmatrix} 1+s & 0 & 0 & 0 \\ 0 & 1 & 0 & 0 \\ 0 & 0 & 1 & 0 \\ 0 & 0 & 0 & 1 \end{pmatrix},$$

where s is the fraction of stray light in the intensity.

Primary mirror, Gregorian secondary mirror and two windous are regarded as ideal ones in polarization, because they are symmetry with respect to the optical axis and the incident angle to them are very small. Thus we can rewrite the Mueller matrix of DST

$$\mathbf{T'_{DST}} = \mathbf{S}\,\mathbf{M_C}\mathbf{M_G}\mathbf{R}(\phi_\mathbf{C})\mathbf{M_N}\mathbf{M_P}\mathbf{R}(\phi_\mathbf{N}),$$

where $\mathbf{M_G}$ and $\mathbf{M_P}$ are as the follows.

$$\mathbf{M_G} = \mathbf{M_P} = \begin{pmatrix} 1 & 0 & 0 & 0 \\ 0 & 1 & 0 & 0 \\ 0 & 0 & -1 & 0 \\ 0 & 0 & 0 & -1 \end{pmatrix},$$

ϕ_N is the angle between x_o and x_N, and ϕ_C is the angle between x'_N and x_C, where x_N (x'_N) and x_C (x'_C) are axes included in the incident and reflection plane of the Newton and Coude mirrors, respectively (see Fig. 3.2).

The axis x'_C which is coordinate axis of the Coude mirror does not coincide with that of analyzer (x_V). The Mueller matrix of entire telescope, $\mathbf{T_V}$, thus include a rotating matrix of the angle between x'_C and x_V

$$\mathbf{T_V} = \mathbf{R}(\phi_\mathbf{V})\mathbf{S}\,\mathbf{M_C}\mathbf{M_G}\mathbf{R}(\phi_\mathbf{C})\mathbf{M_N}\mathbf{M_P}\mathbf{R}(\phi_\mathbf{N}). \tag{3.1}$$

where ϕ_V is the angle between x'_C and x_V. The angles in Equation (3.1) can be written using the hour angle θ_{HA} and the zenith distance θ_{ZD} of the sun as follows,

$$\phi_N \quad = \quad \theta_{ZA}$$

$$
\begin{aligned}
\phi_C &= \mp\theta_{ZD} \\
\phi_V &= \pm\theta_{ZD} - \theta_{ZA} + \theta_i \\
\theta_{ZA} &= \arcsin\Big(\frac{\cos\theta_{lat}\sin\theta_{HA}}{\sin\theta_{ZD}}\Big),
\end{aligned}
$$

where θ_{lat} is the latitude of Hida Observatory and the upper and the lower signs of $\pm$ or $\mp$ are for when the telescope tube is set westward and eastward to the rotation axis of the azimuth, respectively. Since the configuration and the Mueller matrix of DST change as the hour angle and the zenith distance of the sun, we need to record these angles during observation.

To calibrate instrumental polarization of DST, we consider only the effect of two flat oblique mirrors in the model of DST. Thus the model has five unknown parameters (p_N, τ_N, p_C, τ_C, s) where p_N and τ_N are p and τ of the Newton mirror, p_C and τ_C are p and τ of the Coude mirror. Our tolerances of p_N, τ_N, p_C, and τ_C are derived in the same manner as Ichimoto et al. [89] as 0.04, 0.3°, 0.04, and 0.3°, respectively.

3.3.2 A remotely controllable turret accommodating polarizer

To determine the Mueller matrix of DST, we need to measure polarizations transformed by DST from well-known different incident polarizations. We are able to derive five unknown parameters (p_N, τ_N, p_C, τ_C, s) of our DST model by introducing unpolarized light and linear polarizations in different orientations from the entrance window.

For this purpose, we developed a rotatable turret accommodating linear polarizers, which can be remotely controled from the observation room. The equipment is composed of two circular panels (Fig. 3.3). One works as the mask with fixed 8 holes and the other is a rotatable turret with 16 holes with a diameter of 48 mm. The rotatable turret accommodates 8 linear polarizers at every other holes with the same direction of the polarization axis, while the other 8 holes are open. The turret can be placed at 16 positions with 22.5° interval. When liner polarizers are under the mask hole, linearly polarized solar light enter the entrance window and when clear holes without polarizer are under the mask holes, solar light enter the window directly. The linear polarizers (Versalight, manufactured by Meadowlark Co.) constructed of a thin layer of Aluminum micro wires work as linear polarizer for wide wavelength range in visible and infrared.

Because it is difficult to lay a harness from observation room to the entrance of the telescope the rotatable turret is controled wirelessly by using 400 MHz radio waves from a PC in the observation room (Fig 3.4). An Absorbed Glass Mat battery set on the turret supplies the power and a solar cell auxiliary charges the battery to reduce the weight of the battery. The efficiency of our power system is quite high, because the solar cell always faces to the sun.

Requirements on the accuracy of the polarization angle and the side-runout of the turret are 0.5° and ±1°, respectively. A stepping motor and reduction gears drive the turret with a resolution of 0.003° where the backlash produced by gears is 0.001°. By the driving system and a sensor of origin of the rotating turret, the error of polarization angle is constantly smaller than that of the requirement on the angle accuracy. Measured side-runout of the turret is less than ±0.006°.

Figure 3.3: A picture of a remotely controllable turret accommodating linear polarization attached at the entrance window of DST.

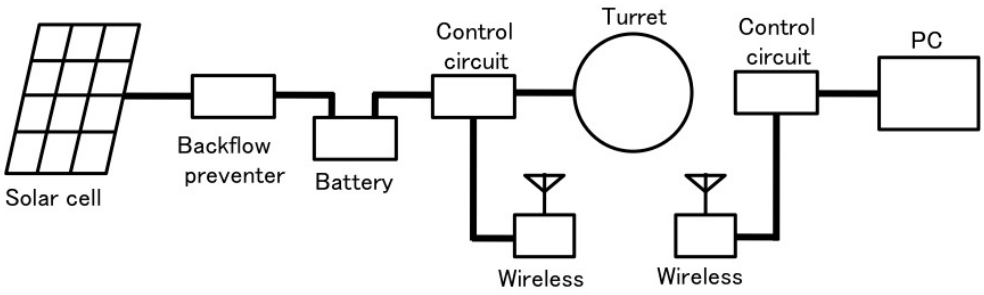

Figure 3.4: System diagram of the remotely controllable turret.

3.3.3 Calibration of instrumental polarization of DST

The remotely controllable turret accommodating linear polarizers is attached at the entrance window of the telescope to induce a well known polarized light (solar light, $I = Q$, $I = -Q$, $I = U$, or $I = -U$) into the telescope and we observed continuum light of a quiet region at the solar disk center for the whole day. The continuum light from the solar disk center is an ideal unpolarized light source whose polarization degree is $< 10^{-6}$ [94] . Table 3.1 show the list of calibration runs.

We developed the Mueller matrix model of DST to fit the observed data by Levenberg-Marquardt least-squares minimization method. Fitting parameters are five unknowns of the DST polarization model (p_N, τ_N, p_C, τ_C, s) and an angle offset of the origin of the remotely controllable turret. Figure 3.5 shows the one of results of fitting and Figure 3.6 is the obtained parameters (p_N, τ_N, p_C, τ_C, s) as function of the wavelength. DST produces the instrumental polarization if an ideal unpolarized light enters the entrance window of DST, and transform the polarization when a linear polarized light enter the window. Though observed instrumental polarization depends on the atitude of DST and inclination of the spectrograph slit, the Mueller matrix model of DST can reproduce the polarization well by tuning the 6 parameters with satisfactory small residuals of fitting as shown in Table 3.1.

The value of p_N, τ_N, p_C, and τ_C vary with the wavelength and the stray light s is a few par cent (Fig. 3.6). There are differences between these values when the telescope tube is set westward and eastward to the rotation axis of the azimuth. The origin angle of the remotely controllable turret changes with the observing day but the standard deviation of the angle is less than 0.2° on each day.

3.4 Discussion and Summary

In order to open a new window of plasma diagnostics by using Zeeman effect, Hanle effect, Stark effect and impact polarization, we developed a new spectropolarimeter on the Domeless Solar Telescope at Hida observatory. The polarimeter consists of a 60 cm aperture vacuum telescope, a high dispersion slit vacuum spectrograph, polarization modulator/analyzer composed of a rotating waveplate and Wollaston prisms, and a detector. With a quartz and a APSAW as the waveplate and CCD camera and infrared camera as the detector, the system enables us to observe in wide range of wavelength covering from 400 nm to 1100 nm. A photometric accuracy of 10^{-3} can be achieved in ∼30 s and ∼60 s in visible and near infrared, respectively.

Instrumental polarization of the telescope is modeled by a set of Mueller matrices, in which two oblique mirrors have actions on polarization but others are idealized. Unpolarized and linearly polarized lights are introduced into the telescope by using a remotely controllable turret attached at the entrance window of the telescope, and

Table 3.1: Information and results of observations

Date	Wavelength (nm)	Waveplate	position	p_N	τ_N (°)	p_C	τ_C (°)	s	Residual[1]
2011. 4.17	630	Quartz	East	-0.0406	-18.696	-0.0407	28.484	0.0269	0.007
2011. 4.17	656	Quartz	East	-0.0406	-18.010	-0.0377	31.010	0.0609	0.013
2011. 4.17	854	Quartz	East	-0.0525	-13.965	0.00368	27.435	0.0475	0.014
2011. 4.17	630	Quartz	West	-0.0409	-18.696	-0.0421	28.484	0.0423	0.011
2011. 4.17	656	Quartz	West	-0.0436	-18.010	-0.0392	31.010	0.0523	0.009
2011. 4.17	854	Quartz	West	-0.0505	-13.965	0.0037	27.435	0.0323	0.007
2011. 9. 6	589	APSAW	East	-0.0387	-16.497	-0.0325	28.494	0.0178	0.040
2011. 9. 6	630	APSAW	East	-0.0410	-16.423	-0.0379	26.862	0.00354	0.013
2011. 9. 6	656	APSAW	East	-0.0437	-15.956	-0.0377	28.771	0.00173	0.016
2011. 9. 6	854	APSAW	East	-0.0498	-13.391	0.00252	28.998	0.0145	0.014
2011. 9. 6	1083	APSAW	East	-0.0204	11.424	0.0196	6.064	0.0260	0.009
2012. 4.29	1083	Quartz	West	-0.0236	-9.547	0.0219	-5.561	0.0000	0.020
2012. 6.11&14	1005	APSAW	West	-0.0275	-9.713	0.0270	2.268	0.0045	0.014
2012. 6.11&14	901	APSAW	West	-0.0417	-8.646	0.0246	16.335	0.0499	0.017
2012. 6.11&14	866	APSAW	West	-0.0477	-9.878	0.0153	21.319	0.0035	0.015
2012. 6.11&14	854	APSAW	West	-0.0512	-11.038	0.0113	23.180	0.0200	0.019
2012. 6.11&14	849	APSAW	West	-0.0505	-10.610	0.0097	23.454	0.0078	0.024
2012. 6.11&14	839	APSAW	West	-0.0505	-10.262	0.0062	24.779	0.0005	0.017
2012. 6.25	656	APSAW	West	-0.0419	-17.057	-0.0399	29.294	0.0096	0.006
2012. 6.25	656	APSAW	East	-0.0417	-15.707	-0.0392	30.443	0.0084	0.009
2012. 6.25	630	APSAW	West	-0.0406	-17.693	-0.0385	26.178	0.0146	0.017
2012. 6.25	630	APSAW	East	-0.0407	-16.301	-0.0378	27.453	0.0041	0.010
2012. 6.25	589	APSAW	West	-0.0371	-19.969	-0.0368	20.876	0.0227	0.028
2012. 6.25	589	APSAW	East	-0.0390	-17.711	-0.0340	21.373	0.0000	0.010
2012. 6.25	510	APSAW	West	-0.0369	-21.639	-0.0271	7.647	0.0177	0.009
2012. 6.25	510	APSAW	East	-0.0374	-20.579	-0.0276	9.103	0.0000	0.017
2012. 6.25	486	APSAW	West	-0.0372	-22.886	-0.0252	1.075	0.0405	0.007
2012. 6.25	486	APSAW	East	-0.0365	-21.858	-0.0251	2.737	0.0000	0.025
2012. 6.25	434	APSAW	West	-0.0394	-24.283	-0.0212	-9.910	0.0548	0.016
2012. 6.25	434	APSAW	East	-0.0400	-22.434	-0.0265	-7.665	0.0000	0.027
2012. 6.25	410	APSAW	West	-0.0440	-25.292	-0.0211	-14.340	0.1317	0.020

[1] Root mean square of differences between the fitting results and the averages of Q/I, U/I, and V/I over the detector pixels are written.

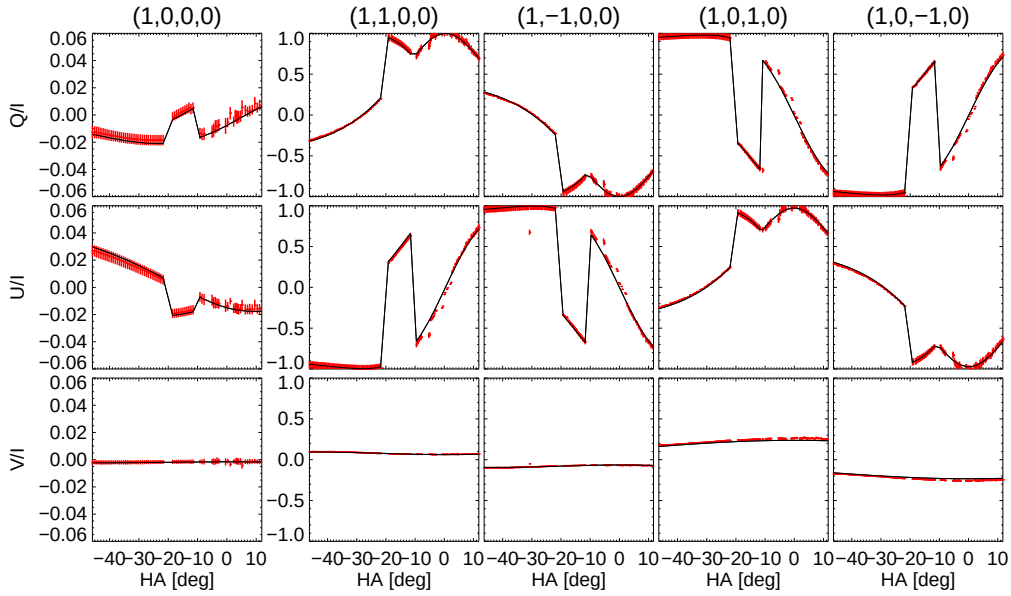

Figure 3.5: Products of the polarimeter (Q/I, U/I and V/I) for unpolarized and linearly polarized incident lights as a function of hour angle of the telescope. Data were taken in 1083 nm on 29 Apr. 2012. Red bars are for the observation data and the black curves are the fitting result with the DST model. The input Stokes vector to the DST is, as shown at the top of each column, unpolarized, $I = Q$, $I = -Q$, $I = U$, and, $I = -U$ from the left to the right. We change inclination angle of slit (θ_i) when hour angle is between $-20°$ and $-12°$. The red bars scale the rms variation of each quantity over the detector.

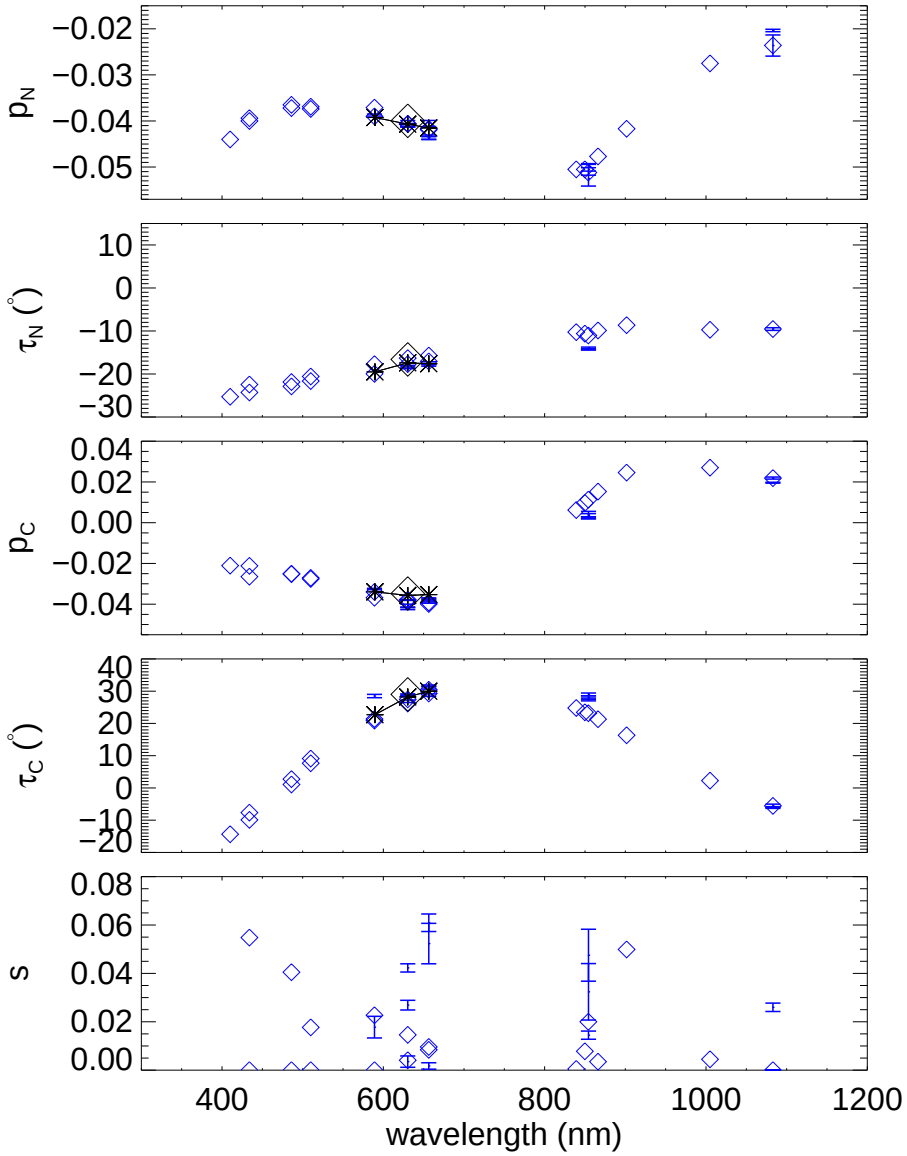

Figure 3.6: Variations of 5 parameters (p_N, τ_N, p_C, τ_C, and s) of our Mueller matrix telescope model against the wavelength (Blue plots). Error bars are standard deviations of the values along a spectrograph slit. Black line and asterisks are results of Hanaoka [17] and black diamond is the result of Kiyohara et al. [18] .

observed responses of the polarimeter are fit with the Mueller matrix model by tuning 5 unknown parameters in the model. The fitting residuals are smaller than spatial variation of the observed Stokes vectors over the detector (Fig. 3.5) and smaller than the requirement on the scale error 0.05 (Table 3.1). In the small polarization degree regime, the residuals of instrumental polarization from our DST model are dominantly produced from the intensity. Since the variation of the instrumental polarization along the wavelength is negligible in the observing spectral window containing a few spectral lines, we can re-calibrate the Stokes profiles by using the polarization of the continuum. Stray light s produces a scale error in polarization magnitude. Spatial variation of s over the detector was found to be smaller than the requirement of 0.05.

In the model, the parameters of mirrors do not depend on the telescope tube position against the rotation axis of the azimuth, but our calibration show non-negligible difference between these values when the telescope tube is set westward and eastward to the rotation axis of the azimuth. The cause of the discrepancy is not identified yet. Our results are slightly different from previous works in 600 nm wavelength range (Fig. 3.6). The parameters of the mirrors might also change slowly due to aging of coatings, etc.. They are needed to be updated. It is possible to derive the 3 parameters (p_N, p_C, and τ_C) without the turret on the entrance window but with only the continuum light at the disk center. We plan to make such quick calibration in more frequent manner to monitor the aging effect or seasonal variations of these parameters.

Figure 3.7 shows an examples of observed data taken with our polarimeter. This is a Stokes spectrum of a flare kernel on 2011 April 18 in the Ca II 854 nm. We put the spectrograph slit on the flare kernel and we show their Stokes spectrum before and after calibration for the instrumental polarization. It took 19 s to obtain the spectrum and the spatial sampling and the resolution of the wavelength are 0.8 arcsec and 7 pm, respectively. The flare kernel produces a central emission in the Ca II 854 nm line and Zeeman effect appears in the Stokes-V profile.

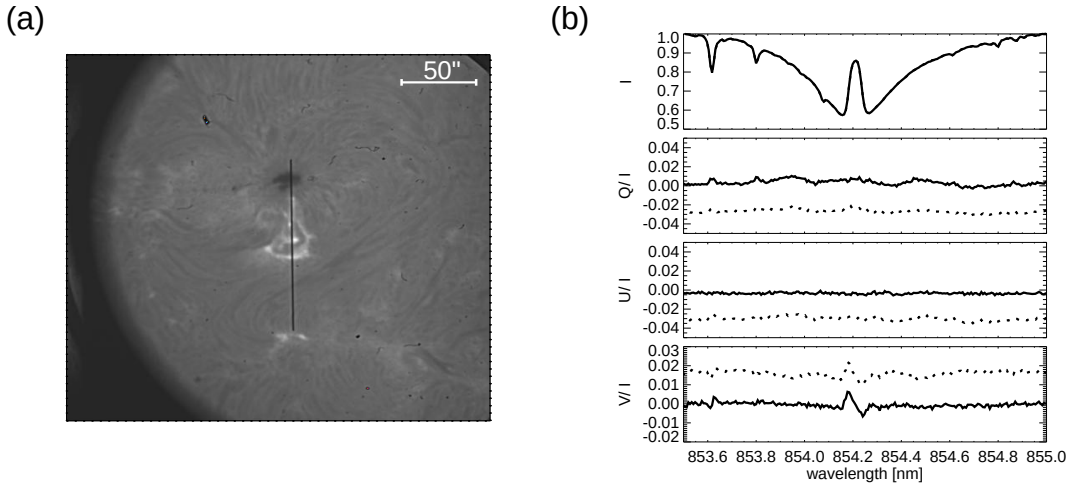

Figure 3.7: Stokes profiles of a flare kernel (b) taken with our polarimeter on 2011 April 18 in the Ca II 854 nm. Solid line and doted line are Stokes spectra after and before the calibration for the instrumental polarization, respectively. Left image (a) is slit-jaw image in Hα center. The black vertical line in the center of the left image is the spectrograph slit. The flare kernel is on the center of the slit.

Chapter 4

Diagnosis of Magnetic and Electric fields of Chromospheric Jets through Spectropolarimetric Observations of HI Paschen Lines

4.1 INTRODUCTION

Chromospheric jets called "surges" often occur near sunspots, in the proximity of neutral points of the magnetic fields [95], in flux emergence regions [96], or in association with magnetic flux cancellation [97]. They reach heights up to 200 Mm and velocities of 50 to 200 km s^{-1} [98]. Recent observations have found tiny chromospheric jets outside sunspots in active regions [99, 100]; their typical length and velocity are 1 to 4 Mm and 5 to 20 km s^{-1}, respectively [3]. In addition, jet-like features are observed in sunspot penumbrae where stronger, inclined magnetic fields and weaker, nearly horizontal magnetic fields co-exist at small spatial scales [101]. These jets are interpreted as the result of magnetic energy release caused by a change of magnetic field topology [99, 102, 103, 28]. However, there are no studies reporting direct measurements of the magnetic field of jets in the chromospheric lines.

Unlike the measurement of magnetic fields, the study of electric fields in solar plasmas has been given little attention. This is partially due to the fact that appreciable quasi-static electric fields on macroscopic spatial scales are unlikely in the solar atmosphere, since the relaxation time for the electric charge is very short in the highly conductive solar atmosphere. Electric fields generated in magnetic reconnection events occur at spatial scales far smaller than the spatial resolution of current spectropolarimetric instrumentation. On the other hand, the spatial scale of Lorentz electric fields associated with plasma motions across the magnetic field can be large enough to be resolved with existing solar telescopes, and the associated Stark effect can be detected in a weakly ionized plasma that is able to reach sufficient bulk velocities across the

magnetic field.

Since detection of the electric field experienced by neutral atoms moving across the magnetic field can tell us about the degree of dynamical coupling between the neutrals and the ionized plasma, the observation and detection of these *motional* electric fields is of particular interest for understanding the dynamics of partially ionized plasmas in the chromosphere.

In order to possibly detect electric fields, we carried out spectropolarimetric observations of the high Paschen series (i.e., large principal quantum number of the upper level) of neutral hydrogen. The choice of hydrogen was motivated because the linear Stark effect (a first order perturbation of the atomic level energy) only occurs in hydrogen-like ions, whereas multi-electron atoms tend to show only quadratic (and higher order) energy effects in the presence of an external electric field. In the case of the linear Stark effect, the splitting of the energy levels is also roughly proportional to the square of the principal quantum number [44, 45], so the use of high transitions in a hydrogen line series is desirable in order to increase the magnitude of the polarization signal. Moran & Foukal [44] and Foukal & Behr [45] estimated the electric field in post flare loops and prominences by studying the line width variation of the linear polarization profile between two orthogonal states of polarization. The implicit assumption in that study was that atomic polarization of such highly excited initial levels could be neglected since they should mainly be populated by isotropic recombination processes [104]. Foukal & Behr [45] measured a surge that occurred in association with a solar flare and obtained a value of the electric field of $\sim 35\,\mathrm{V\,cm^{-1}}$.

Formalisms for the description of hydrogen line polarization in the simultaneous presence of magnetic and electric fields in both local thermodynamic equilibrium (LTE) [105] and non-LTE including atomic polarization [14] have been developed. In LTE, an electric field of the order of 1 V $\mathrm{cm^{-1}}$ produces a linear polarization of the order of 0.1% through the linear Stark effect. Casini [14] pointed out that if an electric field is present in the non-LTE scattering process, magnetic field strengths of order of 10 G can produce a significant level of atomic orientation through the A-O mechanism, comparable to that produced by a magnetic field of the order of 10^3 G in the absence of an electric field. This is because, in the presence of an electric field, magnetic-induced level crossing can happen between $\Delta L = 1$ levels that are separated in energy by a difference comparable to the Lamb shift, rather than by the much larger L-S coupling fine structure energy separation. In the scattering process with both magnetic and electric fields, an electric field of the order of 0.1 V $\mathrm{cm^{-1}}$ is sufficient to modify the linear polarization of the observed Paschen lines by about 1%.

Gilbert et al.[106] evaluated the drain speed of neutral atoms across the magnetic field in a simple prominence model with a partially ionized plasma, in which the solar gravitational force balances with the frictional force proportional to the relative flow

of the neutral and ionized components. Their analytical calculations in steady state show the downflow velocity of neutral hydrogen to be $\sim 1.6\,\mathrm{km\,s^{-1}}$ for a density of $10^{10}\,\mathrm{cm^{-3}}$, assuming a ionization fraction of hydrogen of 10^{-3} and a ionization fraction of helium of 10^{-2}. If we assume a magnetic field strength of 100 G, the electric field experienced by neutral atoms moving across the magnetic field is $\sim 0.16\,\mathrm{V\,cm^{-1}}$, and it is possible that the electric field modifies the polarization of the scattered radiation. In dynamic phenomena, electric fields can be stronger than in the steady state case. For instance, the neutral hydrogen in a surge is ejected with a velocity of 50 to 200 km $\mathrm{s^{-1}}$ with a whiplike motion [98, 107], while neutral hydrogen in prominences descends and rises along vertical threads with a velocity of 5 to 20 km $\mathrm{s^{-1}}$ [108, 109].

In order to study the magnetic and electric fields in chromospheric jets, we observed the full Stokes spectra of the Paschen series of HI in active region jets that took place on the solar limb on May 5, 2012. For convenience, throughout this paper we use the two terms "surge" and "jet" to refer to large and small events, respectively. In the following sections, we describe the details of the observations (Sec. 4.2), the inference of the magnetic and possible electric fields (Sec. 4.3), and finally we discuss our measurements and provide our conclusions (Sec. 4.4).

4.2 Observations and data reduction

Several jets in the active region NOAA 11476 were observed in several HI Paschen lines using the universal spectropolarimeter [34] of the Domeless Solar Telescope [90] at Hida observatory, Japan. The polarimeter uses a continuously rotating achromatic waveplate as polarization modulator and provides the full Stokes vector of any spectral regions between 4000 Å and 11000 Å for all the spatial points along the spectrograph slit, with a spatial sampling of $\sim 0.4\,\mathrm{arcsec/px}$. The full Stokes spectra so obtained were calibrated for instrumental polarization using a predetermined Mueller matrix of the telescope. The expected error on the determination of a given Stokes polarization parameter $S = Q, U, V$, can be expressed as Ichimoto et al. [89] and Anan et al. [34]

$$\delta\left(\frac{S}{I}\right) = a\,\frac{S}{I} + \sigma \tag{4.1}$$

where a is the *polarimetric accuracy* of the calibration and σ is the *rms polarimetric sensitivity* of the observation, which is measured by the statistical noise with respect to the peak intensity of the spectral line. Our calibration procedure guarantees that $|a| \leq 0.05$. Estimates of σ for the different Paschen lines in our observations are given in the next paragraph.

Observation properties

time (UT)	target	line	λ (Å)	noise[a]
2:47	jets	P7	10049.368	2×10^{-3}
3:11	surge	P9	9229.014	2×10^{-3}
3:13	surge	P10	9014.909	3×10^{-3}
3:16	surge	P11	8862.782	3×10^{-3}
3:23	surge	P12	8750.472	3×10^{-3}
3:25	surge	P13	8665.019	4×10^{-3}
3:30	surge	P15	8545.383	-[b]
3:34	surge	P18	8437.956	-[b]
3:34	surge	P19	8413.318	-[b]
3:39	surge	P20	8392.387	-[b]

[a] Noise with respects to the peak intensity of spectral line
[b] Signal is too low to be detected.

The observation ran from 2:32 UT to 3:50 UT on 2012 May 5. Two beams with orthogonal polarizations are taken simultaneously with a CCD camera (Prosilica GE1650) with a spectral sampling of 70 mÅ/pix and an exposure time of 500 msec, and 99 frames are integrated in 49.5 sec, while the spin rate of the rotating waveplate is 0.1 rev./sec. Full Stokes spectra were observed in "sit-and-stare" mode for all Pn lines of the Paschen series of HI, for the values $n = 7, 9, 10, 11, 12, 13, 15, 18, 19, 20$ of the principal quantum number of the upper level. These lines were observed sequentially by rotating the spectrograph grating. The rms polarization sensitivity for the strongest lines P7, P9, P10, P11, P12, and P13, was estimated to be, respectively, $\sim 2 \times 10^{-3}$, 2×10^{-3}, 3×10^{-3}, 3×10^{-3}, 3×10^{-3}, and 4×10^{-3}. We did not analyze the Stokes spectra for the Paschen lines above P15, because the observed signals were lower than 10% of the scattered continuum outside the solar limb, and were thus dominated by flat field errors. The line wavelengths were determined by identifying neighboring absorption lines in the background scattered spectrum in the solar atlas of Kurucz et al. [110]. Because motion of the solar image on the slit caused by the seeing and telescope guiding error was approximately 1 arcsec in amplitude during the run of the observation, we averaged the Stokes spectra in the spatial direction over 2 arcsec. The properties of the observed data set are summarized in Table 1.

The slit was placed outside the solar limb, approximately parallel to it, above active region NOAA 11476. The slit width and length were 1.28 arcsec and 128 arcsec, respectively. In our analysis, the slit identifies the reference direction of polarization, along which Stokes Q is defined to be positive.

Figure 4.1 shows examples of the observed Stokes spectra of the P7, P9, P10, P11, P12, P13, and P15 lines with slit-jaw images taken at the Hα line center. In the spectral ranges of P13 (8665 Å) and P15 (8545 Å) there are strong emission lines of CaII 8662 Å and CaII 8542 Å, whose peaks are strongly saturated. During the observation, some jets and a surge took place across the slit. The jets were observed in P7 between

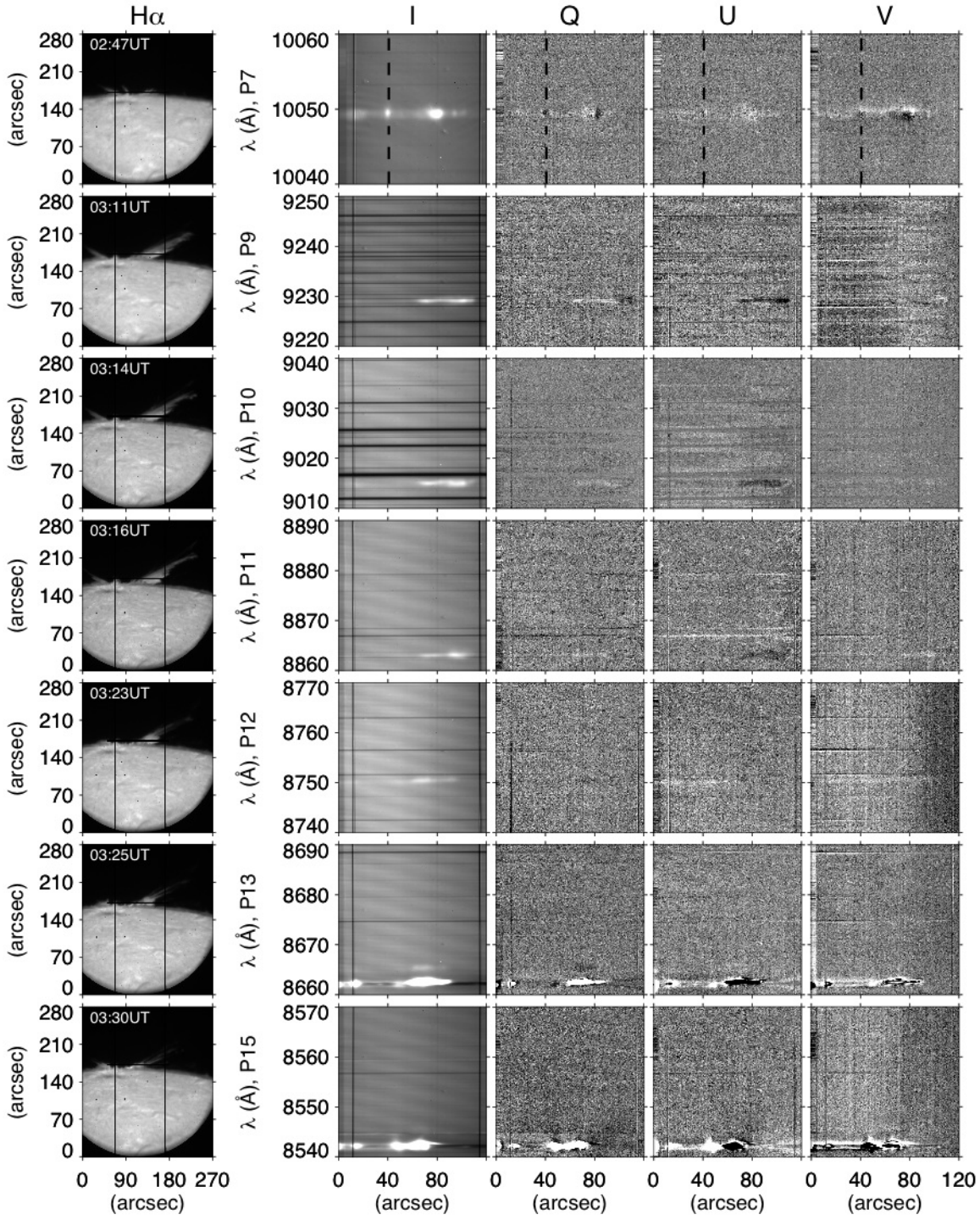

Figure 4.1: Observed Stokes spectra of the Paschen series of neutral hydrogen (4 right columns) and slit-jaw images in Hα (left column). The data set in each row were obtained simultaneously. The horizontal lines in the slit-jaw images show the spectrograph slit. The two vertical lines in the slit-jaw images and the I spectral images show the spectrograph hairlines. The vertical dashed lines in the Stokes spectra of the P7 denote the location of the profiles shown in Figure 4.2. The strong emissions features in the frames of P13 and P15 are the CaII 8662Å and CaII 8542Å lines, respectively.

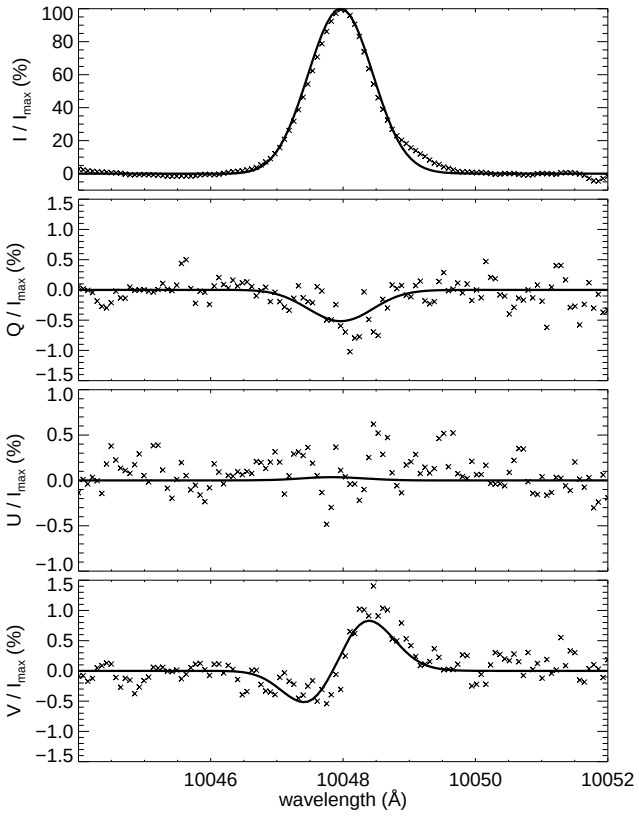

Figure 4.2: Example of the observed Stokes profiles (crosses) of the HI P7 line at 10049Å and the inversion fits (solid curves). The inverted magnetic field vector $(B, \vartheta_B, \varphi_B)$ and temperature are approximately $(128\,\mathrm{G}, 112°, 1.2°)$ and 24300 K, respectively.

2:32 UT and 2:47 UT, while the surge was observed in the P9, P10, P11, P12, P13, P15, P18, P19, and P20 during the second half of the observation period. The distance of the slit to the visible limb for the observation of the jets and the surge was, respectively, ~ 10 arcsec and ~ 15 arcsec.

After correcting our data for instrumental polarization, the Stokes spectra still show a residual polarization signal in the continuum around the Paschen lines. This is likely caused by stray light in the instrument, and indicates that the line signal in the jets and surge is also affected by this spurious polarization. We simply corrected for it by subtracting the polarization offset that is obtained by averaging the Stokes signal in spatial positions along the slit outside the detectable emissions of Paschen lines. These signals are typically dominated by the scattered photospheric spectrum, showing evidence of absorption features in the spectral region of interest. However, in the stray light spectra observed in our data, the photospheric signal of the Paschen lines is not distinguishable.

We also cannot exclude that part of the spurious polarization offset may be due to residual polarization cross-talk from Stokes I after the polarization calibration. In particular, this could be caused by imperfect spatial coregistration and/or intensity rescaling of the two beams with orthogonal polarizations before subtraction. Some evidence of this can be glimpsed from the Stokes Q, U, and V spectra of Figure 1, as some of these spectra clearly show a spurious signal in correspondence with the slit-jaw hairlines. We take into account this possibility in Sec. 4.3.4, when we estimate the effects of possible Lorentz fields on the polarization of the observed lines.

4.3 Diagnosis of magnetic and electric fields

Figure 4.1 and 4.2 show the observed Stokes spectra of the Paschen series of HI and an example of Stokes profiles of P7, respectively. It must be noted that the shape of the linear polarization signals resemble that of the intensity profile. This suggests the presence of atomic polarization in the upper levels of the transitions of neutral hydrogen in the studied jets and surge, and puts into question the assumption that was made in previous studies of electric field measurements by spectro-polarimetric observations, that the atomic polarization of highly excited levels should be negligible [43, 104], presuming that these levels are mostly populated by electron recombination. *Our observations indicate instead that optically pumped atomic polarization must be significant, at least for the upper levels of the Paschen lines that we considered.*

Casini [14] derived a formalism for modeling the scattering polarization of hydrogen lines in the presence of both magnetic and electric fields. In that work, he predicted that a small electric field of the order of $1\,\mathrm{V\,cm^{-1}}$, even if contributing negligible linear polarization via the Stark effect, can still bring important modifications to the atomic polarization of the hydrogen levels when acting in the presence of a magnetic field.

In particular, the simultaneous presence of magnetic and electric fields brings an enhancement of the A-O mechanism that is responsible for the appearance of net circular polarization (NCP).

Figure 4.1 does not show a significant amount of NCP. Since it is not possible to conclude from the data that electric fields may be producing any effect, we carried out the inversion of the Stokes spectra taking into account only the effect of magnetic fields according to the resonance scattering formalism. We then estimated an upper limit for the electric field in the plasma by calculating the polarization degree in the simultaneous presence of magnetic and electric fields, assuming for the magnetic field the configuration derived from the inversion.

4.3.1 Line formation in the presence of magnetic fields: PCA-based inversion of the observations

The inversion of the full Stokes profiles of the observed Paschen HI lines in the presence of a magnetic field made use of pattern recognition techniques. Such type of inversion involves the search of a precomputed database of Stokes profiles for the best match to the observed profiles. Specifically, we adopted Principal Component Analysis (PCA) for our implementation of pattern recognition inversion [111, 112, 12].

The code computing the inversion database of Stokes profiles solves the statistical equilibrium of a quantum model of the HI atom in the presence of the magnetic field [12, 61], and computes from this solution the full Stokes vector of the scattered radiation. Figure 4.3 shows the geometry of resonance scattering in the presence of the magnetic field, and the parameters used in the line formation code.

For a good inversion, the database must cover the full range of parameters spanning the line formation model. The parameters used to construct the precomputed database are the magnetic field strength, B, the inclination of the magnetic field vector with respect to the local solar vertical, ϑ_B, the azimuth angle about the local solar vertical with respect to the x' axis, φ_B, the inclination of the line-of-sight (LOS) from the local solar vertical, ϑ, the height of the scattering point from the solar surface along the local solar vertical, h, the optical thickness of the slab at line center, τ, and the temperature of the plasma in the scattering region, T (Fig. 4.3). The adopted range of these seven parameters, are $0.01 < h < 0.08\,R_\odot$, $0 < B < 1000\,\mathrm{G}$, $0^\circ < \vartheta_B < 180^\circ$, $0^\circ < \varphi_B < 360^\circ$, $82^\circ < \vartheta < 98^\circ$,[1] $0.01 < \tau < 1$, and $1000 < T < 65000\,\mathrm{K}$.

One of the assumptions of the model is that the incident radiation on the scattering atom is not polarized, and possesses cylindrical symmetry around the local solar vertical through the scatterer. In the approximation of complete redistribution under which the line formation model for this problem is valid, we must also assume that the

[1] We note that the LOS corresponding to the minimum height of $0.01\,R_\odot$ would intersect the solar disk if ϑ were outside this range.

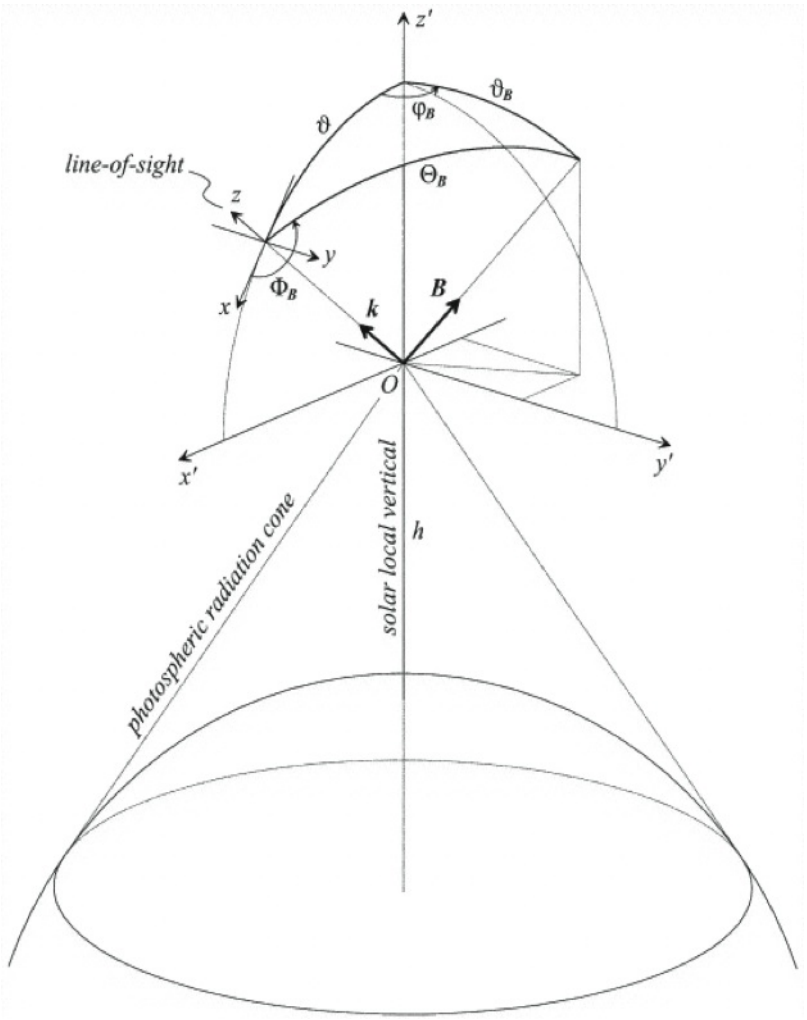

Figure 4.3: Geometric model for radiation scattering in the presence of a magnetic field. The cone of (photospheric) radiation irradiates the scattering atoms at the point O of height h above the solar surface. The direction of the magnetic field vector, $\mathbf{B}$, is defined by the angles ϑ_B and φ_B in the reference frame of the local solar vertical through the point O, and by Θ_B and Φ_B in the reference frame of the LOS, $\mathbf{k}$. The inclination angle of $\mathbf{k}$ from the local solar vertical is ϑ and the direction of $y \equiv y'$, which corresponds to the reference direction of positive Stokes Q, is parallel to the solar limb.

radiation is spectrally flat over the width of the spectral line. Another assumption is to neglect collisional coupling among the atomic levels.In Sect. 4.4 we discuss how this approximation affects the inference of the magnetic and electric fields in the plasma.

The emergent Stokes parameters are obtained by solving the radiative transfer equation

$$\frac{d}{ds}\begin{pmatrix} I \\ Q \\ U \\ V \end{pmatrix} = \begin{pmatrix} \eta_I & \eta_Q & \eta_U & \eta_V \\ \eta_Q & \eta_I & \rho_V & -\rho_U \\ \eta_U & -\rho_V & \eta_I & \rho_Q \\ \eta_V & \rho_U & -\rho_Q & \eta_I \end{pmatrix} \begin{pmatrix} I \\ Q \\ U \\ V \end{pmatrix} + \begin{pmatrix} \epsilon_I \\ \epsilon_Q \\ \epsilon_U \\ \epsilon_V \end{pmatrix}, \tag{4.2}$$

where s is the geometrical distance along the ray passing through a slab and $(\eta_I, \eta_Q, \eta_U, \eta_V)$, (ρ_Q, ρ_U, ρ_V), and $(\epsilon_I, \epsilon_Q, \epsilon_U, \epsilon_V)$ represent, respectively, the dichroic absorption, dispersion, and emission coefficients for the Stokes parameters I, Q, U, and V. The expression for each of those quantities is given by equations (7.47) of Landi Degl'Innocenti & Landolfi [61]. We assume homogenous physical conditions along the optical depth within the slab. When the anomalous dispersion and dichroism terms are small, $\eta_I \gg (\eta_X, \rho_X)$ (with $X = Q, U, V$), and the polarized emission is weak, $\epsilon_I \gg \epsilon_X$, we can formally integrate equation (4.2), yielding [39]

$$\begin{aligned} I(\tau) &= I_0 e^{-\tau} + \frac{\epsilon_I}{\eta_I}(1 - e^{-\tau}) \\ X(\tau) &= \frac{\epsilon_X}{\eta_I}(1 - e^{-\tau}) - I_0 \frac{\eta_X}{\eta_I}\tau e^{-\tau} - \frac{\epsilon_I \eta_X}{\eta_I^2}[1 - e^{-\tau}(1 + \tau)], \end{aligned}$$

where τ (with $d\tau = -\eta_I ds$) is the optical depth along the ray, and I_0 is the background intensity of the slab (which is zero outside the limb).

The above approximate formulas for the emergent Stokes parameters from a homogeneous and weakly polarizing slab are reasonable for the modeling of solar chromospheric structures [39, 31].

The adopted atomic model of HI is composed of the terms in L-S coupling of principal quantum numbers $n = 1, 2, 3, 4$ plus the value of n pertaining to the upper level of the observed transition. L-S coupling is a reasonably good approximation for light atoms such as HI. The reason for including the $n = 4$ level in the atomic model is because of the importance of the Hα and Hβ radiation in the solar spectrum in determining the polarization of the $n = 2, 3, 4$ levels. The omission of the intermediate terms between $n = 4$ and the upper level of the observed transition is justified because the statistical equilibrium of the upper level must be dominated by the optical pumping through the resonant radiation at the frequency of the observed line from the $n = 3$ level, as indicated by the predominance of the atomic polarization signature in the emitted radiation.

Figure 4.4 shows the estimated polarization degree for Stokes Q, U, and V, of the lines P7, P9, P10, and P11, for the case of 90°-scattering of the solar radiation at the limb. The polarization degree is calculated through $Q/I_{\max}$ and $U/I_{\max}$ at line center

in the case of linear polarization, and through the NCP in the case of Stokes V, as a function of the magnetic field strength, and for two geometric configurations of the magnetic field. In the first configuration (upper panel), the magnetic field is directed along the LOS. For zero magnetic field, the scattered light is linearly polarized with positive Q (i.e., parallel to the limb) as expected. For $10^{-2}\,\mathrm{G} < B < 10\,\mathrm{G}$, the direction of the linear polarization is rotated with respect to the zero-field case, and the degree of polarization is also decreased approaching zero around 10 G. These rotation and reduction of the linear polarization of scattered radition are characteristic phenomena of the magnetic Hanle effect. For $B > 1\,\mathrm{G}$, the atomic energy levels within a fine structure term in the upper level start crossing each other, creating the conditions for the Paschen-Back effect and the A-O mechanism to generate asymmetric components in the Stokes V profile as a function of wavelength.

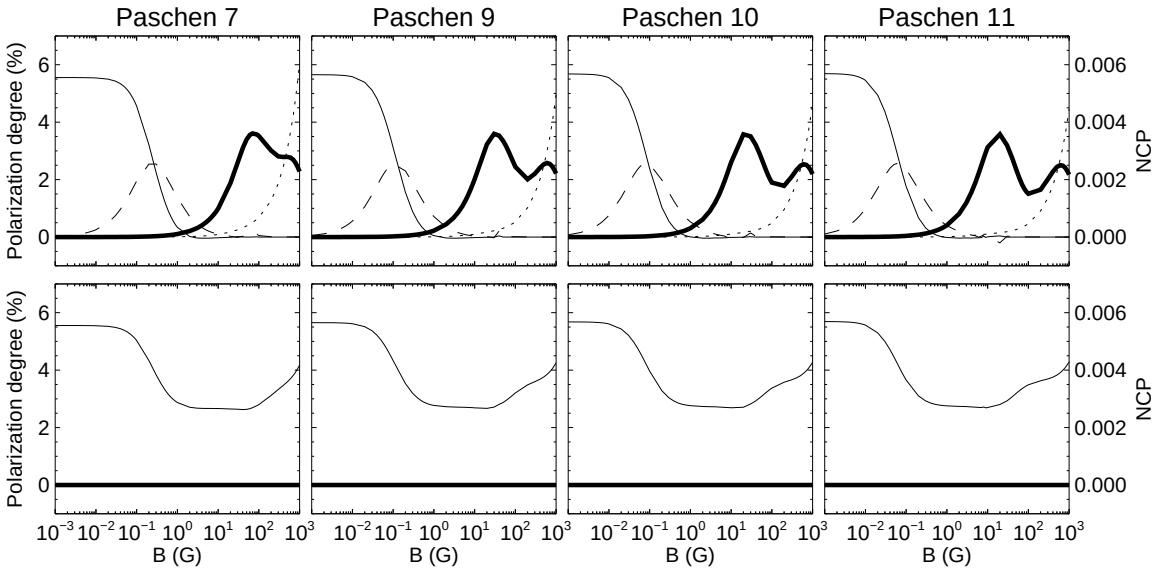

Figure 4.4: Expected polarization as a function of the magnetic field strength in the P7, P9, P10, and P11 lines, for 90° scattering. The top panels show solutions where the magnetic field is directed along the LOS. The bottom panels show solutions were the magnetic field lies in the POS, and is perpendicular to the solar vertical (i.e., horizontal; **B** along the y-axis of Fig. 4.3). The thin solid lines and the dashed lines show, respectively, Q/I_{max} and U/I_{max} at line center. The dotted lines show V/I_{max} at +0.5Å from line center. The thick solid lines show the NCP.

In the second magnetic configuration (lower panel), the magnetic field is perpendicular to the LOS and parallel to the limb. For $10^{-2}\,\mathrm{G} < B < 10\,\mathrm{G}$, the Hanle effect only depolarizes the scattered radiation, to about 1/2 of the zero-field value. For B larger than a few 10 G, the generation of linear polarization by anisotropic pumping of radiation becomes more efficient due to the change of energy configuration of the atom in the transition to the Paschen-Back regime [61, 78], when the spin-orbit interaction

becomes negligible with respect to the magnetic interaction.

The fundamental concepts of PCA inversion of Stokes profiles were described by Rees et al. [111]. Applications of this technique to scattering polarization on the Sun were considered by L ópez Ariste & R. Casini [12] and Casini et al. [35, 113, 114]. PCA is mainly a technique for pattern recognition and data compression. It allows an efficient decomposition of the Stokes profiles using only a very small number of "universal" principal components (eigenprofiles) out of the full basis that would be needed for a lossless reconstruction of the profiles. The dimension of the PCA basis equals the number of wavelength points in the profiles. Since the number of principal components needed to reconstruct the Stokes profile to within the polarization sensitivity of the observations is much smaller (typically by at least one order of magnitude) than the number of wavelength points, PCA allows a much faster comparison of the observed data with the model than iterative fitting. Additionally, the use of a precomputed database of profiles for data inversion is free from the risk of converging to local minima typical of iterative fitting.

4.3.2 Test of the inversion code

We examined the reliability of our inversion scheme by performing test runs for 10,000 synthetic Stokes profiles calculated with randomly distributed parameters in the 7D parameter space within the ranges specified earlier, after adding to the profiles a random noise of 3×10^{-3} with respect to the peak intensity. The inversion tests were run for P7, P9, P10, and P11, using a database of 100,000 models. Figure 4.5 shows the inversion results against the actual values of the synthetic model for each parameter, for the case of the P7 line. The results for the inversion of the other lines are similar to the case of P7, and therefore we do not shown them here.

Figure 4.5b shows the scatter plot of the longitudinal magnetic field strength ($B \cos \Theta_B$). This quantity is determined rather well from the inversion of Stokes V, which is mostly affected by the longitudinal Zeeman effect. In contrast, the error in the inversion of the magnetic field strength and the inclination angle of the magnetic field vector is rather large (Figs. 4.5a and 4.5c). This can be understood when we consider that, for these Paschen lines, the Hanle effect is completely saturated already for $B > 10\,\mathrm{G}$ (Fig. 4.4), whereas the Zeeman effect does not produce a significant linear polarization until the field reaches strengths of the order of a few kG. Therefore, for $10 \leq B \leq 1000\,\mathrm{G}$ the inferred magnetic field strength is derived mainly from the circular polarization signal.

Since there can be different values of the magnetic field strength corresponding to a given degree of NCP or to the amplitude of the linear polarization induced by resonance scattering (Fig. 4.4), and considering that the atomic alignment from which both these polarization signals originate depends on the true height (versus the observed projected height) of the scatterer over the solar surface, as well as on the inclination

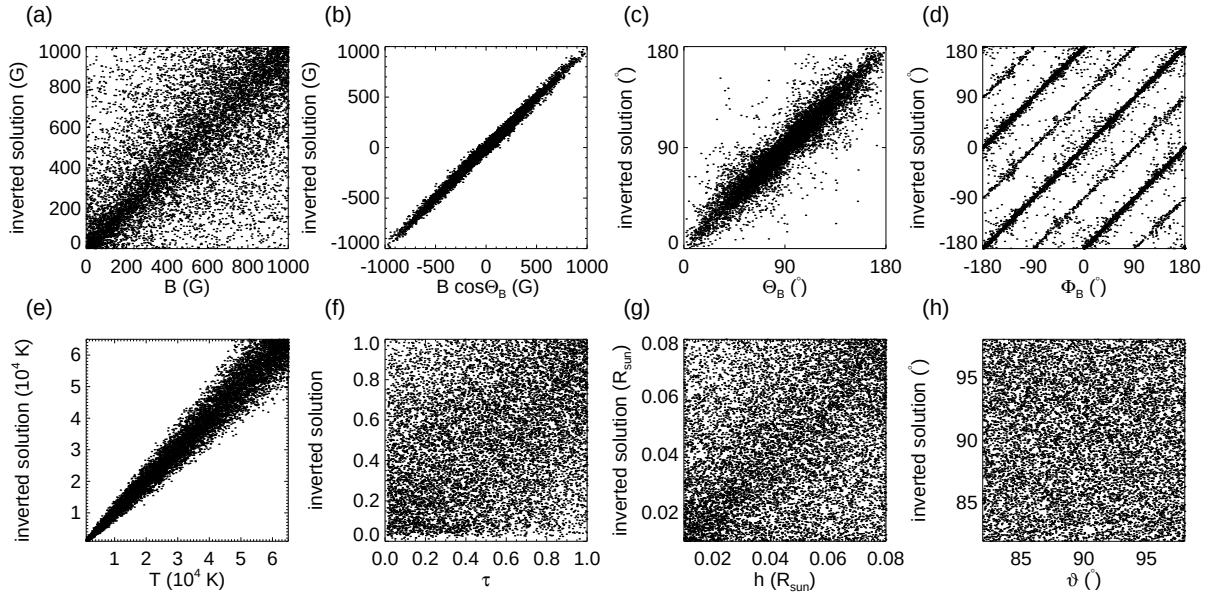

Figure 4.5: Scatter plots of the inverted vs true values of the model parameters for 10,000 random synthetic profiles of P7. The PCA-based inversions used a database of 100,000 models spanning the same parameter ranges as the synthetic profiles.

of the magnetic field from the local solar vertical ϑ_B (see eqs. [4.3] below), we can understand why the inference of the magnetic field strength and inclination can be affected by larger errors.

The scatter plot of the inverted azimuth angle of the magnetic field in the reference frame of the observer, Φ_B, exhibits multiple streaks, which are caused by intrinsic ambiguities of scattering line polarization with the geometry of the field (Fig. 4.5d). Typical examples are the well-known 180°-ambiguity of the Zeeman effect, and the 90°-ambiguity of the saturated regime of the Hanle effect [115, 116, 83, 113]. In order to see this, we consider the emissivity for Stokes Q and U in the saturated regime of the Hanle effect for a two-level atom with unpolarized lower level, and neglecting stimulated emission. This is simply expressed by

$$\begin{array}{l} \epsilon_Q \sim w(3\cos^2\vartheta_B - 1)\sin^2\Theta_B\cos 2\Phi_B \\ \epsilon_U \sim w(3\cos^2\vartheta_B - 1)\sin^2\Theta_B\sin 2\Phi_B \end{array} \quad , \tag{4.3}$$

where w is the anisotropy factor of the radiation field [83]. A sign change of Stokes Q and U due to a 90° change of Φ_B can thus be compensated by a sign change of the factor $(3\cos^2\vartheta_B - 1)\sin^2\Theta_B$. Therefore the condition for the presence of the 90° ambiguity (in the optically thin case) is the existence of ϑ'_B and Θ'_B such that

$$(3\cos^2\vartheta_B - 1)\sin^2\Theta_B = -(3\cos^2\vartheta'_B - 1)\sin^2\Theta'_B. \tag{4.4}$$

Since the dependence of the Stokes Q and U polarization on the geometry of the field and the observer, as given by eqs. (4.3), is modified in the optically thick case, or for

the case of a multi-level atom, we have checked this dependence numerically in the optically thick case relying on our line formation model. As a result, we verified that the expected variations of the polarization degree of the Paschen series with optical thickness remain below the noise level of the observations, and thus we can still rely on eqs. (4.3) to provide an approximate description of the azimuthal ambiguities even for our more general atomic and radiative transfer models. In the inversion results (see Sect. 4.3.3), we determine whether the inferred configuration is subject to ambiguities, by checking whether the condition (4.4) can be realized for that configuration.

If we ignore the ambiguities shown in Fig. 4.5d, the 90% confidence interval for the inversion of Φ_B is $\pm 13^\circ$ for P7, P9, P10, and P11.

The temperature is inferred from the line width under the assumption that this is determined by thermal broadening. The error on T is estimated to be $0.2\,T$, based on the scatter plot of Fig. 4.5e.

The determination of the remaining parameters is not very accurate. The optical depth deforms the line shape and slightly changes the polarization degree of the line. The height of the scatterer determines the dilution and anisotropy factors of the incident radiation field, which in turn determines the state of atomic polarization in the zero-field case. However, a change of the height over the entire parameter range, between 0.01 and $0.08\,R_\odot$ causes only small changes in the polarization degree of the lines. The same is true for the change of ϑ between 82° and 98°.

4.3.3 Inversion results

The observed Stokes spectra of the P7, P9, P10, and P11 lines were inverted using the PCA technique illustrated in Sect. 4.3.1, in order to derive the magnetic and plasma model of the emitting plasma in the observed active region's jets and surge. We did not invert the Paschen lines above P11, because the signal-to-noise ratios of the polarization signals were too low.

For the inversion, the possible effects of an electric field (e.g., of the Lorentz type) were neglected. The Doppler velocity was derived from the shift of the center of gravity of the Stokes I profiles, using the wavelengths of the Paschen lines as reported by Kramida [117].

Figure 4.2 shows an example of inversion fit of the Stokes vector of P7 for a jet, the location of which is indicated by the dashed lines in the top of Fig. 4.1. Our spectral synthesis does not reproduce the complex shape of Stokes profiles produced in a spatially unresolved, multi-component atmosphere, because of the assumption of a homogeneous slab. Nonetheless, most of the observed Stokes profiles fit satisfactorily some synthetic profile in our inversion database with only 100,000 models, as shown in Fig. 4.2.

The distributions of the inverted parameters along the slit are shown in Figure 4.6.

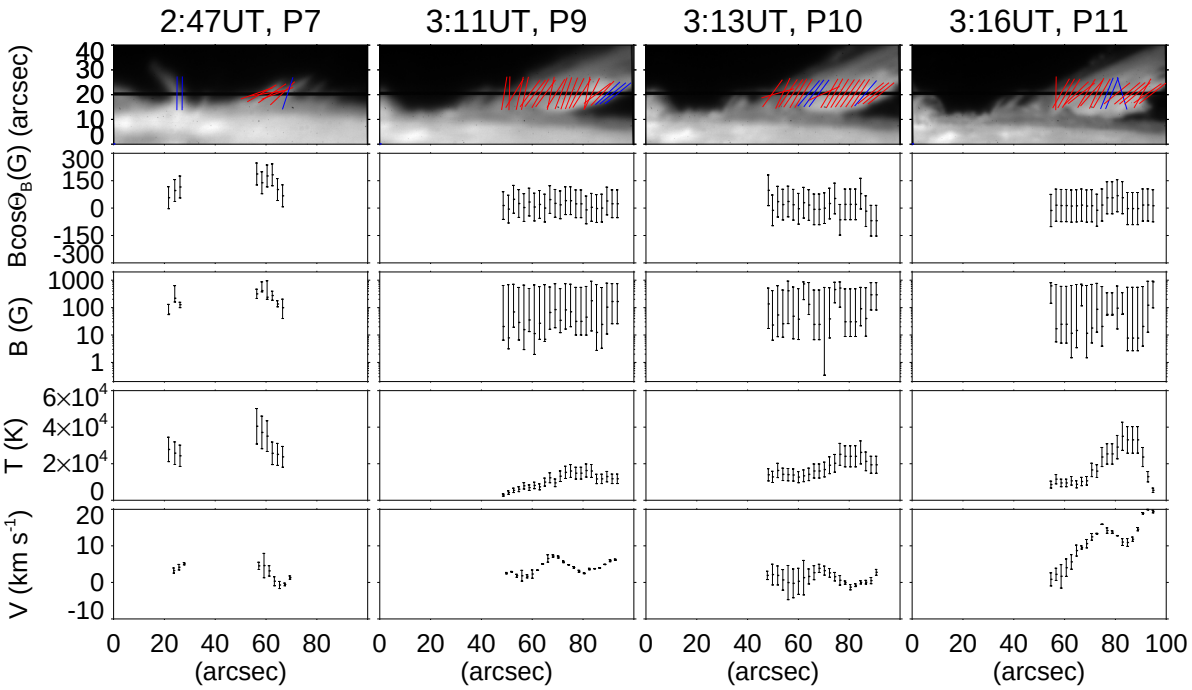

Figure 4.6: Inverted magnetic field, temperature, and Doppler velocity for the observed jets and surge at the position of the slit shown in the figure. The columns, from left to right, show the inversion results for the observed Stokes spectra of P7 (2:47 UT), P9 (3:11 UT), P10 (3:13 UT), and P11 (3:16 UT). The slit-jaw images in the top row show the direction of the magnetic field on the POS. The red lines indicate inverted solutions affected by the 90° azimuthal ambiguity, while the blue lines correspond to the solutions with nonambiguous azimuth. The second to fifth rows show, respectively, the longitudinal component of the magnetic field, the magnetic field strength, the temperature, and the Doppler velocity. The abscissas indicate the position along the slit.

The ranges of the physical parameters estimated from the inversion corresponding to the 90% confidence level (Sec. 4.3.2) are shown in the four bottom rows, respectively for the longitudinal component of the magnetic field, the magnetic field strength, the plasma temperature, and the plasma velocity along the LOS. In the top row, the direction of the lines indicates the direction of the magnetic field on the POS (related to Φ_B). The red (blue) color marks the solutions which admit (do not admit) an alternative 90°-ambiguous configuration of the magnetic field. The magnetic field solutions that do not admit this azimuthal ambiguity indicate that the projected magnetic field on the POS is approximately aligned to the jets and the surge. Accordingly, 60% of the solutions marked with the red lines were rotated by 90° in order to align the projected magnetic field on the POS to the directions of the jets and the surge. After this operation, it is noticeable that the direction of the magnetic field on the POS appears to be systematically tilted away from the surge by about 25° counterclockwise, which is larger than the estimated inversion error of 13° of Φ_B corresponding to the 90% confidence level. We do not speculate on the physical origin of this tilt.

The inverted magnetic field component along the LOS ($B_\parallel = B\cos\Theta_B$) is comprised in the following ranges, respectively for the three jets and the surge: $0\,\mathrm{G} < B_\parallel < 180\,\mathrm{G}$, $80\,\mathrm{G} < B_\parallel < 250\,\mathrm{G}$, $10\,\mathrm{G} < B_\parallel < 160\,\mathrm{G}$, and $-70\,\mathrm{G} < B_\parallel < 100\,\mathrm{G}$.

For the magnetic field strength of the three jets, using the observation at 2:47 UT, we found $60\,\mathrm{G} < B < 630\,\mathrm{G}$, $190\,\mathrm{G} < B < 960\,\mathrm{G}$, and $40\,\mathrm{G} < B < 200\,\mathrm{G}$. In the case of the surge, the circular polarization is practically absent, leading to a larger uncertainty in the determination of the magnetic field strength in that structure. For a 90% confidence level we found $10\,\mathrm{G} < B < 640\,\mathrm{G}$.

Figure 4.6 shows other parameters that are determined by the inversion. The derived temperature must be regarded as an upper limit, because only thermal and natural broadening were considered for the inversion, while other broadening mechanisms such as pressure broadening, plasma turbulence, and collisional damping may also contribute to the effective line width. The maximum Doppler velocity of the surge at 3:11 UT, 3:13 UT, and 3:16 UT was $7\,\mathrm{km\,s^{-1}}$, $4\,\mathrm{km\,s^{-1}}$, and $16\,\mathrm{km\,s^{-1}}$, respectively.

4.3.4 Upper limit of the electric field

The time evolution of the surge can be seen in Figure 4.7, which shows a slit-jaw image at the line core of Hα (left) and two time-distance diagrams showing the motion along two different sections of the surge, respectively parallel (top right) and perpendicular (bottom right) to it.

The surge first appeared at 2:58 UT, ejected at a speed of $\sim 100\,\mathrm{km\,s^{-1}}$, initially with a whiplike motion, finally reaching a length of $\sim 110,000\,\mathrm{km}$. The observations taken at 3:11 UT, 3:13 UT, and 3:16 UT show the surge near its maximum extension. The observed Doppler shift indicates a significant component of plasma velocity along

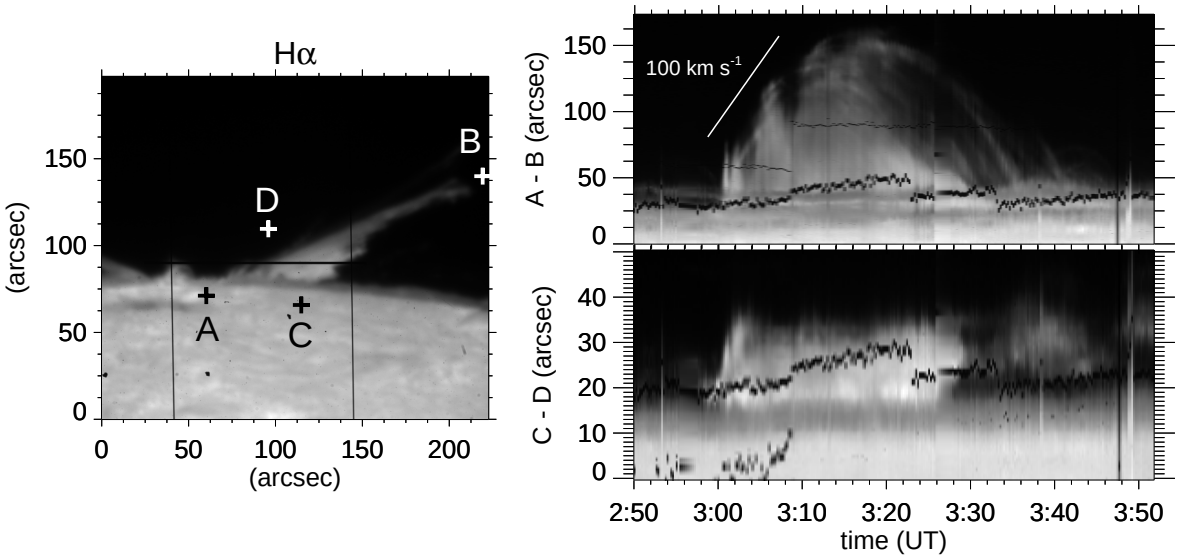

Figure 4.7: *Left:* Slit-jaw image in Hα of the surge observed at 3:16 UT. *Right:* Time-distance diagrams obtained between the points A and B (top), and C and D (bottom), marked on the slit-jaw image on the left. The thick dots in the diagrams show the spectrograph slit. The thin dots in the top diagram show one of the spectrograph hairlines.

the LOS, which is also nearly perpendicular to the magnetic field, if we accept the inversion results that the magnetic field vector practically lies in the POS (Fig.4.6). Therefore, this event provides a good opportunity for testing the coupling between partially ionized plasma and magnetic fields, since neutral atoms that move across the magnetic field must experience a motional electric field.

We used the inverted magnetic and velocity field configurations of the surge as the basis to calculate the emergent Stokes profiles in the additional presence of an electric field (Fig. 4.8). The magnetic field, which is roughly aligned to the surge, is inclined about 45° from the local solar vertical, and on the POS (Fig. 4.6). The velocity component is assumed to be along the LOS, because no significant apparent lateral motions were observed in the Hα slit-jaw images at the times of the observation, 3:11 UT, 3:13 UT, and 3:16 UT (Fig. 4.7). Since the inferred magnetic field strength in the surge varies approximately between $10\,\mathrm{G} < B < 640\,\mathrm{G}$, we calculated the expected line polarizations in the presence of a motional electric field for three magnetic-field strengths of 70, 200, and 600 G. Unlike the surge, the magnetic field in the jets has a significant component along the LOS. Since it is difficult to estimate the velocity component across the magnetic field from the time evolution of the plasma in the observations, we omit any discussion about the estimation of electric fields in the jets.

We calculated the theoretical net linear and circular polarizations of the Paschen HI lines as functions of the strength of the motional electric field, assumed to be per-

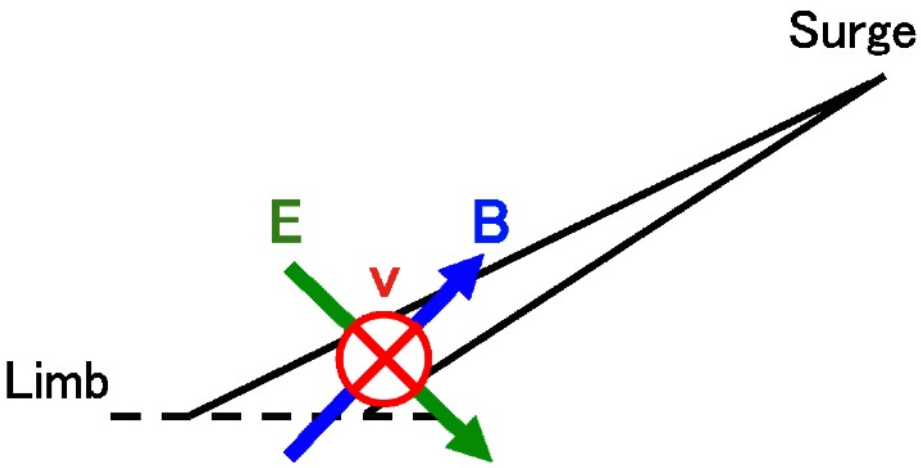

Figure 4.8: Schematic picture of the magnetic, electric, and velocity vectors in the surge.

pendicular to both the magnetic field and the LOS, using the formalism of Casini [14]. Because of the particular field geometry (both fields lie on the POS), all configurations where the orientation of either of the two fields is inverted give rise to the same polarization.

Figure 4.9 shows the results for P10 for the three selected values of the magnetic field strength. It is notable that the direction of the linear polarization does not change appreciably when the electric field is applied. This is in fact dominated by Stokes U at all times, in agreement with the fact that the atom is in the saturated regime of the (magnetic) Hanle effect, and therefore the direction of linear polarization must be perpendicular to the magnetic field direction (135° in this calculation). This fact allows us to determine the azimuth angle of the magnetic field (Φ_B) from the inversion independently of the effect of possible electric fields.

The upper limit of the electric field in the P10 at 3:13 UT is estimated by comparing the observed polarization degree with the calculated values. Because of the residual continuum polarization observed in the Stokes spectra after correcting them for instrumental polarization (see end of Sect. 4.2), the observed polarization degree is affected by both random and systematic errors. In Figure 4.9, the horizontal dotted lines in each plot limit the range of polarization error due to both systematic (either instrumental stray light or residual polarization cross-talk) and random sources. Additional polarization effects due to an undetected motional electric field must then lie within this range.

We thus find an upper limit of 0.04, 0.3, and 0.8 $\mathrm{V\,cm^{-1}}$, respectively for the magnetic field strength of 70, 200, and 600 G. This implies that the upper limit of the

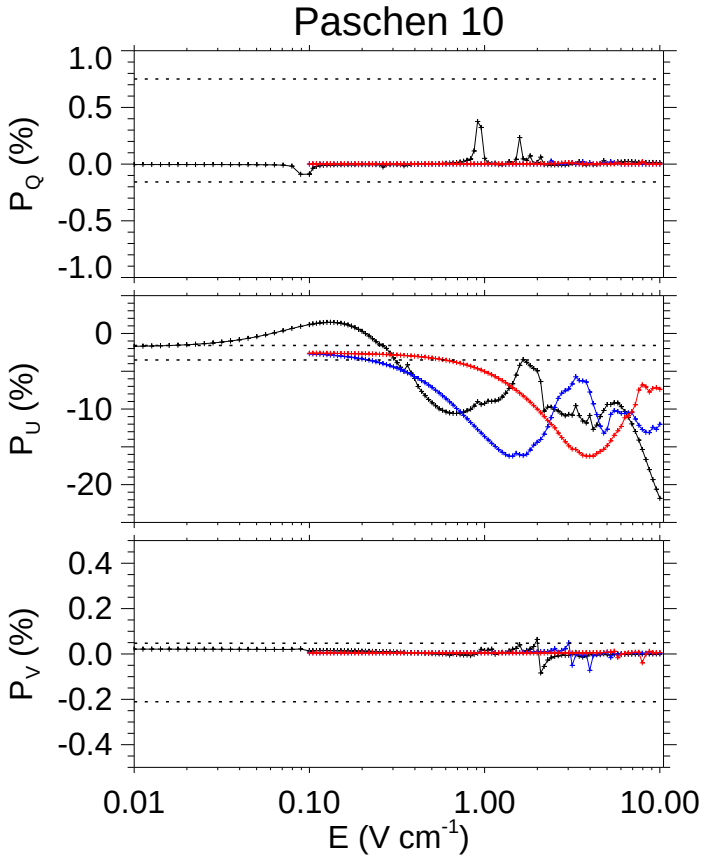

Figure 4.9: Broadband polarization of P10 in Stokes Q (top), U (center), and V (bottom), as a function of the electric field strength, in a 90° scattering event. The magnetic field lies on the POS, with azimuth $\Phi_B = 135°$ (see Fig. 4.3). The electric field also lies on the POS, and is assumed to be perpendicular to the magnetic field. Black, blue, and red lines correspond to magnetic field strengths of 70, 200, and 600 G, respectively. The horizontal lines in each plot limit the range of polarization error due to both random and systematic (instrumental stray light and residual polarization cross-talk) sources.

velocity of neutral hydrogen moving across the magnetic field corresponds respectively to 0.6, 1.5, and 1.3 $\mathrm{km\,s^{-1}}$. Since the measured Doppler velocity in the P10 at 3:13 UT is $3.4 \pm 1.6\,\mathrm{km\,s^{-1}}$, the velocity of neutral hydrogen moving across the magnetic field appears to be significantly smaller than the plasma's bulk velocity.

In the same way, we estimated the upper limit of the velocity of neutral hydrogen moving across the magnetic field at 3:11 UT from observations of the P9 line. We found in this case the values 0.8, 1.5, and 1.1 $\mathrm{km\,s^{-1}}$ for the same magnetic field strengths, in very good agreement with the results found with P10. Using the P11 data (observed at 3:16 UT) we found instead 1.1, 1.0, and 0.8 $\mathrm{km\,s^{-1}}$, which also are in agreement with the results from P9 and P10. Since the measured Doppler velocity in the P9 at 3:11 UT, and in the P11 at 3:16 UT, are $3.3 \pm 0.2\,\mathrm{km\,s^{-1}}$ and $12.5 \pm 1.4\,\mathrm{km\,s^{-1}}$, respectively, all estimated upper limits of the velocity across the magnetic field are smaller than the measured Doppler velocities.

4.4 Discussion and summary

We presented magnetic field inferences in a surge and in active region jets, and a first estimation of the upper limit of motional electric fields, and the corresponding limit to plasma velocities across the magnetic field lines.

The direction of the magnetic field on the POS is found to approximately align to the jets and the surge. This confirms the common scenario of the chromospheric jet model, in which plasma is ejected along the magnetic field [99, 28]. When we look carefully at the geometric relation between the magnetic field and the jet, we find that the direction of the magnetic field is slightly tilted counterclockwise from the direction of the surge. Further study with high-accuracy spectro-polarimetric data for a number of similar events is needed in order to clarify the details of the geometric relation between the magnetic field and jets.

The strength of the magnetic field in the three jets is found to be in the ranges $60\,\mathrm{G} < B < 630\,\mathrm{G}$, $190\,\mathrm{G} < B < 960\,\mathrm{G}$, and $40\,\mathrm{G} < B < 200\,\mathrm{G}$. This determination is driven mainly by the observed circular polarization signal and its symmetry characteristics. Because NCP can also be generated by the coupling of velocity and magnetic field gradients along the LOS [70], and since our model does not contemplate the possibility of a multi-component atmosphere, we cannot exclude the possibility that the inferred magnetic field strengths may be affected by the possible presence of velocity and magnetic field inhomogeneities along the LOS.

The upper limit of the motional electric field is estimated to be $0.04\,\mathrm{V\,cm^{-1}}$ for a magnetic field strength of 70 G, based on the observed polarization degree in the P10 line. If we neglect the magnetic field and the atomic level polarization, as assumed in previous estimates of solar electric fields, the limit to the electric field that is derived from the observed polarization degree (using, e.g., the formalism of Goto [10]) is $\sim$

$30\,\mathrm{V\,cm^{-1}}$, which is significantly larger than our estimates.

In our inversion model, we neglected collisional coupling among the atomic levels, which tends to reduce the amount of linear polarization and NCP in the scattered radiation. In the case of the surge, the observed linear polarization may be explained through a combination of collisional depolarization with the polarization effects of the magnetic field and the possible motional electric fields in the plasma (Fig. 4.9). In particular this implies that our inferred upper bounds for the motional electric field present in the surge could be underestimated. Similarly, our model might underestimate the LOS component of the magnetic field, if the observed low values of NCP were caused by the destruction of atomic orientation by collisions. Finally, we note that the presence of isotropic collisions does not cause a significant change of the direction of the emergent linear polarization, hence we can still reliably determine the azimuth angle of the magnetic field on the POS (Φ_B) from the inversion, independently of the effects of the collisions.

From the upper limit of the motional electric field, we also estimated the velocity of neutral hydrogen moving across the ambient magnetic field. At 3:16 UT, the surge reaches its maximum height (Fig. 4.7) and a large bulk velocity (i.e., Doppler shift) is observed (Fig. 4.6). Therefore the velocity vector can be assumed to be along the LOS and perpendicular to the magnetic field (Fig. 4.6). On the other hand, from our analysis of the polarization effects of motional electric fields, the upper limit of the velocity of neutral hydrogen moving across the magnetic field is found to be $1.1\,\mathrm{km\,s^{-1}}$ in this geometry. As this is much smaller than the measured bulk velocity of $12.5 \pm 1.4\,\mathrm{km\,s^{-1}}$, our estimate of the upper bound of the motional electric fields in the plasma leads us to conclude that neutrals must be in a highly frozen-in condition in the surge.

Chapter 5

Summary and Concluding Remarks

We opened a new window of plasma diagnostics to measure magnetic and electric fields by using atomic polarization, and we presented magnetic field measurements in a surge and in active region jets, and a first estimation of the upper limit of Lorentz electric field, and the corresponding limit to plasma velocities across the magnetic field lines.

In order to develop new plasma diagnostics by using polarization mechanism of spectral line, i.e., Zeeman effect, Paschen-Back effect, Stark effect, resonance scattering, impact polarization, Hanle effect, and Alignment-to-Orientation conversion to measure the external magnetic field, electric field, and anisotropies in atomic excitation in solar atmosphere, we developed a new spectropolarimeter on the Domeless Solar Telescope at Hida observatory. The polarimeter consists of a 60 cm aperture vacuum telescope, a high dispersion slit vacuum spectrograph, a continuously rotating achromatic waveplate as polarization modulator, Wollaston prisms as polarization analyzer, and CCD camera and infrared camera as detector. The polarimeter provides the full Stokes vector of any spectral regions between 4000 Å and 11000 Å for all the spatial points along the spectrograph slit. A photometric accuracy of 10^{-3} can be achieved in $\sim$ 30 s and $\sim$ 60 s in visible and near infrared by radiation emitted from solar disk center, respectively. Instrumental polarization of the telescope is calibrated by using a remotely controllable turret accommodating linear polarizer attached at the entrance window of the telescope to induce well known polarized light into the telescope. Thus a Mueller matrix model of the telescope for spectral regions between 4000 Å and 11000 Å is established to compensate the instrumental polarization included in observed data within the required accuracy.

Among several new plasma diagnostics which the polarimeter enable us to develop, we selected a topic for this thesis, i.e., measurement of magnetic field and electric field of chromospheric jets by using atomic polarization, and we observed full Stokes spectra of the Paschen series of neutral hydrogen in a surge and in some active region jets. Our observation indicate that optically pumped atomic polarization must be significant, at

least for the upper levels of the observed transitions, while assumptions in previous studies of electric field measurements were negligible of the atomic polarization. The choice of the lines was motivated because the splittings of subcomponents of the lines are sensitive to electric field by the Stark effect.

Having found no definitive evidence of the effects of electric fields in the observed Stokes profiles, we first inverted the Stokes spectra taking into account only the effect of magnetic fields. The inferred direction of the magnetic field on the plane of the sky approximately aligns to the active region jets and the surge. This confirms the common scenario of the chromospheric jet model. We found 60 G $< B <$ 630 G, 190 G $< B <$ 960 G, 40 G $< B <$ 200 G, and 10 G $< B <$ 640 G for the magnetic field strength of the three jets and the surge, respectively.

We then estimated an upper limit for the electric fields by calculating the polarization degree under the magnetic field configuration derived in the inversion, with the additional presence of a perpendicular Lorentz type electric field of varying strength in the resonance scattering formalism. Using magnetic field strengths of 70, 200, and 600 G, we obtained upper limits for possible electric fields of 0.04, 0.3, and 0.8 $\mathrm{V\,cm^{-1}}$, respectively

Since detection of the Lorentz type electric field experienced by neutral atoms moving across the magnetic field can tell us about the degree of dynamical coupling between the neutrals and the ionized plasma, the observation and detection of these electric fields is of particular interest for understanding the dynamics of partially ionized plasmas in the chromosphere. Under the geometry derived from observation, the velocity vector can be assumed to be along the line of the sight and perpendicular to the magnetic field. From the upper limit of the Lorentz type electric field, the upper limit of the velocity of neutral hydrogen moving across the ambient magnetic field in the surge is estimated to be $1.1\,\mathrm{km\,s^{-1}}$ at 3:16 UT. Because this is much smaller than the measured bulk velocity of $12.5 \pm 1.4\,\mathrm{km\,s^{-1}}$ as measured by the Doppler shift, we conclude that neutrals must be in a highly frozen-in condition in the surge.

The measurement of electric field is expected to open the new era of research for the physics of neutral dynamics. In addition, if large electric field accelerates charged particle in flare loop, we are able to detect the field directly. Furthermore, if we should resolve current sheet in magnetic reconnection region, we would measure the resistivity and the diffusion of the magnetic field. The electric fields in particle acceleration and reconnection region are essential part of these physics.

Finally it should be pointed out that polarization is useful to diagnose vector quantities and the measurement of electric field will be a large piece of solar physics.

Bibliography

[1] Hathaway, D. H., "The solar cycle," *Living Reviews in Solar Physics* **7**, no.1 (2010).

[2] Ito, H., Tsuneta, S., Shiota, D., Tokumaru, M., and Fujiki, K., "Is the polar region different from the quiet region of the sun?," *Astrophysical Journal* **719**, 131–142 (2010).

[3] Nishizuka, N., Nakamura, T., Kawate, T., Singh, K. A. P., and Shibata, K., "Statistical study of chromospheric anemone jets observed with hinode/sot," *The Astrophysical Journal* **731**, 43–54 (2011).

[4] Berger, T. E., Slater, G., Hurlburt, N., Shine, R., Tarbell, T., Title, A., Lites, B. W., Okamoto, T. J., Ichimoto, K., Katsukawa, Y., Magara, T., Suematsu, Y., and Shimizu, T., "Quiescent prominence dynamics observed with the hinode solar optical telescope. i. turbulent upflow plumes," *The Astrophysical Journal* **716**, 1288–1307 (2010).

[5] Arnaud, J. and Jr., G. N., "Mean properties of the polarization of the fe xiii 10747 åcoronal emission line," *Astronomy and Astrophysics* **178**, 263–268 (1987).

[6] Lin, H., Kuhn, M. R., and Coulter, R., "Coronal magnetic field measurements," *Astrophysical Jounal* **613**, L177–L180 (2004).

[7] Zaitsev, V. V., Urpo, S., and Stepanov, A. V., "Temporal dynamics of joule heating and dc-electric field acceleration in single flare loop," *Astronomy and Astrophysics* **357**, 1105–1114 (2000).

[8] Snik, F. and Keller, C., "Astronomical polarimetry: polarized views of stars and planets," , **,**, , (2011).

[9] Sakurai, T., "Computational modeling of magnetic fields in solar active regions," *Space Science Reviews* **51**, 11–48 (1989).

[10] Goto, M., [*Plasma Polarization Spectroscopy ed. T. Fujimoto & A. Iwamae, chapter 2*], SPRINGER (2008).

[11] Bueno, J. T., "Atomic polarization and the hanle effect," *Proceedings of Advanced Solar Polarimetry* **236**, 161–195 (2001).

[12] Ariste, A. L. and Casini, R., "Magnetic fields in prominences: Inversion techniques for spectropolarimetric data of the hei d_3 line," *The Astrophysical Journal* **553**, 949–954 (2001).

[13] James, G. K., Slevin, J. A., Dziczek, D., McConkey, J. W., and Bray, I., "Polarization of lyman-α radiation from atomic hydrogen excited by electron impact from near threshold to 1800 ev," *Physical Review A* **57**, 1787–1797 (1998).

[14] Casini, R., "Resonance scattering formalism for the hydrogen lines in the presence of magnetic and electric fields," *Physical Review* **71**, 062505 (2005).

[15] del Toro Iniesta, J. and Collados, M., "Optimum modulation and demodulation matrices for solar polarimeter," *Applied Optics* **39**, 1637–1642 (2000).

[16] Ichimoto, K., Shinoda, K., Yamamoto, T., and Kiyohara, J., "Photopolarimetric measurement system of mueller matrix with dual rotating waveplates," *Publications of the National Astronomical Observatory of Japan* **9**, 11–19 (2006).

[17] Hanaoka, Y., "Spectropolarimetry with the hida domeless solar telescope," *Publications of the Astronomical Society of Japan* **61**, 357–365 (2009).

[18] Kiyohara, J., Ueno, S., Kitai, R., Kurokawa, H., Makaita, M., and Ichimoto, K., "Calibration of the instrumental polarization of the domeless solar telescope at the hida observatory," in [*Ground-based Instrumentation for Astronomy*], Moorwood, A. F. M. and Masanori, I., eds., *Proc. SPIE* **5492**, 1778–1785 (2004).

[19] Hale, G. E., "On the probable existence of a magnetic field in sun-spots," *Astrophysical Jounal* **28**, 315–343 (1908).

[20] Borrero, J. M. and Ichimoto, K., "Magnetic structure of sunspots," *Living Reviews in Solar Physics* **8**, no.4 (2011).

[21] Stenflo, J. O., "Magnetic-field structure of the photospheric network," *Solar Physics* **32**, 41–63 (1973).

[22] Stenflo, J. O., "Collapsed, uncollapsed, and hidden magnetic flux on the quiet sun," *Astronomy and Astrophysics* **529**, 42–62 (2011).

[23] Tsuneta, S., Ichimoto, K., Katsukawa, Y., Lites, B. W., Matsuzaki, K., Nagata, S., Suárez, D. O., Shimizu, T., Shimojo, M., Shine, R. A., Suematsu, Y., Suzuki, T. K., Tarbell, T. D., and Title, A. M., "The magnetic landscape of the sun's polar region," *Astrophysical Journal* **688**, 1374–1381 (2008).

[24] Dikpati, M. and Charbonneau, P., "A babcock-leighton flux transport dynamo with solar-like differential rotation," *Astrophysical Journal* **518**, 508–520 (1999).

[25] Shiota, D., Tsuneta, S., Shimojo, M., Sako, N., Suárez, D. O., and Ishikawa, R., "Polar field revearsal observations with hinode," *Astrophysical Journal* **753**, 157–165 (2012).

[26] Lites, B. W., Kubo, M., Socas-Navarro, H., Berger, T., Frank, Z., Shine, R., Tarbell, T., Title, A., Ichimoto, K., Katsukawa, Y., and Tsuneta, S., "The horizontal magnetic flux of the quiet-sun internetwork as observed with the hinode spectro-polarimeter," *Astrophysical Journal* **672**, 1237–1253 (2008).

[27] Ishikawa, R. and Tsuneta, S., "Comparison of transient horizontal magnetic fields in a plage region and in the quiet sun," *Astronomy and Astrophysics* **495**, 607–612 (2009).

[28] Takasao, S., Isobe, H., and Shibata, K., "Numerical simulations of solar chromospheric jets associated with emerging flux," *Publications of the Astronomical Society of Japan* **65**, 62–84 (2013).

[29] Hillier, A., Isobe, H., Shibata, K., and Berger, T., "Numerical simulations of the magnetic rayleigh-taylor instability in the kippenhahn-schlüter prominence model," *Astrophysical Jounal* **736**, L1–L6 (2011).

[30] Bueno, J. T., Degl'Innocenti, E. L., Collados, M., Merenda, L., and Sainz, R. M., "Selective absorption process as the origin of puzzling spectral line polarization from the sun," *Nature* **415**, 403–406 (2002).

[31] Bueno, J. T. and Ramos, A. A., "Influence of atomic polarization and horizontal illumination on the stokes profiles of the hei 10830åmultiplet," *The Astrophysical Journal* **655**, 642–650 (2007).

[32] Collados, M., Lagg, A., Garcí, A. J. J. D., Suárez, E. H., López, R. L., Mañá, E. P., and Solanki, S. K., "Tenerife infrared polarimeter ii," in [*The Physics of Chromospheric Plasmas ASP Conference Series*], Heinzel, P., Dorotovič, I., Rutten, R. J., and of the Pacific, S. F. A. S., eds., *Proc. of the conference held 9-13 October, 2006 at the University of Coimbra in Coimbra, Portugal*, 611–616 (2007).

[33] Jaeggli, S. A., Lin, H., Mickey, D. L., Kuhn, J. R., Hegwer, S. L., Rimmele, T. R., and Penn, M. J., "Firs: a new instrument for photospheric and chromospheric studies at the dst," *Memorie della Societa Astronomica Italiana* **81**, 763–768 (2010).

[34] Anan, T., Ichimoto, K., Oi, A., Kimura, G., Nakatani, Y., and Ueno, S., "Developments of the wideband spectropolarimeter of the domeless solar telescope at hida observatory," *SPIE* **8446**, 1C (2012).

[35] Casini, R., Ariste, A. L., Tomczyk, S., and Lites, B. W., "Magnetic maps of prominences from full stokes analysis of the hei d_3 line," *The Astrophysical Journal* **598**, L67–L70 (2003).

[36] Merenda, L., Bueno, J. T., Degl'Innocenti, E. L., and Collados, M., "Determination of the magnetic field vector via the hanle and zeeman effects in the he i λ10830 multiplet: Evidence for nearly vertical magnetic fields in a polar crown prominence," *The Astrophysical journal* **642**, 554–561 (2006).

[37] Sasso, C., Lagg, A., and Solanki, S. K., "Multicomponent he i 10830 å profiles in an active filament," *Astronomy and Astrophysics* **526**, A42 (2011).

[38] Ariste, A. L. and Casini, R., "Inference of the magnetic field in spicules from spectropolarimetry of hei d_3," *Astronomy and Astrophysics* **436**, 325–331 (2005).

[39] Bueno, J. T., Merenda, L., Centeno, R., Collados, M., and Degl'Innocenti, E. L., "The hanle and zeeman effects in solar spicules: A novel diagnostic window on chromospheric magnetism," *The Astrophysical Journal* **619**, L191–L194 (2005).

[40] Lagg, A., Woch, J., Krupp, N., and Solanki, S. K., "Retrieval of the full magnetic vector with the hei multipret at 1083 nm," *Astronomy and Astrophysics* **414**, 1109–1120 (2004).

[41] Mickey, D. L., "Polarization measurements in the green coronal line," *Astrophysical journal* **181**, L19–L21 (1973).

[42] Lin, H., Penn, M. J., and Tomczyk, S., "A new precise measurement of the coronal magnetic field strength," *Astrophysical Jounal* **541**, L83–L86 (2000).

[43] Foukal, P. and Hinata, S., "Electric fields in the solar atmosphere - a review," *Solar Physics* **132**, 307–334 (1991).

[44] Moran, T. and Foukal, P., "An electrograph for measurement of macroscopic electric fields in prominence and flares," *Solar Physics* **135**, 179–191 (1991).

[45] Foukal, P. V. and Behr, B. B., "Testing mhd models of prominences and flares with observations of solar plasma electric fields," *Solar Physics* **156**, 293–314 (1995).

[46] Vlahos, L., Isliker, H., and Lepreti, F., "Particle acceleration in an evolving network of unstable current sheets," *Astronomical Journal* **608**, 540–553 (2004).

[47] Blackman, E. G., "Distinguishing solar flare types by differences in reconnection regions," *Astronomical Journal* **484**, L79–L82 (1997).

[48] Karlický, M. and Kosugi, T., "Acceleration and heating processes in a collapsing magnetic trap," *Astronomy and Astrophysics* **419**, 1159–1168 (2004).

[49] Kumar, N. and Roberts, B., "Ion-neutral collisions effect on mhd surfaces waves," *Solar Physics* **214**, 241–266 (2003).

[50] Khodachenko, M. L., Arber, T. D., Rucker, H. O., and Hanslmeier, A., "Collisional and viscous damping of mhd waves in partially ionized plasma of the solar atmosphere," *Astronomy and Astrophysics* **422**, 1073–1084 (2004).

[51] Leake, J. E., Arber, T. D., and Khodachenko, M. L., "Collisional dissipation of alfén waves in a partially ionized solar chromosphere," *Astronomy and Astrophysics* **442**, 1091–1098 (2005).

[52] Forteza, P., Oliver, R., Ballester, J. L., and Khodachenko, M. L., "Damping of oscillations by ion-neutral collisions in a prominence plasma," *Astronomy and Astrophysics* **461**, 731–739 (2008).

[53] Vranjes, J., Poedts, S., Pandey, B. P., and de Pontieu, B., "Energy flux of alfvén waves in weakly ionized plasma," *Astronomy and Astrophysics* **478**, 553–558 (2008).

[54] Soler, R., Oliver, R., and Ballester, J. L., "Time damping of non-adiabatic magnetohydrodynamic waves in a partially ionized prominence plasma: effect of helium," *Astronomy and Astrophysics* **512**, 28–33 (2010).

[55] Brandenburg, A. and Zweibel, E. G., "The formation of sharp structure by ambipolar diffusion," *Astrophysical Journal* **427**, L91–L94 (1994).

[56] Vishniac, E. T. and Lazarian, A., "Reconnection in the interstellar medium," *Astrophysical Journal* **511**, 193–203 (1999).

[57] Krishan, V., "Sweet-parker current slab in a partially ionized plasma," *Monthly Notices of the Royal Astronomical Society* **400**, 2200–2206 (2009).

[58] Singh, K. A. P., Isobe, H., Nishizuka, N., and Shibata, K., "Multiple plasma ejections and intermittent nature of magnetic recconection in solar chromospheric anemone jets," *Astrophysical Journal* **759**, 33–47 (2012).

[59] Henoux, J. C., Chambe, G., Smith, D., Tamres, D., Feautrier, N., Rovira, M., and Sahal-Brechot, S., "Impact line linear polarization as a diagnostic of 100 kev proton acceleration in solar flares," *Astrophysical Journal Supplement Series* **73**, 303–311 (1990).

[60] Hurford, G. J., Krucker, S., Lin, R. P., Schwartz, R. A., Share, G. H., and Smith, D. M., "Gamma-ray imaging of the 2003 october/november solar flares," *Astrophysical Jounal* **644**, L93–L96 (2006).

[61] Degl'Innocenti, M. L. and Degl'Innocenti, M. L., [*Polarization in Spectral Lines*], Astrophysics and space library (2004).

[62] Lehmann, H., "Luminescence and absorption studies on sapphire with flash light excitation," *Journal of Physics and Chemistry of Solids* **25**, 941–950 (1964).

[63] Degl'Innocenti, E. L., "The determination of vector magnetic fields in prominences from the observations of the stokes profiles in the d3 line of helium," *Solar Physics* **79**, 291–322 (1982).

[64] Kemp, J. C., Macek, J. H., and Nehring, F. W., "Induced atomic orientation, an efficient mechanism for magnetic circular polarization," *Astrophysical Jounal* **278**, 863–873 (1984).

[65] Favati, B., Degl'Innocenti, E. L., and Landolfi, M., "Resonance scattering of lyman-α in the presence of an electrostatic field," *Astronomy and Astrophysics* **179**, 329–338 (1987).

[66] Bommier, V., Leroy, J. L., and Sahal-Bréchot, S., "The linear polarization of hydrogen h-beta radiation and the joint diagnostic of magnetic field vector and electron density in quiescent prominences - part two - the electron density," *Astronomy and Astrophysics* **156**, 90– (1986).

[67] Sahal-Bréchot, S., Vogt, E., Thoraval, S., and Diedhiou, I., "Impact polarization of the hα line of hydrogen in solar flares: calculations of electron and proton collisional anisotropic process between the zeeman excited sublevels," *Astronomy and Astrophysics* **309**, 317–334 (1996).

[68] Štěpán, J. and Bueno, J. T., "Scattering polarization of hydrogen lines in weakly magnetized steller atmosphere. i. formation and application to isothermal models," *The Astrophysical journal* **732**, 80–100 (2011).

[69] Zeeman, P., "On the influence of magnetism on the nature of the light emitted by a substance," *Philosophical Magazine* **43**, 226– (1897).

[70] Illing, R. M., Landman, D. A., and Mickey, D. L., "Observations of broad-band circular polarization in sunspots - magnetic field correspondence," *Astronomy and Astrophysics* **35**, 327–331 (1974).

[71] Almeida, J. S. and Lites, B. W., "Observation and interpretation of the asymmetric stokes q, u, and v line profiles in sunspots," *Astrophysical Journal* **398**, 359–374 (1992).

[72] Makita, M., "An interspretation of the broad-band circular polarization of sunspots," *Solar Physics* **106**, 269–286 (1986).

[73] Solanki, S. K. and Montavon, C. A. P., "Uncombed fields as the source of the broad-band circular polarization of sunspots," *Astronomy and Astrophysics* **275**, 283–292 (1993).

[74] Stark, J., "Observations of the effect of the electric field on spectral lines i. transverse effect," *Ann. d. Phys.* **43**, 965–983 (1914).

[75] Surdo, A. L., "?," *Accad. Lincei Atti* **22**, 665 (1913).

[76] White, H., [*Introduction to Atomic Spectra*], International Series in Pure and Applied Physics (1934).

[77] Štěpán, J., Bueno, J. T., Carlsson, M., and Leenaarts, J., "The hanle effect of lyα in a magnetohydrodynamic model of the solar transition region," *Astrophysical Journal Letters* **758**, L43–L48 (2012).

[78] Casini, R. and Sainz, R. M., "Scattering polarization of hydrogen lines in the presence of turbulent electric fields," *Journal of Physics B* **39**, 3241–3253 (2006).

[79] Skinner, H. W. B., "On the excitation of polarised light by electron impact," *Proceedings of the Royal Society of London* **112**, 642–660 (1926).

[80] Hénoux, J. C., Heristchi, D., Chambe, G., Machado, M., Woodgate, B., Shine, R., and Beckers, J., "Conductive flux in flaring solar chromospheres deduced from the linear polarization observations," *Astronomy and Astrophysics* **119**, 233–238 (1983).

[81] Syms, R. F., McDowell, M. R. C., Morgan, L. A., and Myerscough, V. P., "?," *J. Phys. B, Atom. Molec. Phys.* **19**, 2817– (1975).

[82] Hanle, W., "über den zeemaneffekt bei der resonanzfluoreszenz," *Naturwissenschaften* **11**, 690–691 (1923).

[83] Casini, R., "The hanle effect of the two-level atom in the weak-field approximation," *The Astrophysical Journal* **568**, 1056–1065 (2002).

[84] Cohen-Tannoudji, C., Diu, B., and Laloë, F., ",," *Mécanique Quantique, Hermann, Paris* **,**, , (1977).

[85] Cohen-Tannoudji, C., Dupont-Roc, J., and Grynberg, G., ",," *Photons et Atomes, InterEditions, Editions du CNRS, Paris* **,**, , (1987).

[86] Gandorfer, A. M. and Povel, H. P., "First observations with a new imaging polarimeter," *Astronomy and Astrophysics* **328**, 381–389 (1997).

[87] Stenflo, J. O., "The hanle effect and the diagnostics of turbulent magnetic fields in the solar atmosphere," *Solar Physics* **80**, 209–226 (1982).

[88] Stenflo, J. O. and Keller, C. U., "The second solar spectrum. a new window for diagnostics of the sun," *Astronomy and Astrophysics* **321**, 927–934 (1997).

[89] Ichimoto, K., Lites, B., Elmore, D., Suematsu, Y., Tsuneta, S., Katsukawa, Y., Shimozu, T., Shine, R., Tarbell, T., Title, A., Kiyohara, J., Shinoda, K., Card, G., Lecinski, A., Streander, K., Nakagiri, M., Miyashita, M., Noguchi, M., Hoffmann, C., and Cruz, T., "Polarization calibration of the solar optical telescope onboard hinode," *Solar Physics* **249**, 233–261 (2008).

[90] Nakai, Y. and Hattori, A., "Domeless solar tower telescope at the hida observatory," *Kyoto University, Faculty of Science, Memoirs, Series of Physics, Astrophysics, Geophysics and Chemistry* **36**, 385–399 (1985).

[91] Nakai, Y., "New domeless solar telescope in hida observatory," in [*Japan-France Seminar on Solar Physics*], Moriyama, F. and Henoux, J. C., eds., *Proc. teh Conference*, 275 (1980).

[92] Makita, M., Funakoshi, Y., and Hanaoka, Y., "Polarization of the domeless solar telescope of the hida observatory (preliminary report)," in [*Solar Polarimetry*], L. J. November. Sunspot, N., ed., *Proc. the 11th Sacramento Peak Summer Workshop*, 198–210 (1991).

[93] Skumanich, A., Lites, B. W., Pillet, V. M., and Seagraves, P., "The calibration of the advanced stokes polarimeter," *Astrophysical Jounal Supplement* **110**, 357–380 (1997).

[94] Stenflo, J. O., "Polarization of the sun's continuous spectrum," *Astronomy and Astrophysics* **429**, 713–730 (2005).

[95] Rust, D. M., "Chromospheric explosions and satelite sunspots," *Proceedings of the International Astronomical Union Sympossium* **35**, 77–84 (1968).

[96] Kurokawa, H., "Surge activity in an emerging magnetic region of the sun," *Vistas in Astronomy* **31**, 67–71 (1988).

[97] Gaizauskas, V., "Magnetic reconnection as a driver of chromospheric surges," *Solar Physics* **169**, 357–366 (1996).

[98] Roy, J. R., "The magnetic properties of solar surges," *Solar Physics* **28**, 95–114 (1973).

[99] Shibata, K., Nakamura, T., Matsumoto, T., Otsuji, K., Okamoto, T. J., Nishizuka, N., Kawate, T., Watanabe, H., Nagata, S., Ueno, S., Kitai, R., Nozawa, S., Tsuneta, S., Suematsu, Y., Ichimoto, K., Shimizu, T., Katsukawa, Y., Tarbell, T. D., Berger, T. E., Lites, B. W., Shine, R. A., and Title, A. M., "Chromospheric anemone jets as evidence of ubiquitous reconnection," *Science* **318**, 1591–1594 (2007).

[100] Morita, S., Shibata, K., Ueno, S., Ichimoto, K., Kitai, K., and Otsuji, K., "Observations of chromospheric anemone jets with hinode caii broadband filtergraph and hida caii spectrograph," *Publications of the Astronomical Society of Japan* **62**, 901–920 (2010).

[101] Katsukawa, Y., Berger, T. E., Ichimoto, K., Lites, B. W., Nagata, S., Shimizu, T., Shine, R. A., Suematsu, Y., Tarbell, T. D., and Title, A. M., "Small-scale jetlike features in penumbral chromosphere," *Science* **318**, 1594–1597 (2007).

[102] Ryutova, M., Berger, T., Frank, Z., and Title, A., "On the penumbral jetlike features and chromospheric bow shocks," *The Astrophysical Journal* **686**, 1404–1419 (2008).

[103] Nakamura, N., Shibata, K., and Isobe, H., "Numerical sumilation of three-dimentional asymmetric reconnection and application to a physical mechanism of penumbral microjets," *The Astrophysical Journal* **761**, 87–97 (2012).

[104] Casini, R. and Degl'Innocenti, E. L., "Lte radiative transfer for polarized hydrogen lines in the weak-field regime," *Astronomy and Astrophysics* **308**, 335–344 (1996).

[105] Casini, R. and Degl'Innocenti, E. L., "The polarized spectrum of hydrogen in the presence of electric and magnetic fields," *Astronomy and Astrophysics* **276**, 289–302 (1993).

[106] Gilbert, H. R., Hansteen, V. H., and Holzer, T. E., "Neutral atom diffusion in a partially ionized prominence plasma," *The Astrophysical Journal* **577**, 464–474 (2002).

[107] Nishizuka, N., Shimizu, M., Nakamura, T., Otsuji, K., Okamoto, T. J., Katsukawa, Y., and Shibata, K., "Giant chromospheric anemone jet observed with hinode and comparison with magnetohydrodynamic simulations: Evidence of propagating alfvén waves and magnetic reconnection," *The Astrophysical Journal* **683**, L83–L86 (2008).

[108] Zirker, J. B., Engvold, O., and Martin, S. F., "Counter-streaming gas flows in solar prominences as evidence for vertical magnetic fields," *Nature* **396**, 440–441 (1998).

[109] Berger, T. E., Shine, R. A., Slater, G. L., Tarbell, T. D., Title, A. M., Okamoto, T. J., Ichimoto, K., Katsukawa, Y., Sumatsu, Y., Tsuneta, S., Lites, B. W., and SHimizu, T., "Hinode sot observations of solar quiescent prominence dynamics," *The Astrophysical Journal* **676**, L89–L92 (2008).

[110] Kurucz, R. L., Furenlid, I., Brault, J., and Testerman, L., [*Solar flux atlas from 296 to 1300 nm*], National Solar Observatory Atlas, Sunspot, New Mexico (1984).

[111] Rees, D. E., Ariste, A. L., Thatcher, J., and Semel, M., "Fast inversion of spectral lines using principle component analysis i. fundamentals," *Astronomy and Astrophysics* **355**, 759–768 (2000).

[112] Socas-Navarro, H., Ariste, A. L., and Lites, B. W., "Fast inversion of spectral lines using principle component analysis ii. inversion of real stokes data," *The Astrophysical Journal* **553**, 949–954 (2001).

[113] Casini, R., Bevilacqua, R., and Ariste, A. L., "Principal component analysis of the hei d_3 polarization profiles from solar prominences," *Astronomy and Astrophysics* **622**, 1265–1274 (2005).

[114] Casini, R., Ariste, A. L., Paletou, F., and Léger, L., "Multi-line stokes inversion for prominence magnetic-field diagnostics," *The Astrophysical Journal* **703**, 114–120 (2009).

[115] House, L. L., "Coronal emission-line polarization from the statistical equilibrium of magnetic sublevels. i. fe xiii," *The Astrophysical Journal* **214**, 632–652 (1977).

[116] Casini, R. and Judge, P. G., "Spectral lines for polarization measurements of the coronal magnetic field. ii consistent treatment of the stokes vector for magnetic-dipole transitions," *The Astrophysical Journal* **522**, 524–539 (1999).

[117] Kramida, A. E., "A critical compilation of experimental data on spectral lines and energy levels of hydrogen, deuterium, and tritium," *Atomic Data and Nuclear Data Tables* **96**, 586–644 (2010).